Magnetotransport in Graphene: A study of Quantum Hall Breakdown, Energy Loss Rates, and Weak Localization

Anton M. R. Baker

Magdalen College, Oxford

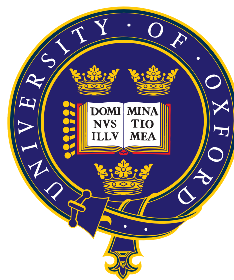

Thesis submitted in fulfilment of the requirements for the degree of Doctor of Philosophy at the University of Oxford

Trinity Term, 2012

Magnetotransport in Graphene: A study of Quantum Hall Breakdown, Energy Loss Rates, and Weak Localization

Anton M. R. Baker, Magdalen College, Oxford

Thesis submitted in fulfilment of the requirements for the degree of Doctor of Philosophy at the University of Oxford. Trinity Term, 2012

Abstract

This thesis reports magnetotransport measurements in graphene Hall bar devices. Graphene samples fabricated from different techniques (epitaxial growth on silicon carbide, exfoliation, and CVD) are measured and compared. Measurements are taken primarily using a 21T magnet, at liquid Helium 4 temperatures.

The first three chapters present the background for the work. Chapter One details the motivation for the thesis, and gives a general background to carbon and the state of carbon research. Chapter Two covers the theoretical background of graphene, including the anomalous quantum Hall effect and weak localization. Chapter Three covers the synthesis of graphene and a typical procedure undertaken for device fabrication.

The next three chapters report experimental results. Chapter Four presents measurements of the energy loss rates in exfoliated graphene. The mechanism of carrier energy loss is investigated, and compared to theory. Further, the breakdown of the quantum Hall effect in the device is investigated, demonstrating peak current densities far in excess of those found in the literature for exfoliated graphene. Chapter Five shows measurements comparing the carrier energy loss rates in graphene derived from the epitaxial, exfoliated and CVD fabrication techniques. An unconventional method for measuring the energy loss rate based on measuring the weak localization peak is developed, and trends in the energy loss rates with carrier density are investigated for a wide range of devices. Chapter Six reports a comparison of the decomposed weak localization scattering lengths from graphene devices derived from the epitaxial and CVD methods, and compares these to measurements from the literature. Further, a previously reported saturation of the weak localization in graphene is investigated, and demonstrated to be an experimental artefact.

This thesis provides a development of the understanding, and an experimental verification, of several aspects of heat transfer in graphene. An understanding of heat transfer is of critical importance to proposed high-density nano-electronics, and bolometry applications. The high breakdown currents and observed trends in carrier density are also of significant assistance in the design of low-cost resistance metrology devices based on graphene.

Acknowledgements

I would like to take the opportunity to thank briefly all those who made this thesis possible.

First, I would like to thank my supervisor Prof. Robin Nicholas for all the invaluable help, guidance and enthusiasm he has given me over the years. His boundless knowledge and passion for the subject never cease to be a source of inspiration.

I would also like to thank all those in the RJN group and beyond for the countless pieces of assistance and fascinating tea-time discussions, in particular my colleagues, past and present, in the RJN group: Jack Alexander-Webber, Thomas Altebaeumer, Ken Chuang, Beate Dirks, David McMullan, James Orr, Torben Schüttfort, Sam Stranks and Richard Tuley.

I thank EPSRC for the funding which made my studies possible, and the Condensed Matter Physics Sub-Department for their conference funding and overall framework of support, particularly the support staff without whom much of our work would not have been possible.

I also owe many thanks to Magdalen College, which has been not just a place of learning, but also my home these past eight years, and to all the people who make it the magical place that it is.

Last but not least, I am extremely grateful to all my friends and family for their unending patience and encouragement, and particularly my fiancée, Aparna, who never ceases to be the most wonderful person and to support me every step of the way in all I do.

Contents

1 Introduction **1**

1.1 Motivation 2

1.2 Carbon 2

1.2.1 Unique properties of carbon 2

1.2.2 Electronic structure 3

1.3 Natural Allotropes 6

1.4 Synthetic Allotropes 8

1.4.1 Buckyballs (Spherical Fullerenes) 8

1.4.2 Carbon Nanotubes 9

1.4.3 Graphene 11

1.5 Current state of play 12

Bibliography **15**

2 Graphene: Theoretical Background **19**

2.1 Band structure of graphene 20

2.1.1 Real and reciprocal space 20

2.1.2 Tight binding model 22

2.1.3 Band structure 24

2.1.4 Dirac fermions 26

2.1.5 Trigonal warping 28

2.2 Weak localization 29

2.3 Anomalous half-integer quantum Hall effect 33
2.3.1 Classical Hall effect 33
2.3.2 Landau levels 35
2.3.3 Integer quantum Hall effect 38
2.3.4 Shubnikov-de Haas effect 40

Bibliography **43**

3 Device Fabrication and Measurement Techniques **47**
3.1 Graphene synthesis 48
3.1.1 Micro-mechanical exfoliation 48
3.1.2 Epitaxial growth on SiC 50
3.1.3 Chemical vapour deposition 51
3.2 Device fabrication 52
3.2.1 Electron beam lithography system 54
3.2.2 First lithographic stage 55
3.2.3 Resists 55
3.2.4 Development 57
3.2.5 Metal evaporation 58
3.2.6 Lift-off 61
3.2.7 Flake discovery and positioning 63
3.2.8 Subsequent lithographic stages 64
3.2.9 Ball bonding 67
3.3 Measurement apparatus 69

Bibliography **73**

4 Energy Relaxation for Hot Dirac Fermions in Graphene and Breakdown of the Quantum Hall Effect **75**
4.1 Introduction 76

4.2 Methodology 78
4.2.1 Sample preparation 78
4.2.2 Measurement and data processing 79
4.3 Results 80
4.3.1 Energy loss rate 80
4.3.2 Quantum Hall effect breakdown 87
4.4 Conclusions 91

Bibliography **93**

5 Energy Loss Rates of Hot Dirac Fermions in Epitaxial, Exfoliated and CVD Graphene **97**
5.1 Introduction 98
5.2 Methodology 100
5.3 Results 101
5.3.1 Shubnikov-de Haas 101
5.3.2 Weak-localization 105
5.3.3 Comparison of the energy loss rate techniques 107
5.3.4 Measured energy loss rates 108
5.4 Conclusions 111

Bibliography **113**

6 Weak Localization Scattering Lengths in Epitaxial, and CVD Graphene **117**
6.1 Introduction 118
6.2 Methodology and Theoretical Background 119
6.3 Results 125
6.3.1 Scattering lengths 125
6.3.2 Maximum currents 128
6.4 Conclusions 132

Bibliography **133**

7 Concluding Remarks **135**

7.1 Key Results 135

7.2 Future Work and Outlook 136

A Abbreviations **139**

Publications

A. M. R. Baker, J. A. Alexander-Webber, T. Altebaeumer, and R. J. Nicholas. Energy relaxation for hot Dirac fermions in graphene and breakdown of the quantum Hall effect. *Physical Review B*, **85**, 115403 (2012).

K. -C. Chuang, A. M. R. Baker and R. J. Nicholas. Magnetoabsorption study of Landau levels in graphite. *Physical Review B*, **80**, 161410(R) (2009).

J. A. Alexander-Webber, A. M. R. Baker, P. D. Buckle, T. Ashley, and R. J. Nicholas. High-current breakdown of the quantum Hall effect and electron heating in InSb/AlInSb. *Physical Review B*, **86**, 045404 (2012).

Manuscripts submitted/in preparation

A. M. R. Baker, J. A. Alexander-Webber, T. Altebaeumer, S. D. McMullan, T. J. B. M. Janssen, A. Tzalenchuk, S. Lara-Avila, S. Kubatkin, R. Yakimova, C. -T. Lin, L. -J. Li, and R. J. Nicholas. Energy loss rates of hot Dirac fermions in epitaxial, exfoliated and CVD graphene. *Submitted to Physical Review Letters.*

A. M. R. Baker, J. A. Alexander-Webber, T. Altebaeumer, S. D. McMullan, T. J. B. M. Janssen, A. Tzalenchuk, S. Lara-Avila, S. Kubatkin, R. Yakimova, C. -T. Lin, L. -J. Li, and R. J. Nicholas. Weak localization scattering lengths in epitaxial, and CVD graphene. *Submitted to Physical Review B.*

S. D. Stranks, A. M. R. Baker, B. Dirks, J. A. Alexander-Webber, and R. J. Nicholas. Production of High Purity Single Chirality Carbon Nanotube Hybrids by Selective Polymer Exchange. *Submitted to Journal of the American Chemical Society.*

J. A. Alexander-Webber, A. M. R. Baker, T. J. B. M. Janssen, A. Tzalenchuk, S. Lara-Avila, S. Kubatkin, R. Yakimova, and R. J. Nicholas. Ultra-high quantum Hall effect breakdown in epitaxial graphene *Manuscript in Preparation.*

Chapter 1

Introduction

This chapter introduces the principal topic of this thesis, graphene. It explains the motivation behind studying this material, the physical and historical context behind its discovery, and ends with a discussion of the current state of carbon research and commercialization.

1.1 Motivation

The 20$^{\text{th}}$ Century was a period of unprecedented growth in human knowledge and the associated technical expertise required to exploit this knowledge. It was the century that brought us antibiotics, radio communication, the car, and the computer, among countless other innovations and discoveries. It was also the century which brought man-made environmental destruction on an unprecedented scale, fast food, global pandemics and nuclear weapons. If the 21$^{\text{st}}$ Century is to capitalize on the opportunities and solve the problems bequeathed by the 20$^{\text{th}}$ Century, science and technological progress are going to be of critical importance.

An important component of this progress is expected to come from developments in novel materials. This thesis is concerned with one such novel material, a synthetic allotrope of carbon: graphene [1]. Graphene is a particularly exciting material due to its superlative physical and engineering properties, which include the highest ultimate tensile strength of any material [2], exceptionally high electron mobility at room temperature [3], the highest thermal conductivity of any material [4], and, perhaps its most remarkable feature of all, its two-dimensionality.

1.2 Carbon

1.2.1 Unique properties of carbon

Carbon is a truly exceptional element. Among the elements it is unique not only for the sheer number of compounds it can form (over twenty million organic compounds have been identified [5]) but also for the astonishing range of properties its allotropes possess. For instance, when we compare two everyday carbon allotropes, diamond and graphite,

the former has a hardness of 10 on the Mohs scale, is an electrical insulator, and is transparent [6, 7]. In contrast, the latter has a Mohs hardness of between 1 & 2, is a good electrical conductor, and is opaque [6, 7]. So how can two substances, composed in their entirety from the same element, have such dramatically different properties? The answer in large part is due to the different chemical bonds that a carbon atom can form to other carbon atoms. In order to understand these different bonds it is necessary first to understand the electronic structure of carbon.

1.2.2 Electronic structure

An isolated carbon atom has 4 valence electrons in a ground state configuration of $1s^2 2s^2 2p_x^1 2p_y^1$ [7], or more precisely,

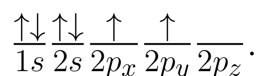

Looking at this structure and using simple models such as valence bond theory one might expect that carbon would form only two covalent bonds. However, carbon compounds with only two covalent bonds such as methylene (CH_2) can be highly unstable and even self-reactive [8]. In contrast, it is illuminating to examine what happens in simple, stable, carbon compounds such as methane (CH_4) which have four covalent bonds [9]. Examining methane, two things are immediately apparent: first, that there are four bonds from the carbon atom, one to each of the hydrogen atoms; second, that each of these bonds have equal strength [10]. This second point is especially important since if, for example, it was simply that a 2s electron were promoted into a 2p orbital, the differing amounts of orbital overlap would imply that the bonds between the carbon atom and some of the hydrogen atoms would be weaker than others, and this is not

observed to be the case. So how can there be four bonds of equal strength from the carbon atom? The answer lies in orbital hybridization.

Unhybridized:

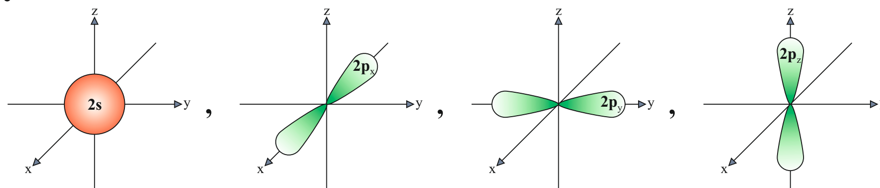

SP:

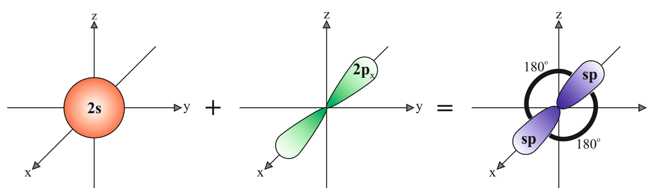

SP^2:

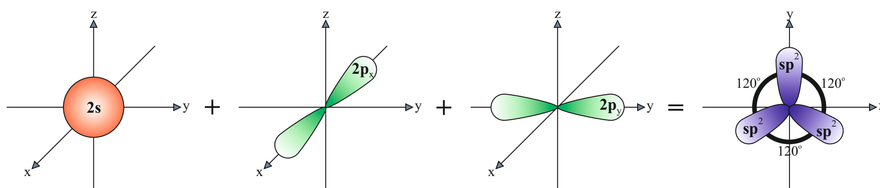

Sp^3:

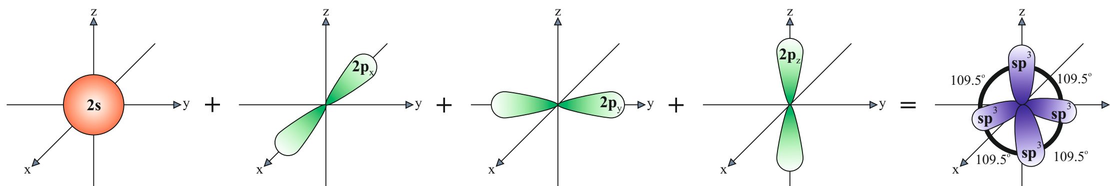

Figure 1.1: The four valence bonds of carbon are shown before hybridization, and subsequently for the three linear combinations of orbitals to give sp, sp^2, and sp^3 hybrid orbitals.

Orbital hybridization is the linear mixing of two or more atomic orbitals to form new hybrid orbital states. It transpires that carbon can form three different linear combinations of its outer s and p-orbitals [7] known as: sp, sp^2, and sp^3 (Fig. 1.1). One way to envisage hybridization is to imagine an intermediary stage where an electron is promoted from a 2s to a 2p orbital forming an excited state of carbon:

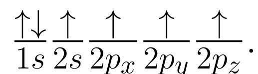

The energy required to excite the electron can be obtained by the much greater energy which is obtained from the formation of a bond.

In sp^3 the final electron configuration becomes [7]

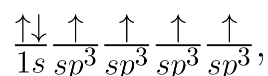

where each of the four orbitals has a 25% s-orbital character and 75% p-orbital character. Each of the sp^3 hybrid orbitals are directional with an angle of 109° from each of the others.

In sp^2 the configuration becomes [7]

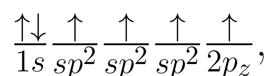

where each of the three sp^2 orbitals has a 50% s-orbital character and 50% p-orbital character, the final orbital remains pure $2p_z$. Each of the hybrid orbitals are coplanar and are again directional with an orbital angle of 120° between each pair of orbitals. The remaining $2p_z$ orbital is perpendicular to the plane of the three sp^2 bonds.

Lastly, the sp hybrid orbital has the following configuration [7]:

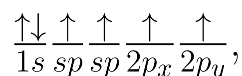

where the two sp orbitals both have 50% s-orbital and 50% p-orbital character, with the other two bonds remaining pure $2p_x$ and $2p_y$. The two sp bonds have an angle of 180°

between each other, whilst the $2p_x$ and $2p_y$ bonds lie in the plane perpendicular to that of the sp bonds.

In general, carbon-carbon bonds formed from two sp^3 σ-bonds are the weakest of the three, and bonds formed from two sp σ-bonds are the strongest [11]. This picture is complicated, however, by the possibility of double or triple bonds where additional π bonds reinforce the σ-bonds between the two carbon atoms. The double and triple bonds are both far stronger than any of the possible single carbon-carbon bonds [11].

1.3 Natural Allotropes

Figure 1.2: Photos showing the three main types of naturally occurring carbon allotropes. Bituminous coal is a commonplace example of amorphous carbon, another common example would be soot. The rough diamond shows the state in which diamonds are typically found. The diamond is in a rough octahedral shape, and is embedded in another mineral. The third picture shows natural graphite as it is characteristically found. Naturally occurring graphite is typically polycrystalline. All photos are from the "Minerals in Your World" project, which is a collaboration between United States Geological Survey and the nonprofit Mineral Information Institute.

There are three naturally occurring allotropes of carbon: amorphous carbon, diamond, and graphite. Two of these, diamond and amorphous carbon, have probably been known

since prehistoric times. Curiously, while there is some evidence for its use in prehistoric times, graphite was not (re)discovered until the 16th Century [12].

Amorphous carbon is the simplest of the three. Coal and soot, among other impure carbon materials, are often classified as amorphous carbon though this is imprecise since in practice these are in part polycrystalline with many non-carbon impurities. Amorphous carbon has no long-range crystalline structure and is formed from a random assortment of bond types.

Diamond is formed from a tetragonal structure of carbon atoms where each atom is bonded to four others with a single sp^3 σ-bond between each pair of atoms. Each of these bonds is very strong and directionally locked causing diamond crystals to be very rigid, which in turns leads to their extreme hardness and thermal conductivity [6]. This hardness makes diamond useful in processes such as industrial grinding and abrasive applications. Further, because of the extreme rigidity of its lattice, only a very few impurities can contaminate it, contributing to the rarity of strongly-coloured diamonds [13]. Because of their purity and characteristic lustre, diamonds have been in demand for adornments and decorations since prehistoric times.

Graphite is formed by a series of stacked sheets of graphene [6]. Each of these sheets is formed of a hexagonal "chicken-wire" lattice of carbon atoms, with each carbon atom connected to three others in a sheet by sp^2 σ-bonds. Above and below each sheet the remaining $2p_z$ electrons are delocalised, forming π-bands. These delocalised electrons give rise to the large electrical and thermal conductivity of graphite [6, 9]. This π-band also creates a weak van der Waals force between multiple sheets, allowing them to stack to form graphite. Further, this weak bonding between the layers allows fluids such as air and water readily to build up between the layers, which makes graphite an excellent lubricant outside vacuum conditions [14]. This is the property exploited when graphite

is used for that most familiar of graphite applications, the “lead” pencil.

1.4 Synthetic Allotropes

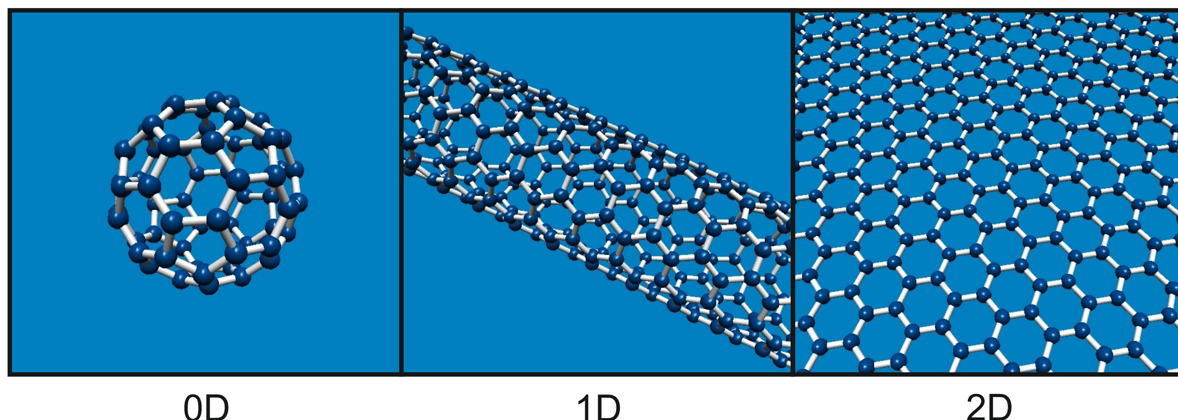

Figure 1.3: Synthetic allotropes of carbon are shown, ordered by the dimension of the molecule. The first molecule, labelled 0D, is a C_{60} molecule, which is a member of the fullerene molecular family. The second molecule, labelled 1D, is a single-walled carbon nanotube with (6,5) chirality. The final molecule, labelled 2D, is a monolayer of graphene.

1.4.1 Buckyballs (Spherical Fullerenes)

For over four centuries amorphous carbon, graphite and diamond were assumed to be the only carbon allotropes. In the second half of the 20th century, however, several theoretical suggestions of possible new carbon structures were made. In 1965 $C_{60}H_{60}$ was proposed as a possible structure by Harry Schultz [15], and this was quickly followed by predictions of C_{60} by three separate groups: Eiji Osawa [16] and R.W. Henson [17] both in 1970, and D.A. Bochvar [18] in 1973. Unfortunately, none of these predictions was widely accepted, and for the most part they were assumed to be “toy models”. All this changed in 1985 when Harold Kroto *et al.* [19] recorded a mass spectrum anomaly

equating to a mass of 60 carbon atoms. In the paper, they correctly surmised that this C_{60} molecule would form a spherical polygon with 60 vertices, 32 faces, of which 12 are pentagonal and 20 hexagonal (Fig. 1.3). This is the same shape as a "standard" football. Every carbon atom in the molecule is bonded to three others. These bonds are predominately sp^2 bonds with the 4th p_z electron forming a π-band. However, due to the curvature of the surface of the molecule, these sp^2 are in practice an admixture of predominantly sp^2 with a small sp^3 component [7]. Since the discovery of C_{60} a whole family of similar spherical fullerene molecules, known colloquially as "buckyballs", has been synthesized.

To date, proposed applications of fullerenes are still at the research stage, though there has been much excitement around using C_{60} to encapsulate atoms or small molecules, protecting them until needed [20], as well as for use as biological tracers [21]. Further uses include their use in organic electronics and low-cost organic solar cells.

1.4.2 Carbon Nanotubes

The discovery of buckyballs was followed, just six years later, with the discovery of carbon nanotubes (CNTs). There have been multiple suggestions [22, 23] of earlier discoveries of CNTs but none of these were sufficiently convincing or well-described to gain widespread acceptance in the community. CNTs in their multi-wall form were brought to widespread awareness by Sumio Iijima [24] in 1991, an achievement which he quickly followed up just two years later with the discovery of the single-walled form [25]. A CNT can be thought of as a single atomic sheet taken from a bulk graphite crystal (graphene) rolled up to form a tube (Fig. 1.3). There is no need for this "rolling up" to proceed along any special, high-symmetry, direction, and hence these sheets can form an infinite number of different, wrapping spirals. An alternate model for thinking about

CNTs is to regard them as "extended" buckyballs. The chemical structure of CNTs is similar to that of the fullerenes with 3 sp^2 bonds, again with a slight admixture of sp^3, as in fullerenes [26]. The sp^2 bonds form to the three adjacent carbon atoms along the surface of the tube, with π-bands inside and outside the tube originating from the $2p_z$ electron. One curious property of a CNT is that tubes with similar diameters can have very different electrical properties. Taking two near-identical tubes, it is possible for one to be metallic and the other semi-conducting. The reason for this is that while the dispersion relation is effectively continuous along the axial direction (the tube for purposes of band-structure calculations is essentially infinite in this direction) it is well quantized along the tube circumference. For wavefunctions travelling around the circumference, only those with wavelengths equal to integer multiples of the circumference do not destructively interfere and hence remain extant. The band structure of CNTs, before the modification for the quantization from the circumference, is the same as that of graphene which is covered in greater detail in section 2.1. Graphene's band structure has only a few discrete points in reciprocal space (the K and K' points) where the conduction and valence bands approach each other. The combination of these few discrete touching points, and the quantization from the circumference, leads to there only being permissible wavefunctions at the K or K'-points for some wrapping angles. Where there are such wavefunctions, the CNT is metallic, otherwise it is semiconducting. This is the reason for CNTs with similar diameters having dramatically different properties. Therefore, a major problem for applications of CNT is the great difficulty associated with growing, or purifying them, to obtain a single "species" or type (i.e. metallic or semiconducting) of CNT.

These difficulties have meant that despite major recent strides in purifying CNTs [27, 28], the current uses are largely limited to the bulk use of nanotubes for structural or electrical conduction purposes, e.g. for sporting equipment (structural), and wind

turbine blades (structural, lightning conduction) [29]. Several advanced technological applications, however, may be nearing the marketplace, including use as an ITO replacement (a transparent conductor needed for touchscreens and most flat screen displays) [30], and use in ultracapacitors [31].

1.4.3 Graphene

Graphene was discovered in 2004 by Andre Geim and Konstantin Novoselov [1] using a process known as micromechanical exfoliation: the process essentially consists of using two pieces of sellotape to repeatedly separate graphite into successively thinner layers. A full description is given in section 3.1.1. Graphene can be thought of as a single atomic sheet taken from bulk graphite, but as we shall see in chapter 2, it has dramatically different properties to that found in bulk graphite. The structure of graphene is that of carbon atoms arranged in a planar hexagonal honeycomb lattice with each carbon atom bonded to three others with sp^2 bonds (Fig. 1.3). Above and below, a π band is formed from the delocalized p_z electrons.

Due to the recent discovery of graphene, applications are yet to come to market. However, the number of proposed uses for graphene is truly staggering. The most promising applications in the short-term are probably for use in transparent conductors (possibly in conjunction with CNTs) [32], and in the field of analogue electronics [33] and electromechanical components [34]. Its use as a transparent conductor seems imminent; it is anticipated that Samsung will bring out devices based on the technology before the end of 2012 [35].

1.5 Current state of play

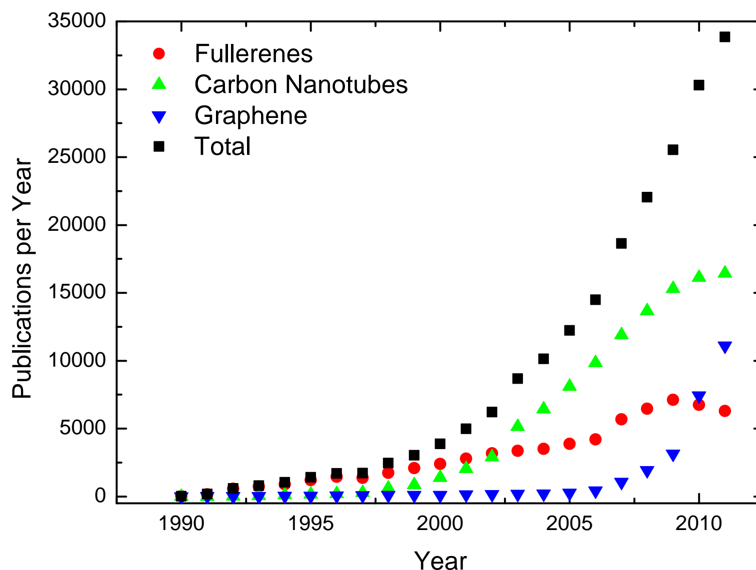

Figure 1.4: Growth in publications of three classes of synthetic carbon allotropes: fullerenes, carbon nanotubes and graphene. Data is collected from ISI Web of Knowledge for the years 1990 through to the last complete year available, 2011.

It is hard to overstate the level of excitement that has built up in recent years around carbon nano-materials [36, 37]. As can be seen from Fig. 1.4, there are a truly staggering number of publications on such materials each year, with over 6,000 on fullerenes, 16,000 on carbon nanotubes, and 11,000 on graphene in 2011 alone. In addition two Nobel prizes have been awarded for synthetic carbon allotropes: the 1996 Nobel Prize in Chemistry was awarded to Robert Curl, Sir Harold Kroto and Richard Smalley for “their discovery of fullerenes”, and the 2010 Nobel Prize in Physics was awarded to Andre Geim and Konstantin Novoselov for “groundbreaking experiments regarding the two-dimensional material graphene”.

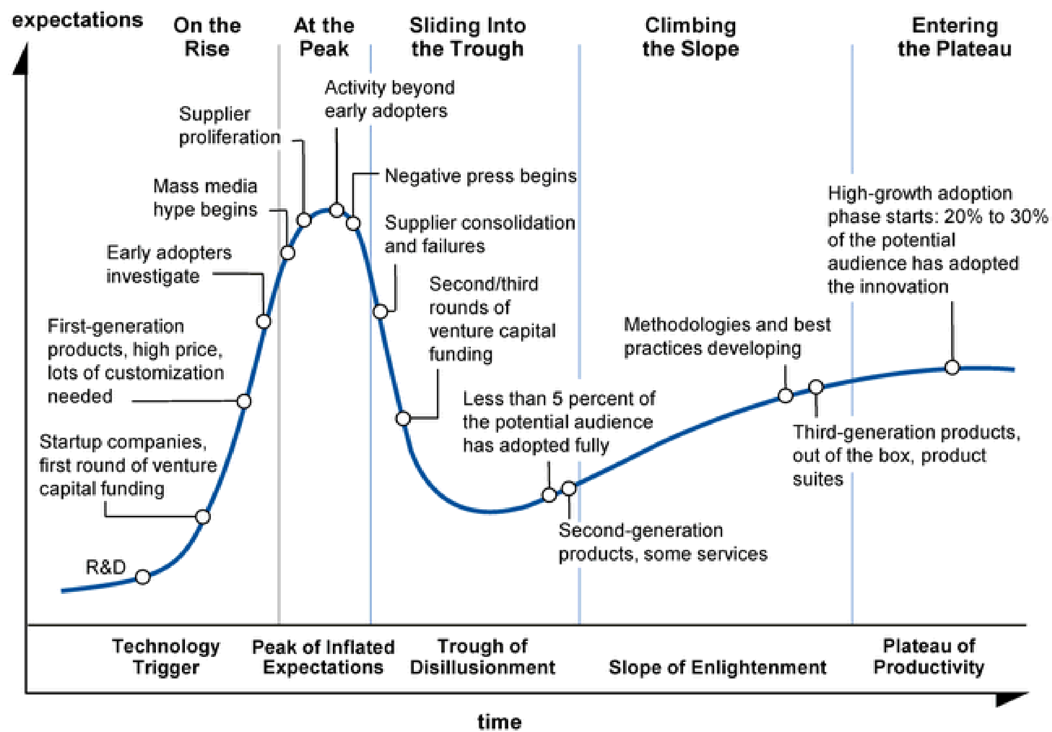

Figure 1.5: Diagram from Gartner's Hype Cycle Special Report 2011 [38] which displays a model developed in 1995 to describe the various stages through which new technologies typically pass.

So, do these carbon nano-materials, and particularly graphene, stand up to the hype? Shown in Fig. 1.5 is a common model used in industry that describes and characterizes the stages which most new and ultimately successful technologies pass through. This model was developed in 1995 to illustrate visually, the over-enthusiasm that new technologies go through prior to a recalibration with reality, and leading to a final development to productivity and acceptance. The basic idea is that expectations of any new technology typically become overinflated before collapsing into a "Trough of Disillusionment". Successful technologies manage eventually to pull themselves out of this trough as high quality products and applications begin to emerge. Unsuccessful ones never recover from the 'Trough of Disillusionment" phase. In this model, carbon nano-materials would still be firmly on the left hand side of this peak. It seems likely

then that at some time, perhaps in the next few years, this expectations bubble will burst and the level of negative press will dramatically increase. So will carbon nanomaterials be one of the ultimately successful technologies? I would suggest that the answer is yes, especially for graphene. The sheer number of proposed applications it has attracted, together with its low cost, suggest that at least a few of these should succeed in either the commercial [39] or the scientific realm [40].

Bibliography

[1] K. S. Novoselov, A. K. Geim, S. V. Morozov, D. Jiang, Y. Zhang, S. V. Dubonos, I. V. Grigorieva, and A. A. Firsov, Science **306**, 666 (2004).

[2] C. Lee, X. Wei, J. W. Kysar, and J. Hone, Science **321**, 385 (2008).

[3] K. S. Novoselov, Z. Jiang, Y. Zhang, S. V. Morozov, H. L. Stormer, U. Zeitler, J. C. Maan, G. S. Boebinger, P. Kim, and A. K. Geim, Science **315**, 1379 (2007).

[4] S. Chen, Q. Wu, C. Mishra, J. Kang, H. Zhang, K. Cho, W. Cai, A. A. Balandin, and R. S. Ruoff, Nat. Mater. **11**, 203 (2012).

[5] A. H. Lipkus, Q. Yuan, K. A. Lucas, S. A. Funk, W. F. Bartelt, R. J. Schenck, and A. J. Trippe, J. Org. Chem. **73**, 4443 (2008).

[6] J. Spencer, G. Bodner, and L. Rickard, *Chemistry: Structure and Dynamics*, 5th ed. (John Wiley & Sons, 2011).

[7] N. Yahya, *Carbon and Oxide Nanostructures: Synthesis, Characterisation and Applications*, 1st ed., Advanced Structured Materials (Springer, 2011).

[8] M. Lazar, *Free Radicals in Chemistry and Biology*, 1st ed. (CRC Press, 1989).

[9] W. Haynes, *CRC Handbook of Chemistry and Physics*, 92nd ed. (CRC Press, 2011).

[10] F. A. Carey and R. J. Sundberg, *Advanced Organic Chemistry: Structure and Mechanisms*, 4th ed. (Springer, 2004).

[11] J. Bloor and S. Gartside, Nature **184**, 1313 (1959).

[12] S. Zumdahl and S. Zumdahl, *Chemistry*, 7th ed. (Houghton Mifflin, 2006).

[13] L. Pan, *Diamond: Electronic Properties and Applications*, 1st ed. (Springer, 1995).

[14] Y. N. Vasil'ev, I. A. Kolyaev, and V. A. Fugol', J. Frict. Wear. **32**, 324 (2011).

[15] H. P. Schultz, J. Org. Chem. **30**, 1361 (1965).

[16] E. Osawa, Kagaku **25**, 854 (1970).

[17] P. A. Thrower, Carbon **37**, 1677 (1999).

[18] D. Bochvar and E. Galpern, Dokl. Acad. Nauk SSSR **209**, 610 (1973).

[19] H. W. Kroto, J. R. Heath, S. C. O'Brien, R. F. Curl, and R. E. Smalley, Nature **318**, 162 (1985).

[20] K. Komatsu, M. Murata, and Y. Murata, Science **307**, 238 (2005).

[21] T. Ohtsuki, K. Masumoto, K. Shikano, K. Sueki, T. Tanaka, and K. Komatsu, Biol. Trace Elem. Res. **71-72**, 489 (1999).

[22] M. Monthioux and V. Kuznetsov, Carbon **44**, 1621 (2006).

[23] L. V. Radushkevich and L. V. M., Zurn. Fisic. Chim. **26**, 88 (1952).

[24] S. Iijima, Nature **354**, 56 (1991).

[25] S. Iijima and T. Ichihashi, Nature **363**, 603 (1993).

[26] S. Reich, C. Thomsen, and J. Maultzsch, *Carbon Nanotubes: Basic Concepts and Physical Properties*, 1st ed. (John Wiley & Sons, 2004).

[27] A. Nish, J.-Y. Hwang, J. Doig, and R. J. Nicholas, Nat. Nanotech. **2**, 640 (2007).

[28] M. C. Hersam, Nat. Nanotech. **3**, 387 (2008).

[29] J. Garcia-Martinez and E. Serrano-Torregrosa, *The Chemical Element: Chemistry's Contribution to Our Global Future*, 1st ed. (Wiley VCH, 2011).

[30] H.-Z. Geng, K. K. Kim, K. P. So, Y. S. Lee, Y. Chang, and Y. H. Lee, J. Am. Chem. Soc. **129**, 7758 (2007).

[31] M. Kaempgen, C. K. Chan, J. Ma, Y. Cui, and G. Gruner, Nano Lett. **9**, 1872 (2009).

[32] S. Bae, H. Kim, Y. Lee, X. Xu, J.-S. Park, Y. Zheng, J. Balakrishnan, T. Lei, H. R. Kim, Y. I. Song, Y.-J. Kim, K. S. Kim, B. Ozyilmaz, J.-H. Ahn, B. H. Hong, and S. Iijima, Nat. Nanotech. **5**, 574 (2010).

[33] K. Bourzac, Nature **483**, S34 (2012).

[34] J. S. Bunch, A. M. van der Zande, S. S. Verbridge, I. W. Frank, D. M. Tanenbaum, J. M. Parpia, H. G. Craighead, and P. L. McEuen, Science **315**, 490 (2007).

[35] K. S. Novoselov (Nobel Prize Lecture, 2010).

[36] A. K. Geim and K. S. Novoselov, Nat. Mater. **6**, 183 (2007).

[37] A. H. Castro Neto, F. Guinea, N. M. R. Peres, K. S. Novoselov, and A. K. Geim, Rev. Mod. Phys. **81**, 109 (2009).

[38] J. Fenn, *Gartner's Hype Cycle Special Report for 2011* (Gartner, 2011).

[39] X. Li, W. Cai, J. An, S. Kim, J. Nah, D. Yang, R. Piner, A. Velamakanni, I. Jung, E. Tutuc, S. K. Banerjee, L. Colombo, and R. S. Ruoff, Science **324**, 1312 (2009).

[40] A. Tzalenchuk, S. Lara-Avila, A. Kalaboukhov, S. Paolillo, M. Syväjärvi, R. Yakimova, O. Kazakova, T. J. B. M. Janssen, V. Fal'ko, and S. Kubatkin, Nat. Nanotech. **5**, 186 (2010).

Chapter 2

Graphene: Theoretical Background

This chapter gives a brief introduction to the theoretical framework required to understand the results presented in this thesis. The first part of this chapter gives an introduction to the band structure of graphene including its calculation using the tight binding model. The second part of the chapter covers weak localization and the scattering times that contribute to form it. Finally this chapter covers the anomalous quantum Hall effect in graphene.

2.1 Band structure of graphene

2.1.1 Real and reciprocal space

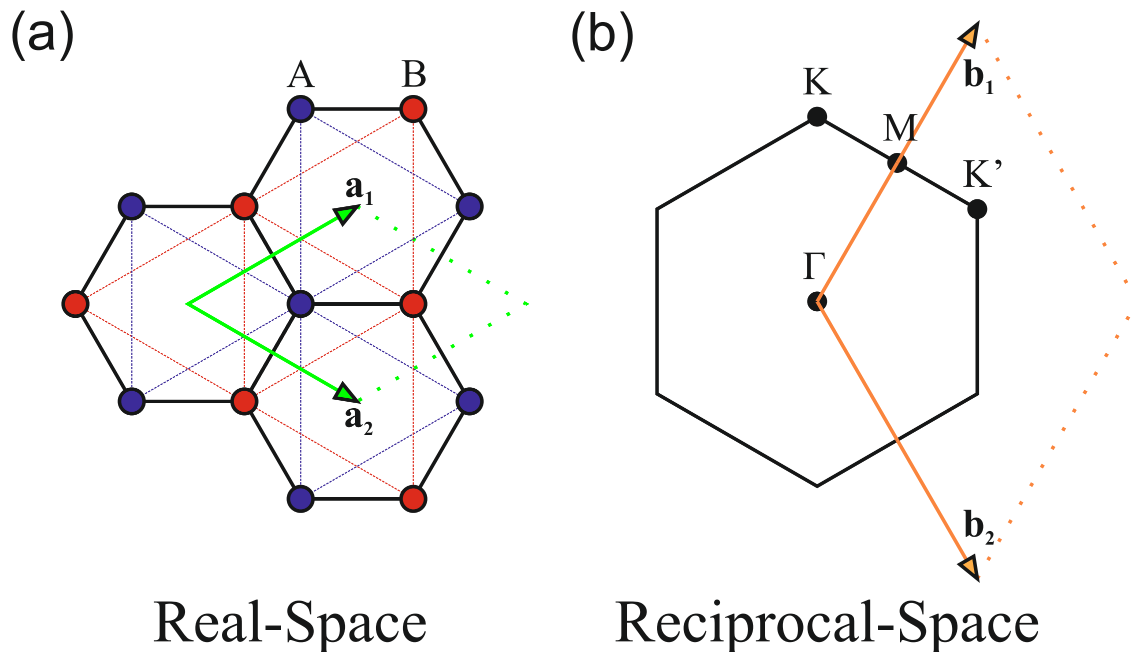

Figure 2.1: The real and reciprocal-space representations of the graphene lattice [1]. (a) Real-space representation of the graphene lattice with the two equivalent sublattices shown in blue(A) and red(B). The real-space unit cell with real-space lattice vectors are marked in green with the two vectors labelled, $\mathbf{a}_1$ and $\mathbf{a}_2$. (b) Reciprocal-space representation of the graphene lattice. The high-symmetry points K, K', Γ, and M are marked on the figure. In addition the reciprocal lattice unit cell is marked in orange, with the reciprocal lattice vectors $\mathbf{b}_1$ and $\mathbf{b}_2$ also shown.

As described in section 1.4.3, and shown in Fig. 2.1 (a) graphene is formed from a hexagonal lattice of carbon atoms. This hexagonal lattice can alternatively be thought of as two interpenetrating triangular sublattices [1]. These are shown in blue and red on Fig. 2.1 (a). The two real-space lattice vectors, for the hexagonal lattice are defined as

$$\mathbf{a}_1 = a_0 \left(\frac{\sqrt{3}}{2}, \frac{1}{2} \right), \ \mathbf{a}_2 = a_0 \left(\frac{\sqrt{3}}{2}, -\frac{1}{2} \right), \tag{2.1}$$

where $\mathrm{a}_0 = \sqrt{3}a_{C-C}$, with a_{C-C} as the length of the carbon-carbon sp^2 bond. These are the bonds which form the plane in graphene, and their length has been measured as 0.142 nm [2]. A unit cell consisting of these lattice vectors is marked in green. The basis of the full lattice consists of two carbon atoms, A and B, marked in blue and red respectively on the figure. With the lattice vectors defined as above, the two carbon atoms are to be found at $\frac{1}{3}(\mathbf{a}_1+\mathbf{a}_2)$ and $\frac{2}{3}(\mathbf{a}_1+\mathbf{a}_2)$.

Fig. 2.1 (b) shows the reciprocal space representation of the graphene lattice. The reciprocal-space lattice is the fourier transform of the real-space lattice. The reciprocal lattice vectors can be defined using $e^{i\mathbf{K}\cdot\mathbf{R}} = 1$, where $\mathbf{K}$ is the reciprocal-space lattice vector and $\mathbf{R}$ is the real-space lattice vector. From this we calculate the reciprocal lattice vectors as

$$\mathbf{b}_1 = \frac{2\pi}{a_0} \left(\frac{1}{\sqrt{3}}, 1 \right), \ \mathbf{b}_2 = \frac{2\pi}{a_0} \left(\frac{1}{\sqrt{3}}, -1 \right). \tag{2.2}$$

These vectors are shown on Fig. 2.1 (b) together with the corresponding unit cell marked in orange. Also marked on the figure are the K, K', Γ, and M high-symmetry points. The two points, K and K', are inequivalent, and are known as the Dirac points for reasons which are explained in section 2.1.4. They have a particular importance which is explained in the following sections.

2.1.2 Tight binding model

The band structure of graphene was first calculated in 1947 by Wallace [2] using a tight-binding model. As discussed in section 1.4.3 the carbon atoms in graphene each form three sp^2 hybrid orbitals, and have one remaining unhybridized 2p orbital. The three sp^2 orbitals form strong σ bonds in the plane of the graphene lattice, and play no significant part in electrical conduction due to their distance from the Fermi level [3]. Recalling that there are two carbon atoms per primitive unit cell this means we are left with two, 2p bonds per cell which form π bonding, and π^* antibonding bands, above and below the plane of the lattice [4]. The simple tight-binding model confines its calculations to these π bands, since it is these bands which cross at the Fermi level, and hence it is these bands which play the significant role of conduction in graphene.

In calculating the electronic energy bands there are two basic approaches which can be taken. The first, is the nearly-free electron model which treats electrons as weakly-bound particles perturbed by a periodic potential. This potential arises both from the atoms in the lattice, and from other electrons [5]. In contrast, the tight binding approach takes the opposite extreme in which electrons are considered to be tightly bound to their respective atoms, with valence electrons allowed to interact weakly with those in other atoms. This allows the electron eigenstates to broaden to form continuous bands in the crystal [3, 5]. The tight binding model is the conventional approach taken in simple modelling of the band structure of graphene.

Nowadays the best known tight-binding approximation comes from Saito *et al.* [10]. This model considers interactions only between nearest neighbours, additionally considering non-zero overlap between basis functions [6]. In contrast Wallace's derivation [2] includes next-nearest neighbours but ignores the overlap. While the derivation that follows is not as precise as versions which include a greater number of neighbours [6], or

those based on *ab initio* approaches [7], it does give a good quantitative approximation of the band structure especially around the K and K' high-symmetry points. Saito's full derivation can be found in references [3] and [10]. His expression for the electronic energy band is

$$E^{\pm}(\mathbf{k}) = \frac{\epsilon_{2p} \pm \gamma_0 \sqrt{f(\mathbf{k})}}{1 \pm s_0 \sqrt{f(\mathbf{k})}}. \tag{2.3}$$

where

$$f(\mathbf{k}) = 3 + 2\cos(\mathbf{k} \cdot \mathbf{a}_1) + 2\cos(\mathbf{k} \cdot \mathbf{a}_2) + 2\cos(\mathbf{k} \cdot (\mathbf{a}_1 - \mathbf{a}_2)). \tag{2.4}$$

The two solutions, E^- and E^+, correspond to the valence (π) and conduction (π^*) bands respectively [3]. The three constants in Eq. (2.3), ϵ_{2p}, γ_0, and s_0 correspond to, (ϵ_{2p}) the energy of the 2p state of an isolated atom modified by the periodic crystal potential, (γ_0) the carbon-carbon interaction energy, and (s_0) the overlap integral between two neighbouring carbon atoms respectively [3, 6]. These three constants are often used as fitting parameters, but can also be obtained via *ab initio* calculations [8].

2.1.3 Band structure

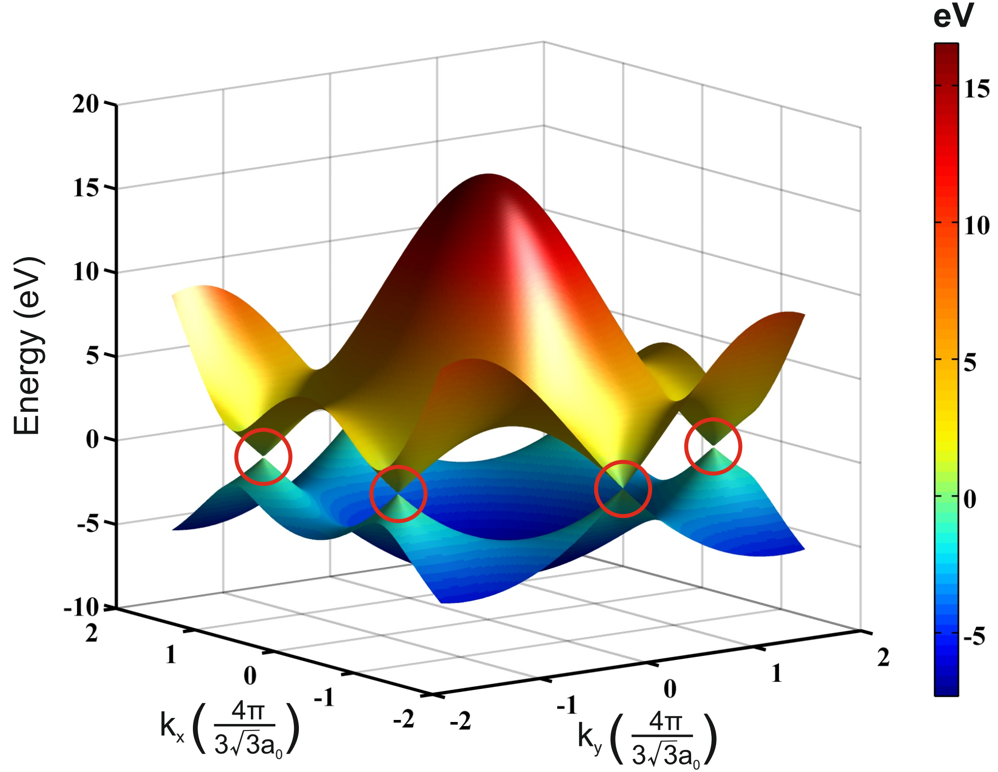

Figure 2.2: 3D plot showing the band structure of graphene. Plot calculated with Eq. (2.3) using $\epsilon_{2p} = 0$ [3], $\gamma_0 = 3.38$eV [9], and $s_0 = 0.129$ [10]. Clearly visible on the figure are the the points where the conduction and valence bands touch. These points are circled in red for clarity, and are known as the Dirac points.

Fig. 2.2 shows a typical theoretical calculation of the band structure using Eq. (2.3). ϵ_{2p} in the figure was set to zero by inspection of Eq. (2.4), noting that $f(\mathbf{k})$ goes to zero at the K $(\frac{1}{3}\mathbf{b}_1+\frac{2}{3}\mathbf{b}_2)$ and K' $(\frac{2}{3}\mathbf{b}_1+\frac{1}{3}\mathbf{b}_2)$ points and that the Fermi level passes through these points. γ_0 has been previously measured from cyclotron resonance by Deacon *et al.* [9] at 3.38eV. Finally in this theoretical calculation s_0 has been set to 0.129 to align this calculation as closely as possible to *ab initio* calculations [10]. Often, however, s_0 is set to zero which allows us to simplify Eq. (2.3) and Eq. (2.4) to

$$E^{\pm}(\mathbf{k}) = E^{\pm}(k_x, k_y) = \pm\gamma_0\sqrt{1 + 4\cos\left(\frac{\sqrt{3}k_x a_0}{2}\right)\cos\left(\frac{k_y a_0}{2}\right) + 4\cos^2\left(\frac{k_y a_0}{2}\right)}. \quad (2.5)$$

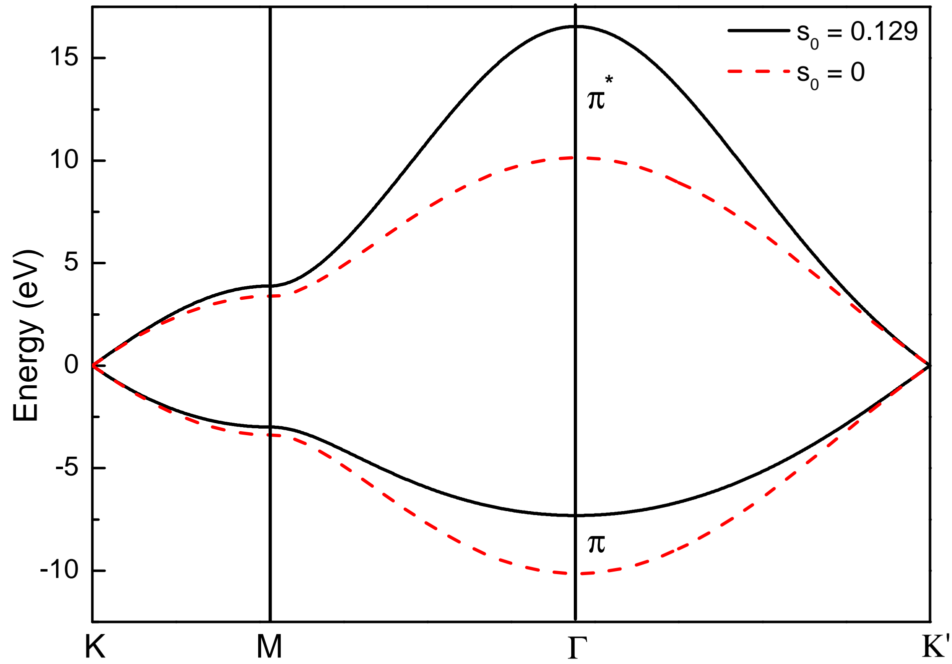

Figure 2.3: A comparison of the band structure for two different values of s_0 (the overlap integral), along straight line paths between the high-symmetry points. At the Dirac points (K, K') the two line up nearly perfectly, in contrast to the Γ point, where the $s_0 = 0$ calculation is nearly 50% lower than the $s_0 = 0.129$ calculation.

As Fig. 2.3 demonstrates, the agreement between $s_0 = 0$ and $s_0 = 0.129$ is very good around the K and K' points. However, the agreement becomes significantly worse as we get further from these points. Thus Eq. (2.5) is useful in describing the behaviour of carriers, but only for the region around these points.

2.1.4 Dirac fermions

Taking Eq. (2.5) and expanding around either the $\mathbf{K} = \left(\frac{2\pi}{\sqrt{3}a_0}, \frac{-2\pi}{3a_0}\right)$ or $\mathbf{K'} = \left(\frac{2\pi}{\sqrt{3}a_0}, \frac{2\pi}{3a_0}\right)$ point gives

$$E^{\pm} = \pm\hbar v_F|\kappa| \tag{2.6}$$

where $\kappa = \mathbf{k} - \mathbf{K}_D$, and $\mathbf{K}_D$ can be any of the K or K' high-symmetry points. The Fermi velocity, v_F, is defined as

$$v_F = \frac{\sqrt{3}\gamma_0 a_0}{2\hbar}. \tag{2.7}$$

Examination of the form of Eq.(2.6) reveals the extraordinary result that the dispersion relation around this point is linear. This implies that the Fermi velocity of the carriers is independent of their energy while near these K/K' points, and that they can be thought of as mimicking relativistic particles with a reduced "speed of light" of around $v_F = 1.1 \times 10^6$ ms^{-1} [9]. This means that unlike nearly every other known material, the electronic properties of graphene are better described by the Dirac equations than the Schrödinger equation [11, 12]. More precisely, at low energies the carriers in graphene can be described by massless quasiparticles known as Dirac fermions, using the (2+1)-dimensional Dirac equation. This is the origin of the label "Dirac points" being applied to the K and K' high-symmetry points. The two valleys, centred on the K and K' points, originate from the two inequivalent triangular sublattices [11], A and B, that make up graphene as shown in Fig. 2.1. The Dirac fermions within each valley can be described by

$$\hat{H} = \hbar v_F \begin{pmatrix} 0 & k_x - ik_y \\ k_x + ik_y & 0 \end{pmatrix} = \hbar v_F \boldsymbol{\sigma} \cdot \mathbf{k}, \tag{2.8}$$

where $\boldsymbol{\sigma}$ is the 2D Pauli matrix. However, unlike the usual case where the Pauli matrix is used to represent spin, $\boldsymbol{\sigma}$ is instead used in this case to represent pseudospin, i.e it represents the relative contribution of the two sublattices to the quasiparticle. There is a related quantity to pseudospin known as chirality which can be defined as the projection of $\boldsymbol{\sigma}$ along the direction of motion, where $\mathbf{k}$ is positive for electrons and negative for holes [11].

2.1.5 Trigonal warping

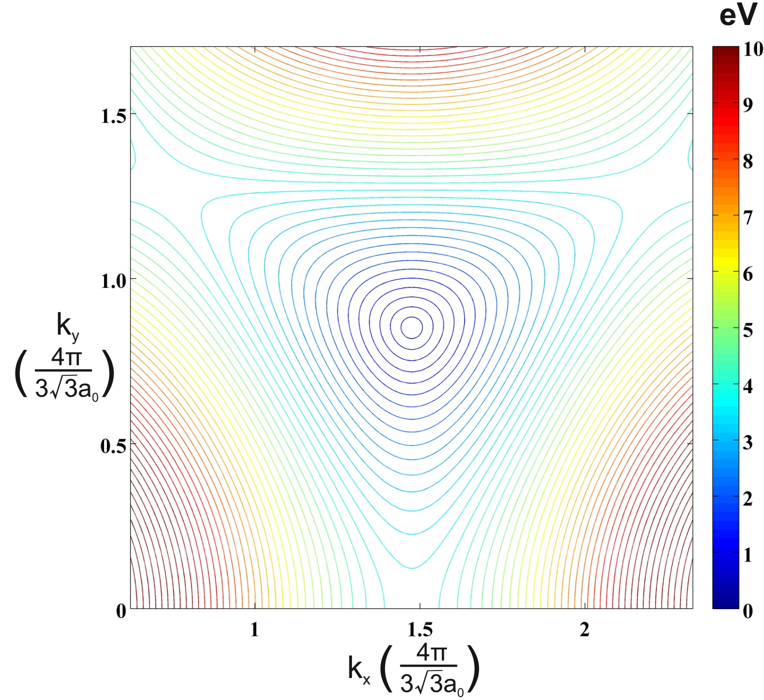

Figure 2.4: An energy contour plot centred around one of the Dirac points. Plot of E^+ values calculated using Eq. (2.3) with $\epsilon_{2p} = 0$ [3], $\gamma_0 = 3.38$eV [9], and $s_0 = 0.129$ [10]. The plot clearly demonstrates the effect of trigonal warping distortion for energies above $\sim$ 1eV, in contrast to the linear dispersion expected in Eq. (2.6).

One final band structure effect worth examining briefly is that of trigonal warping. Looking at Eq. (2.6) we would expect the band structure to form a conical shape around the K and K' points. Such a conical shape would appear in a contour plot of energy as concentric circles around these points. This is indeed what we see in Fig. 2.4 for low energies. However, for energies greater than $\sim$ 1eV [11] this circular shape starts distorting and becoming more triangular. This asymmetry in the Fermi surface can give rise to additional trigonal warping scattering terms, as discussed in the following sections.

2.2 Weak localization

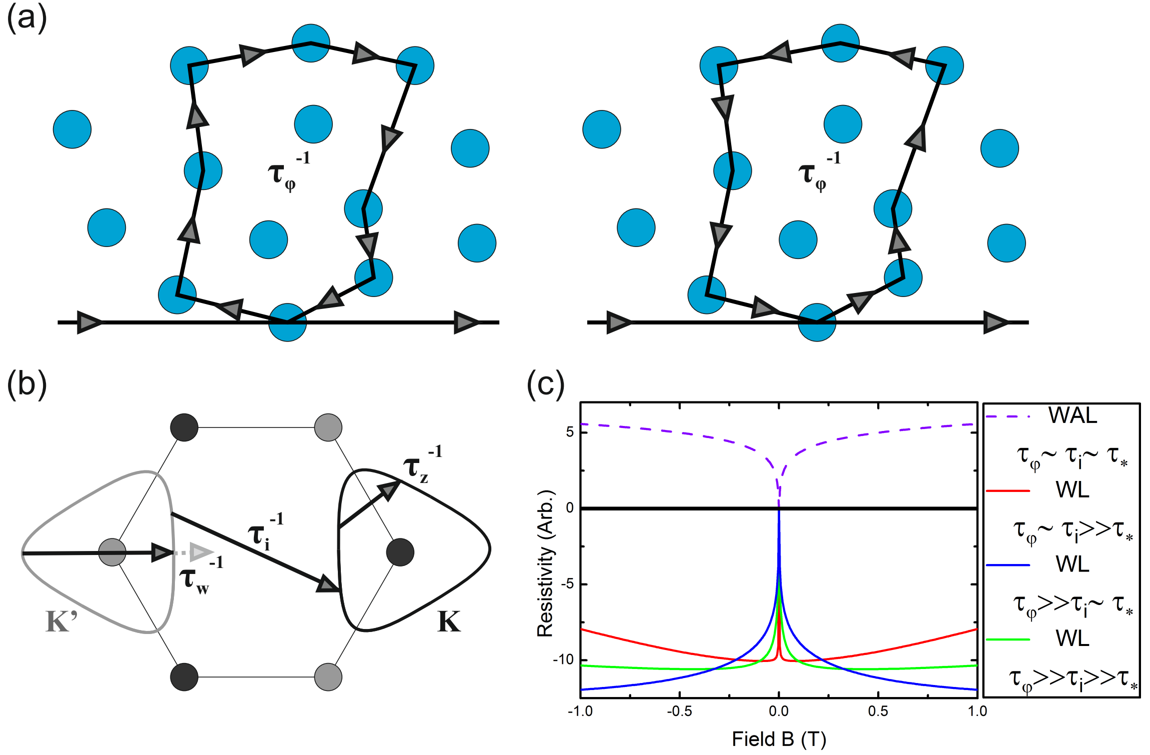

Figure 2.5: Illustration of the scattering processes which contribute to weak (anti)localization. (a) Two example scattering paths, identical except for the direction of travel around the loop, the size of which is determined by τ_φ^{-1}, the dephasing rate. (b) The two rounded triangles centred on the two inequivalent Dirac points, K, K' are shown for a small Fermi energy such that trigonal warping is clearly apparent. Three scattering terms, and how they contribute, are superimposed on this Fermi surface: τ_i^{-1}, the elastic intervalley scattering rate, τ_w^{-1}, the elastic intravalley trigonal warping scattering term and τ_z^{-1} the elastic intravalley chirality breaking scattering term. (c) Illustrates the shape of the weak (anti)localization effect for several different realistic regimes of the relative magnitude of the scattering times, where τ_*^{-1} is the total scattering rate, and $\tau_* \approx 0.01$ps.

The weak (anti)localization effect is a low temperature quantum interference effect which occurs in disordered systems where electrons can remain coherent over sufficiently long

distances [1]. Fig. 2.5 shows four scattering terms which contribute to this process. Fig. 2.5 (a) shows τ_φ, the dephasing rate due to inelastic scattering [13], which acts to control the maximum lengths of paths that can contribute to weak (anti)localization due to the need to maintain phase coherence. Fig. 2.5 (b) shows the three other main scattering terms [14]: τ_i, the elastic intervalley scattering rate which comes from atomically sharp scatterers and scattering from the edges of the device; τ_w, the elastic intravalley trigonal warping scattering term; and finally τ_z, elastic intravalley chirality breaking scattering term which comes from dislocations as well as other topological defects. There is a further tau, τ_* which was originally defined as $\tau_*^{-1} \equiv \tau_w^{-1} + \tau_z^{-1} + \tau_i^{-1}$ [13]. This definition is used in this thesis; however, it is worth pointing out that in the literature an alternate definition is often used, where $\tau_*^{-1} = \tau_w^{-1} + \tau_z^{-1}$. Care must therefore be taken when dealing with τ_*^{-1} to account for these different definitions.

Fig. 2.5 (a) displays two self-intersecting scattering paths. These two paths are identical except for the direction of travel around the loop. Classically, the existence of these two directions would not be a cause for concern. For specified start and end points, the probability of propagation is merely the sum of the squares of the amplitudes of the different paths, $P = |A_1|^2 + |A_2|^2$. However, in systems where the coherence of the samples is maintained, it is more appropriate to treat the carriers as quantum mechanical waves. In travelling around such scattering loops the carriers pick up a phase, and in general they acquire a different phase depending on the direction of travel around the loop. Depending on the phase difference, the two paths could interfere constructively or destructively, and hence the appropriate formula to calculate the propagation probability is: $P = |\psi_1 + \psi_2|^2 = |\psi_1|^2 + |\psi_2|^2 + 2Re(\psi_1\psi_2^*)$. The third term is the interference term, and whether the interference is positive or negative will depend on the sign of this term. Constructive interference between two such loops results in loops being more common than classically expected and hence the resistivity will increase. This is known

as weak localization. The converse, where destructive interference occurs, is known as weak antilocalization. This weak localization correction term has been shown to result mostly from interference between self-intersecting paths where the carrier can propagate either way around such a path. That these paths are necessarily of identical length is the reason that such paths are the primary origin of such interference. Therefore, in the absence of another source of phase shift, the wavefunctions of such paths will have an equal but opposite phase, and survive the disorder averaging. This is the reason why the weak localization effect is substantially greater in lower dimensional systems; since the lower dimensionality dramatically increases the incidence of self-intersecting paths [15]. Due to the need to maintain phase coherence for an interference effect to occur, τ_φ acts to control the maximum size of such loops, and thus control the magnitude of the weak (anti)localization effect.

Whether we are operating in a weak localization regime or a weak antilocalization regime depends on the phase the carriers pick up while traversing such a loop. Because of the existence of a Berry phase in monolayer graphene [12], the two trajectories are expected to gain a phase difference of π, leading to destructive interference, and hence to weak antilocalization [16]. However, in the presence of significant elastic intervalley scattering (τ_i), weak localization can be restored. The reason for this is that chirality is reversed between the two valleys [17]; thus trajectories involving intervalley scattering allow for zero phase difference between two self-intersecting paths, leading to constructive interference and hence weak localization.

The weak (anti)localization effect can be destroyed by increasing either the magnetic field or temperature to a sufficient value. Increased magnetic fields add a random relative phase to the carriers as they traverse curved paths, causing the interference effect to be averaged away [1]. Increased temperature has the effect of decreasing τ_φ, which reduces

the magnitude of both types of localization effect, Eq. (2.10). τ_i, and τ_* in contrast are found to be approximately independent of temperature [18].

This thesis has made use of the main result from McCann *et al.* [13] to produce fits of the resistivity as a function of magnetic field, B, to the measured weak (anti)localization:

$$\Delta\rho(B) = -\frac{e^2\rho^2}{\pi h}\left(F\left(\frac{\tau_B^{-1}}{\tau_\varphi^{-1}}\right) - F\left(\frac{\tau_B^{-1}}{\tau_\varphi^{-1}+2\tau_i^{-1}}\right) - 2F\left(\frac{\tau_B^{-1}}{\tau_\varphi^{-1}+\tau_*^{-1}}\right)\right), \quad (2.9)$$

where $F(z) = \ln z + \psi\left(\frac{1}{2}+\frac{1}{z}\right)$, ψ is the digamma function, $\tau_B^{-1} = \frac{4eDB}{\hbar}$, and D the diffusion coefficient $= \frac{1}{2}v_F^2\tau_{tr}$, where τ_{tr} is the transport time. At small magnetic fields, where $z \ll 1$, we can approximate $F(z) \approx \frac{z^2}{24}$. Using this we can simplify Eq. (2.9) for small fields as

$$\Delta\rho(B) = -\frac{e^2\rho^2}{24\pi h}\left(\frac{4eDB\tau_\varphi}{\hbar}\right)^2\left(1 - \frac{1}{\left(1+2\frac{\tau_\varphi}{\tau_i}\right)^2} - \frac{2}{\left(1+\frac{\tau_\varphi}{\tau_*}\right)^2}\right). \quad (2.10)$$

From this equation it is clear how variations in τ_φ control the magnitude of the weak (anti)localization. It is also clear how significant intervalley scattering, τ_i, is required to produce a positive resistivity correction, i.e. weak localization. In practice, significant intervalley scattering is found in most samples, and therefore weak localization is far more commonly found than weak antilocalization [19].

Fig. 2.5 (c) illustrates the shapes of weak (anti)localization curves for several realistic regimes of scattering times. For the case where τ_i, and τ_* are approximately equal or longer than τ_φ, the sample will be in a weak antilocalization regime. As described previously, significant τ_i is required for weak localization, with the relative strengths of τ_i, and τ_* acting to control the shape of the weak localization curve.

2.3 Anomalous half-integer quantum Hall effect

2.3.1 Classical Hall effect

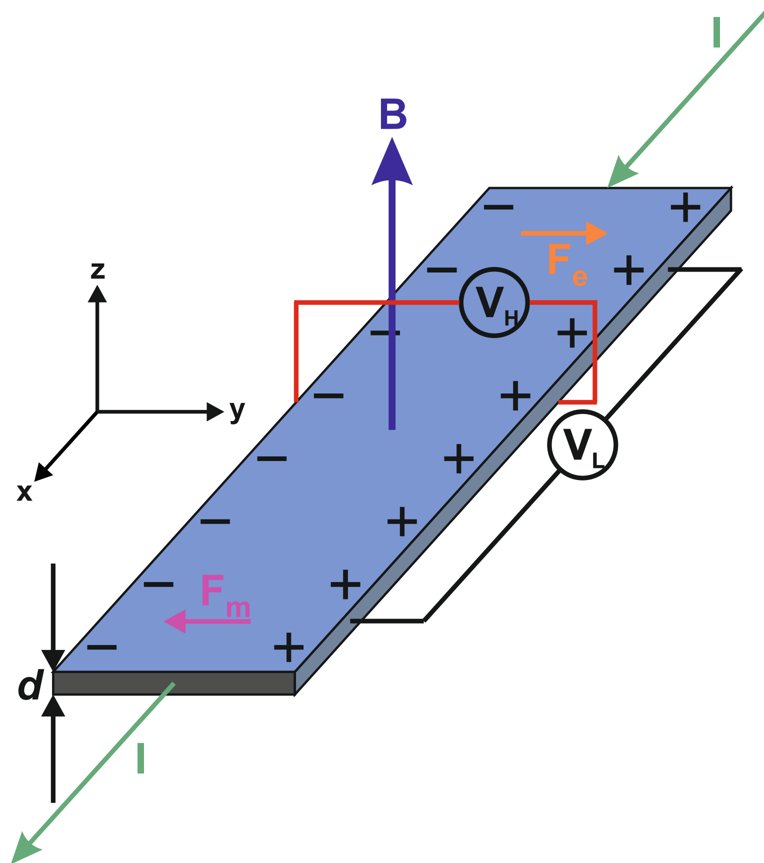

Figure 2.6: Figure showing the distribution of excess charges in a thin flat conductor, of thickness d, in the presence of magnetic field B, perpendicular to the applied current. The Lorentz force felt by the (negatively charged) carriers is shown, labelled F_m. The force of the electric field from the distribution of excess charges is shown, labelled F_e. Two voltmeters are shown which measure the Hall voltage, V_H, and the longitudinal voltage, V_L.

The classical Hall effect was discovered in 1879 by Edwin Hall [20]. An example setup for measuring the Hall effect is shown in Fig. 2.6. Whenever an electric current flows in the presence of a magnetic field, the charge carriers will experience a Lorentz force, F_m. This

changes the distribution of carriers within a conductor, causing parts of the conductor to develop excess positive and negative charge, represented in the figure by the +'s and -'s. This charge distribution generates an electric field which exerts a force F_e on the charge carriers. When a current is first applied, or its magnitude changed, the excess charges will accumulate until the electric field force reaches the same magnitude as the Lorentz force. In this state there is no net force on the charge carriers perpendicular to the overall current, and hence the conductor settles into a steady state. This electric field across the sample is known as the "Hall voltage", which is measured in the figure by voltmeter V_H. In a simple material with only one type of charge carrier this Hall voltage is given by

$$V_H = -\frac{IB}{ned}, \tag{2.11}$$

where n is the carrier density, and d is the thickness of the conductor. A related quantity, the Hall coefficient, R_H, can be defined by

$$R_H = \frac{E_y}{j_x B} = \frac{V_H d}{IB} = -\frac{1}{ne}, \tag{2.12}$$

where j is the current density. The Hall coefficient is a sample-dependent parameter which varies depending on the number and type of carriers present in the sample.

2.3.2 Landau levels

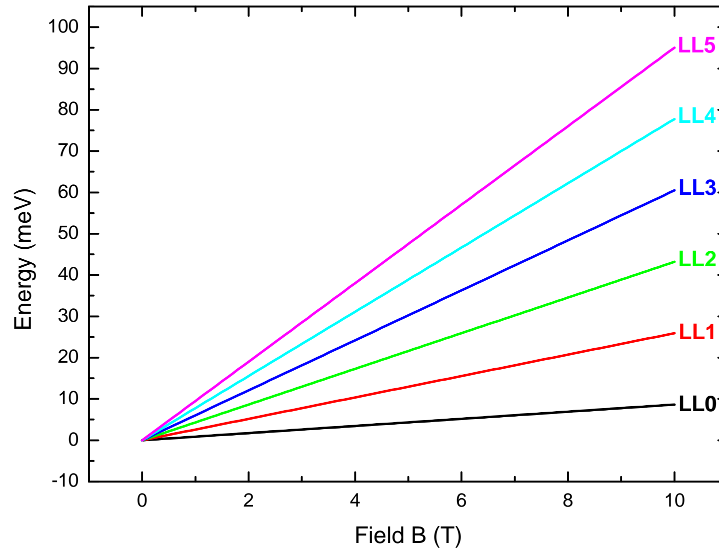

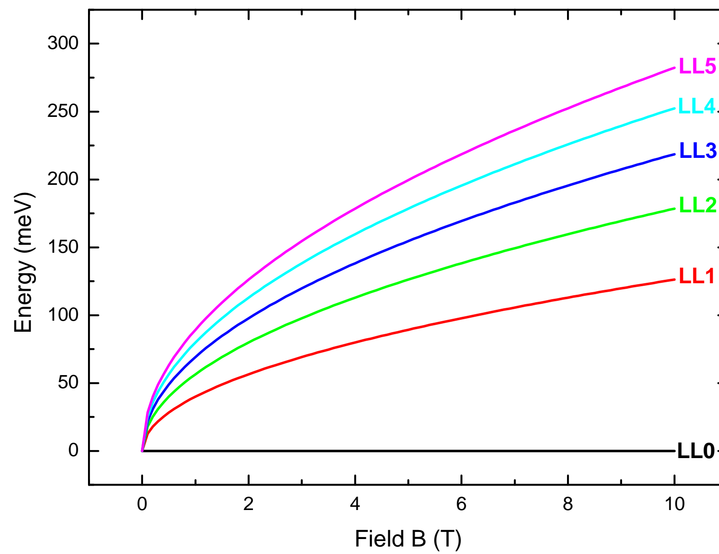

Figure 2.7: Landau level (LL) fan diagrams calculated for: (a) GaAs (a conventional two-dimensional system), and (b) monolayer graphene. Unusually, graphene's Landau levels scale as $\sqrt{B}$ instead of the usual linear in B behaviour. The Landau level spectrum for monolayer graphene is also unusual in that the spacing between the Landau levels is much larger than in conventional systems, particularly between LL0 and LL1, and in that LL0 is at exactly zero energy.

The quantum Hall effect is the quantum-mechanical version of the classical Hall effect. It is observed in systems with two-dimensional carriers, at temperatures low enough to preserve the quantum effect. Remarkably, in contrast to the classical Hall effect, the quantum Hall effect produces a Hall voltage which corresponds to a resistivity, which is a multiple (integer quantum Hall effect), or a simple fraction (fractional quantum Hall effect) of the von Klitzing constant, $R_K = \frac{h}{e^2} = 25813\ \Omega$.

To understand the quantum Hall effect the density of states in such systems must be studied. In three dimensions, applying a strong magnetic field causes the energy of the charge carriers to become completely quantized in the plane perpendicular to the magnetic field; this results in a one-dimensional energy density of states. In a two-dimensional system, however, the two-dimensionality has already removed one degree of freedom such that applying a magnetic field results in a density of states that is simply a series of discrete energy levels. The discrete energy levels in this series are known as Landau levels [5].

In conventional systems which exhibit the quantum Hall effect, such as Si/SiGe [21] or GaAs-AlGaAs heterojunctions [22], the series of energy levels is given by [5]

$$E_n = \left(n + \frac{1}{2}\right)\hbar\omega_c + E_j, \tag{2.13}$$

where n is the Landau level index, and E_j is the energy of the jth sub-band. A fan diagram of such Landau levels calculated for GaAs [23] is shown in Fig. 2.7 (a). The Landau levels in such systems scale linearly with field, and are equally spaced. Graphene, in contrast, has unusual Landau levels which are not governed by this formula. Graphene instead obeys the formula [24]

$$E_n = \text{sgn}(n) \text{ x } \sqrt{2e\hbar v_F^2|n|B}. \tag{2.14}$$

Such Landau levels are characteristic of the Dirac fermions which are the charge carriers in graphene near the Fermi level [25], section 2.1.4. A fan diagram illustrating the Landau levels in graphene is shown in Fig. 2.7 (b). It is immediately apparent that such Landau levels are no longer linear with B and instead have a $\sqrt{B}$ dependence. This has the important consequence that such levels are no longer evenly spaced. One further difference between the Landau levels in graphene and conventional systems, not apparent in the above equations or figure, is the number of states for each Landau level. In conventional systems such as GaAs there are $\frac{2eB}{h}$ states per Landau level. However, in graphene there are $\frac{4eB}{h}$ states per Landau level [26]. The reason for this is that conventional systems gain a degeneracy of two from spin. In addition to a two-fold degeneracy in spin, graphene also has a two-fold valley degeneracy, leading to an overall degeneracy of four. The degeneracy in graphene can be lifted at very high fields [24], though there is still some debate as to the order in which the degeneracy is lifted [27].

In practice, such Landau levels are not infinitely narrow as the above formulae would suggest; this is because of broadening from scattering, e.g. from imperfections in the surface layer or impurities. This scattering broadens the levels by $\delta E \approx \frac{\hbar}{\tau}$, where τ is the relaxation time between scattering events [5].

2.3.3 Integer quantum Hall effect

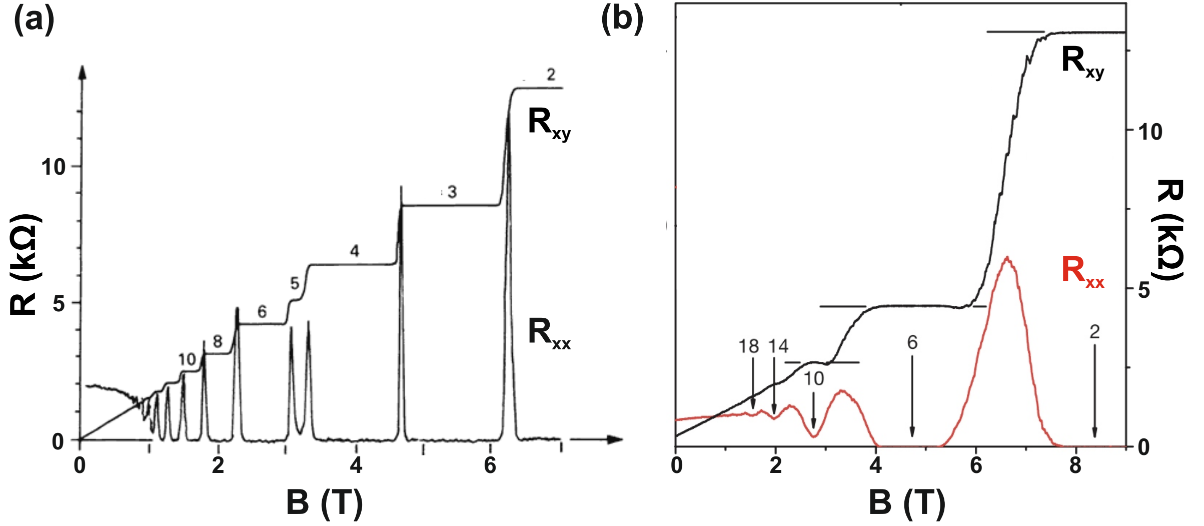

Figure 2.8: Magnetotransport traces for (a) a conventional system [28], and (b) a monolayer of graphene [29]. (a) It should be noted that the observed filling factors in the conventional system observe a 2n dependence at low fields, with additional odd filling factors observable at higher fields due to lifting of the spin degeneracy [30]. (b) In contrast in the monolayer graphene system, the filling factors observe a $4(n+\frac{1}{2})$ dependence, where the factor of four is due to the four-fold spin and valley degeneracy. The $+\frac{1}{2}$ results from considerations of the unusual zeroth Landau level [31]. Figure adapted from [28] & [29].

Fig. 2.8 shows the integer quantum Hall effect and the related Shubnikov-de Haas effect in a conventional two-dimensional system, (a), and in monolayer graphene, (b). The quantum Hall effect is measured across the sample (V_H in Fig. 2.6), and the Shubnikov-de Haas effect is measured longitudinally along the sample (V_L in Fig. 2.6). The measurement across the sample is customarily labelled ρ_{xx}, and the measurement along the sample is labelled as ρ_{xy}. This comes from the two-dimensional definition of conductivity as [5]

$$J_x = \sigma_{xx}E_x + \sigma_{xy}E_y, \tag{2.15}$$

$$J_y = -\sigma_{xy} E_x + \sigma_{xx} E_y, \tag{2.16}$$

where resistivity is defined in relation to these using

$$\rho_{xx} \equiv \frac{E_x}{J_x} = \frac{\sigma_{xx}}{\sigma_{xx}^2 + \sigma_{xy}^2}, \tag{2.17}$$

$$\rho_{xy} \equiv \frac{E_y}{J_x} = \frac{\sigma_{xy}}{\sigma_{xx}^2 + \sigma_{xy}^2}. \tag{2.18}$$

So how do the data presented in Fig. 2.8 correspond with the description of the Landau levels above? On application of a magnetic field, the spacing between the Landau levels increases with increasing field. For the quantum Hall effect to be apparent, the magnetic field has to be sufficient such that the spacing of the Landau levels is greater than the broadening from scattering. This is required so that the Landau levels are properly defined, and do not merge into each other [5]. It is also a requirement that the spacing is greater than $\sim k_B T$, so that the distribution of carriers is predominantly in one Landau level [5]. As the field increases, and the separations of the Landau levels increase, each Landau level in turn will pass through the Fermi energy [5].

When the Fermi energy is near a Landau level, the system operates in a regime of extended states. When the Fermi level is far away from any Landau level, the system operates in a regime of localized states. The presence of disorder causes the extended states to have a finite width in field; without such disorder the system would only operate in an extended state regime for an infinitesimal width of field around an alignment of Landau level and Fermi energy. In the localized states, the carriers in the bulk are stranded in isolated puddles with no conduction paths across the bulk of the sample

[5, 32]. There are however conducting states along the edge of the sample [32, 33]. In the localized regime $\sigma_{xx} = \rho_{xx} = 0$, and ρ_{xy} takes a quantized value. Each regime of localized states is labelled with a parameter known as the filling factor, ν, with $\rho_{xy} = \frac{R_k}{\nu}$. In the extended states conduction paths exist across the bulk of the sample, and hence σ_{xx} and ρ_{xx} are finite [5, 32].

Examining Fig. 2.8 (a) and Fig. 2.8 (b) closely, it is apparent that the conventional and graphene samples have a different sequence of filling factors. The gaps between successive filling factors depend on the degeneracy, which, as described above, is two for conventional two-dimensional systems and four for monolayer graphene [29]. It is clear, however, that this cannot be the complete picture, since we would expect the sequence of filling factors for graphene simply to be $4n$ (where n is an integer), instead of the observed $4(n + \frac{1}{2})$. This shift, which causes the anomalous quantum Hall effect in graphene, can be attributed to the zeroth Landau level in graphene. That level, as can be seen from Eq. (2.14) is at exactly zero energy, and unusually is populated by electron and hole states [29, 31].

2.3.4 Shubnikov-de Haas effect

The Shubnikov-de Haas effect is a magnetotransport process that causes oscillations in the longitudinal resistivity with magnetic field, ρ_{xx}. As with the quantum Hall effect, this process is related to the Landau levels [34]. At low fields, for approximately the regime where the separation of Landau levels is less than that from the broadening of the levels by scattering, the oscillations are sinusoidal and can be modelled by [35]

$$\frac{\Delta\rho}{\rho} = f(\omega_c\tau)\frac{\chi}{\sinh\chi}e^{-\frac{\pi}{\omega_c\tau_q}}, \tag{2.19}$$

where τ_q is the quantum lifetime, and

$$\chi = \frac{2\pi^2 k_B T_e}{\hbar\omega_c}. \tag{2.20}$$

Eq. (2.19) breaks down into two main components, with $f(\omega_c\tau)$ simply being a numerical coefficient. The first component is the temperature-dependent factor, $\frac{\chi}{\sinh\chi}$. This component can be used to calculate the carrier temperature, and can be fitted to calculate the Fermi velocity, from ω_c's dependence on the Fermi velocity. The second component of Eq. (2.19) is the field dependent term, $e^{-\frac{\pi}{\omega_c\tau_q}}$. This term is known as the Dingle term, and can be used to calculate the quantum lifetime, τ_q.

These two terms are each associated with damping of the Shubnikov-de Haas effect. The temperature-dependent term is associated with damping caused by an increase in temperature changing the carrier distribution between the Landau levels. The dingle term is associated with damping from broadening in the levels themselves from scattering.

Bibliography

[1] A. H. Castro Neto, F. Guinea, N. M. R. Peres, K. S. Novoselov, and A. K. Geim, Rev. Mod. Phys. **81**, 109 (2009).

[2] P. R. Wallace, Phys. Rev. **71**, 622 (1947).

[3] S. Reich, C. Thomsen, and J. Maultzsch, *Carbon Nanotubes: Basic Concepts and Physical Properties*, 1st ed. (John Wiley & Sons, 2004).

[4] K. D. Sattle, *Handbook of Nanophysics: Functional Nanomaterials*, 1st ed. (CRC Press, 2010).

[5] J. Singleton, *Band Theory and Electronic Properties of Solids*, 1st ed. (OUP Oxford, 2001).

[6] S. Reich, J. Maultzsch, C. Thomsen, and P. Ordejón, Phys. Rev. B **66**, 035412 (2002).

[7] P. Trevisanutto, C. Giorgetti, L. Reining, M. Ladisa, and V. Olevano, Phys. Rev. Lett. **101**, 226405 (2008).

[8] M. Soler, E. Artacho, J. D. Gale, A. Garc, J. Junquera, P. Ordej, and S.-P. Daniel, J. Phys. Condens. Matter **14**, 2745 (2002).

[9] R. Deacon, K.-C. Chuang, R. J. Nicholas, K. S. Novoselov, and A. K. Geim, Phys. Rev. B **76**, 081406 (2007).

[10] R. Saito, G. Dresselhaus, and M. S. Dresselhaus, *Physical Properties of Carbon Nanotubes*, 1st ed. (Imperial College Press, 1998).

[11] A. K. Geim and K. S. Novoselov, Nat. Mater. **6**, 183 (2007).

[12] K. S. Novoselov, A. K. Geim, S. V. Morozov, D. Jiang, M. I. Katsnelson, I. V. Grigorieva, S. V. Dubonos, and A. A. Firsov, Nature **438**, 197 (2005).

[13] E. McCann, K. Kechedzhi, V. I. Fal'ko, H. Suzuura, T. Ando, and B. L. Altshuler, Phys. Rev. Lett. **97**, 146805 (2006).

[14] F. Tikhonenko, D. Horsell, B. Wilkinson, R. Gorbachev, and A. Savchenko, Physica E **40**, 1364 (2008).

[15] S. Datta, *Electronic Transport in Mesoscopic Systems*, new ed. ed. (Cambridge University Press, 1997).

[16] D. W. Horsell, F. V. Tikhonenko, R. V. Gorbachev, and A. K. Savchenko, Phil. Trans. R. Soc. A **366**, 245 (2008).

[17] V. I. Fal'ko, K. Kechedzhi, E. McCann, B. Altshuler, H. Suzuura, and T. Ando, Solid State Commun. **143**, 33 (2007).

[18] D. K. Ki, D. Jeong, J. H. Choi, H. J. Lee, and K. S. Park, Phys. Rev. B **78**, 125409 (2008).

[19] F. V. Tikhonenko, A. A. Kozikov, A. K. Savchenko, and R. V. Gorbachev, Phys. Rev. Lett. **103**, 226801 (2009).

[20] E. H. Hall, Am. J. Math **2**, 287 (1879).

[21] G. Stöger, G. Brunthaler, G. Bauer, K. Ismail, B. S. Meyerson, J. Lutz, and F. Kuchar, Phys. Rev. B **49**, 10417 (1994).

[22] E. K. Sichel, M. L. Knowles, and H. H. Sample, J. Phys. C: Solid Stat Phys. **19**, 5695 (1986).

[23] Y. Ma, R. Fletcher, E. Zaremba, M. D'Iorio, C. T. Foxon, and J. J. Harris, Phys. Rev. B **43**, 9033 (1991).

[24] Y. Zhang, Z. Jiang, J. P. Small, M. S. Purewal, Y.-W. Tan, M. Fazlollahi, J. D. Chudow, J. A. Jaszczak, H. L. Stormer, and P. Kim, Phys. Rev. Lett. **96**, 136806 (2006).

[25] K. C. Chuang, A. M. R. Baker, and R. J. Nicholas, Phys. Rev. B **80**, 161410(R) (2009).

[26] D. A. Abanin, K. S. Novoselov, U. Zeitler, P. A. Lee, A. K. Geim, and L. S. Levitov, Phys. Rev. Lett. **98**, 196806 (2007).

[27] I. a. Luk'yanchuk and A. M. Bratkovsky, Phys. Rev. Lett. **100**, 176404 (2008).

[28] R. B. Laughlin, H. L. Störmer, and D. C. Tsui (Nobel Prize Press Release, 1998).

[29] Y. Zhang, Y.-W. Tan, H. L. Stormer, and P. Kim, Nature **438**, 201 (2005).

[30] M. M. Fogler and B. I. Shklovskii, Phys. Rev. B **52**, 17366 (1995).

[31] V. Gusynin and S. Sharapov, Phys. Rev. Lett. **95**, 146801 (2005).

[32] A. W. W. Ludwig, M. P. A. Fisher, R. Shankar, and G. Grinstein, Phys. Rev. B **50**, 7526 (1994).

[33] S. A. Trugman, Phys. Rev. B **27**, 7539 (1983).

[34] F. Duan and J. Guojin, *Introduction to Condensed Matter Physics: Volume 1*, 1st ed. (World Scientific Publishing Company, 2005).

[35] T. Ando, J. Phys. Soc. Japan **37**, 1233 (1974).

Chapter 3

Device Fabrication and Measurement Techniques

This chapter begins with a description of the most common graphene synthesis methods. It then proceeds to examine the typical Hall bar fabrication procedure and the main measurement apparatus used in this thesis.

3.1 Graphene synthesis

There are two broad approaches which can be taken in producing graphene [1]. The first approach comprises the top-down methods. These start with bulk materials which contain graphene layers such as highly oriented pyrolytic graphite (HOPG), or natural graphite, and, by selectively removing atoms or layers, e.g. by micro-mechanical exfoliation or sonication, arrive at (monolayer) graphene. The second approach comprises are the bottom-up methods. These include epitaxial growth on silicon carbide, and chemical vapour deposition (CVD) onto metal. These methods chemically build up graphene crystals piece by piece. Currently the three most common graphene fabrication methods from both approaches are micro-mechanical exfoliation, epitaxial growth from silicon carbide, and CVD onto copper. Samples from all three of these methods are investigated in this thesis.

3.1.1 Micro-mechanical exfoliation

Micro-mechanical exfoliation was the original method used by Andre Geim and Konstantin Novoselov in 2004 to discover graphene [2]. The process, colloquially known as the "sticky tape" method is, at least in hindsight, astonishingly simple. The basic process involves taking a piece of graphite, and two pieces of sellotape. One piece of sellotape is pressed onto the graphite and then peeled off. This peels a thin flake of graphite away with the tape. This thin flake of graphite on tape can then be pressed onto the other piece of tape. When these two pieces of tape are separated they leave a thinner flake of graphite on each piece of tape. The process is repeated until we are left with multiple thin flakes, including a few which are monolayer. Given the simplicity of the fabrication process, it appears surprising that graphene was not discovered earlier;

there are, however, two main reasons which explain this. The first is that graphene was presumed to be unstable in its free-standing standing form, and there were apparently convincing theoretical predictions that thermal fluctuations in 2D crystals should destroy any long range order in such crystals rendering them unstable [3, 4]. Explanations have subsequently been proposed for this stability problem which suggest that the 2D graphene crystals undulate in the third dimension and it is these "corrugations" that stabilize the graphene crystals [5]. The second reason is the extreme difficulty of finding monolayer graphene flakes after they have been produced. This problem is compounded in that the unoptimized micro-mechanical cleavage method has a very low yield of monolayer flakes, and that those produced are typically very small. The ingenious way that Geim and Novoselov overcame this problem was to deposit their flakes onto a silicon substrate with a thin, 300nm silicon dioxide layer [2]. This produces an interference-like effect when graphene is placed on the substrate surface, producing a wavelength shift of the SiO_2 colour, allowing quick accurate identification of mono and bi-layer flakes through an optical microscope [6] (Fig. 3.1). To date (2012), this method produces the highest quality graphene with mobilities in excess of 200,000 $cm^2\ V^{-1}\ s^{-1}$ in suspended graphene (suspended on a scaffold in air or vacuum above the substrate) [7]. The major disadvantage of this method is that the flake sizes are in general limited to a few tens of μm square [8], and it is hard to see how this process could be scaled up in a commercially viable manner to wafer scale. These issues with the micromechanical cleavage method have been, and continue to be, a major driver of the extensive research which has gone into graphene synthesis.

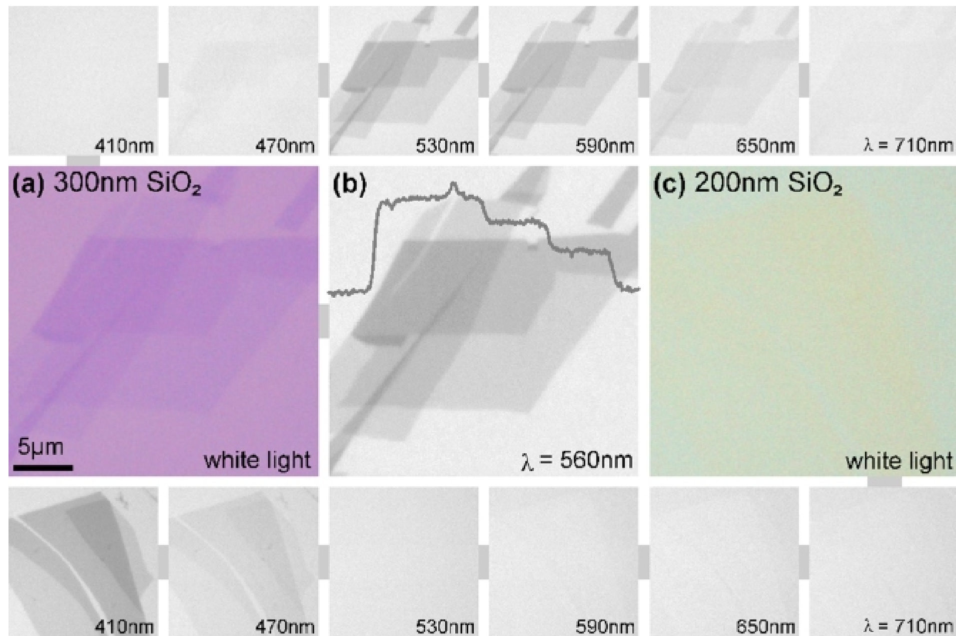

Figure 3.1: Series of microscope images demonstrating the advantage of using a silicon wafer with a 300nm layer of SiO_2. (a) Shows mono, bi and multi-layer graphene illuminated under white light on a 300nm layer, and (c) with a 200nm layer. The graphene layers are far clearer under the 300nm condition. The small images on the top line, and (b) show the contrast attained using 300nm SiO_2 under different illumination wavelengths. The images in the bottom line show the contrast attained using 200nm SiO_2 under different illumination wavelengths. Figure adapted from Blake *et al.* [6].

3.1.2 Epitaxial growth on SiC

A second approach to fabricating graphene is epitaxial growth of graphene on silicon carbide. A simplified version of the process involves heating the silicon carbide to a temperature in excess of 1200 °C in a vacuum, or preferably in argon [9]. The growth can be derived either from the silicon or carbon-terminated face of the SiC. In general, the silicon-terminated face produces small domain sizes which are predominantly monolayer [9]. In contrast, the carbon-terminated face produces larger area domains which are typically several layers thick [9]. There is some discussion in the literature, however, that these layers might act as nearly independent graphene monolayers due to the rotational disorder between the layers [10, 11]. In either growth regime, the silicon carbide

thermally decomposes with the silicon atoms evaporating from the surface, producing an excess of carbon in the surface layers [1]. These excess carbon atoms create bonds between each other, forming graphene. So far mobilities as high as 25,000 $cm^2\ V^{-1}\ s^{-1}$ have been attained [12]. While these are not as high as those attained for exfoliated graphene, they are comparable to those attained in graphene derived by CVD onto metal [13]. The big advantage of epitaxial growth of graphene on silicon carbide is that it is grown straight onto an insulating substrate which renders the graphene immediately suitable for device applications [1]. Currently though, it has the large disadvantage that the high-quality SiC wafers needed for the process are expensive [14].

3.1.3 Chemical vapour deposition

The third main method of fabricating graphene is CVD growth of graphene onto a metal substrate. The most common metal currently used is copper [1], though other metals such as nickel [1] and ruthenium [15] have also been used. Copper has so far been found to be the best metal for CVD growth of graphene. This is due to the low solubility of carbon in copper [15], which causes the growth process of graphene to be self-limiting when the growth gases are at low pressures [16]. A typical process [16] involves raising the temperature of a 25 μm thin film of copper to 1000 °C in a H_2 environment. This causes the grain size in the metal to enlarge which produces better quality graphene [16]. The temperature is then held constant while a mixture of CH_4 and H_2 is passed through the growth chamber. This is the stage when the growth of graphene occurs. Finally, the temperature is rapidly dropped back to room temperature in H_2 gas. Encouragingly, this process is readily amenable to reel-to-reel production, allows easy transference of the graphene to other substrates, including flexible polymers (Fig. 3.2), and has the potential to become quite inexpensive. At present, carrier mobilities attained in CVD

graphene are around 37,000 cm^2 V^{-1} s^{-1} [13].

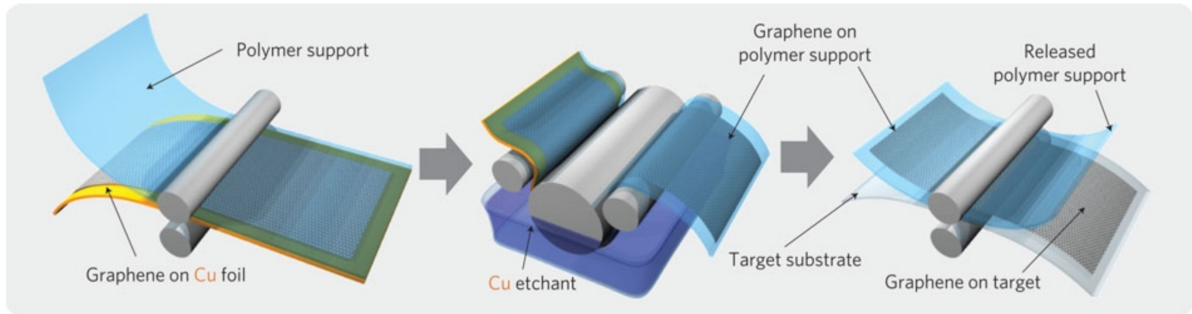

Figure 3.2: Schematic showing part of the reel-to-reel production method as described in Bae *et al.* [17]. Figure shows the procedure for transfering graphene grown by chemical vapour deposition on copper onto a target substrate in a continuous roll to roll process. Figure adapted from [17].

3.2 Device fabrication

This section describes the fabrication process for one of our typical exfoliated graphene Hall bars. I have personally carried out every one of the steps presented in this section, though in the interest of expediency for the majority of samples the workload was divided amongst myself and two other members of the group.

A Hall bar is simply a geometric arrangement of contacts designed for measuring the Hall effect (Sec. 2.3). An example Hall bar can be seen in Fig. 3.10 (b). The first step is to produce the graphene using the “sticky tape” process as described in sec. 3.1.1. The back-and-forth process between the two pieces of tape is carried out until one piece of tape is covered by a thin mat of graphene and graphite flakes (Fig. 3.3).

Figure 3.3: Photograph showing the blue Nitto tape commonly used for micro-mechanical exfoliation. Nitto tape is used here, as in the semiconductor industry, since it leaves nearly no residue after removal. In the photograph only the large graphite flakes are visible, coverage of thinner flakes is typically far more complete.

The next step is to transfer these flakes onto a suitable substrate. A bulk silicon wafer with a 300nm silicon dioxide thin film layer is used as the substrate. As described earlier in Sec. 3.1.1, the 300 nm silicon dioxide layer is there to exploit the interference-like effect [6], as well as providing an insulating dielectric layer. Before the graphene is transferred to the wafer, the latter is subjected to oxygen plasma in a plasma etcher for 60 seconds. This helps clean the surface, especially from carbon debris, and promotes adhesion between the graphene layers and the substrate, which is critical to producing large area (> 10 x $10\ \mu m^2$) flakes reliably. Once the wafer has been cleaned, the tape is pressed down onto the silicon dioxide, and pressure is applied evenly on the back surface, for example with a rubber. An even application of pressure is necessary to obtain large area flakes. Subsequent to the transfer, the wafer is briefly examined under a microscope to confirm there is sufficient coverage of flakes to give a reasonable chance of finding a large monolayer graphene flake.

3.2.1 Electron beam lithography system

In order to contact and shape graphene flakes we use electron beam (e-beam) lithography. An e-beam lithography system is a machine which can accurately steer a tight beam of electrons over a surface, providing controlled doses of electrons to each point in a predetermined pattern. The simplest e-beam systems are scanning electron microscopes (SEMs) which have been converted such that their scan coils can be digitally driven in steps [18]. Our e-beam is a dedicated JEOL JBX-5500ZC e-beam system. Such a dedicated system has several advantages over a converted SEM [18]. The first is that a dedicated system has a much higher beam current, typically 100 times larger (5nA vs. 50pA), than a converted SEM [18]. The second is that coil settling times are much faster on a dedicated system, typically 10 μs compared with 1 ms for a converted system [18]. These two advantages combine to leave dedicated systems much faster than converted ones, and hence a dedicated system allows for large areas to be written far faster. This speed allows us to conduct all of our lithographic steps using our e-beam system without the need to resort to photolithography for some stages, which is normally required when using a converted system. Another advantage is that much higher resolutions can be obtained with a dedicated system; around 10nm for our machine, compared to around 100nm for a converted system. This resolution is also much higher than the current industry state of the art silicon microprocessor production technology which has feature sizes of 22nm [19]. This higher resolution of a dedicated system is obtained by the use of better "optics", higher voltages, and beam stability [18]. A further advantage of a dedicated system is that the field of view, and hence the area which can be written without stitching, is much larger than in converted SEM systems. This problem in converted systems can be somewhat overcome by using a piezo-stage; however, this adds to the cost and is problematic due to the distortions at the edge of

the field in SEM systems [18].

3.2.2 First lithographic stage

To produce a typical Hall bar it is necessary to undertake multiple lithographic stages. In this chapter the first stage is described in great detail, and subsequent ones with reference to the first and therefore more briefly. The purpose of the first lithographic stage is to produce the bond pads and alignment marks. The purpose of the second stage is to write the contacting tracks from the bond pads, stopping just a short distance away from the graphene flake. The third stage mesa-etches the graphene flake into the desired Hall bar shape. And finally the fourth lithographic stage produces the final contacting tracks, connecting the graphene Hall bar to the previous partial contacting tracks.

3.2.3 Resists

In order to carry out the e-beam lithography the chip must first be coated in resist. A resist is an electron-sensitive (or in the case of photolithography, light-sensitive) polymer or polymer precursor dissolved in a solvent [20]. A resist can be either positive or negative in type. A positive resist is one where, after exposure, the exposed regions dramatically increase their solubility in a particular developer. A negative resist is the opposite of this, in that the exposed regions become less soluble to the developer. Typically this change in solubility is achieved by creating or destroying crosslinking/polymerization in the polymer, where the increased crosslinking/polymerization would normally decrease the solubility [20]. The purpose of the resist is to capture an image of the desired exposure pattern, and allow this image to be converted into a mask by using a developer.

The resist is normally applied by spin-coating, using a spin-coater. A spin-coater is a machine designed to spin a chip, or wafer, at high speeds on a preprogrammed speed-time path. Such a machine typically holds the chip/wafer on the end of a spinning disc using a vacuum. More advanced systems can also maintain a specified temperature.

As stated above, the purpose of the first lithographic stage is to produce the bond-pads, which are large conducting pads for connecting the chip to the measurement apparatus, and alignment marks, which are used for aligning further lithographic stages to this first one. The alignment between stages is critical to ensure correct fabrication of the chip. For the first stage a positive bilayer resist is used. We choose to use a positive resist for this stage since we wish a large majority of the chip to remain masked, and hence the exposure is far quicker when using a positive resist. The first resist layer is 8% PMMA 495 (polymethyl methacrylate) dissolved in anisole. The second resist layer is 8% PMMA 950, also dissolved in anisole. The number following the PMMA, in each, refers to the molecular weight where 495 stands for 495,000 u, and 950 stands for 950,000 u. We use a bilayer configuration of resists to allow for more successful lift-off, which is explained in greater detail in sec. 3.2.6. The PMMA 495 layer is applied to the chip using a spin coating process at 1000 RPM for 60 seconds. The resist is subsequently baked at 180 °C for 60 seconds to remove the excess solvent. Due to the increased viscosity from the higher molecular weight, the PMMA 950 layer must be spin coated at the much higher spin-speed of 5000 RPM for 60 seconds. This second layer is baked as before at 180 °C for 60 seconds. Once the resists are successfully applied the chip is ready for the exposure step. In order for the e-beam machine to produce the desired exposure pattern, it is necessary to define an electronic pattern from which it may work. This pattern is produced using AutoCAD, which in addition to allowing the researcher to define where the pattern should be written, also allows the researcher to select the doses applied when writing this pattern. A dose is measured as coulombs per cm^{-2}. We

use a dose of 600 μC cm^{-2} for features larger than 10 x 10 μm. For the smaller features we must use greater doses, reaching 900 μC cm^{-2} for the smallest features. An example pattern can be see in Fig. 3.4 below.

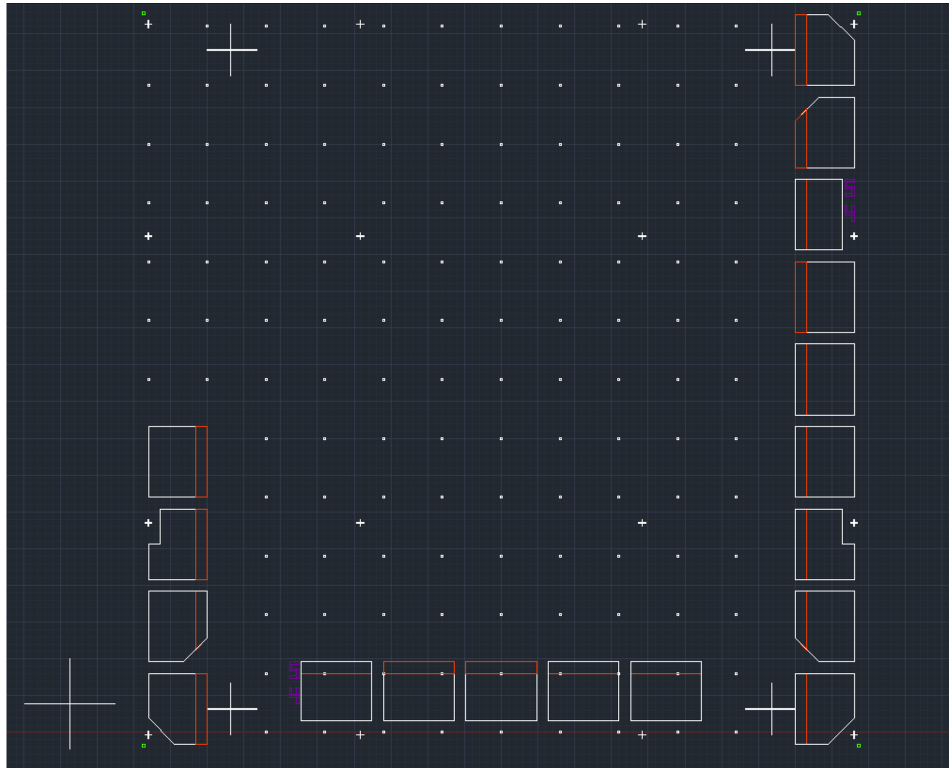

Figure 3.4: An example AutoCAD file from the first lithographic stage. Bondpads and alignment marks (dots and crosses) are clearly visible. Additionally small numbers shown in purple are visible, which give the code number of the current chip. The total size of the chip is 4 x 4 mm.

3.2.4 Development

The next step in the lithographic process is to develop the exposed resist on the chip. The development stage partially removes resist from all parts of the chip, but removes resist quicker from regions of higher solubility i.e. the exposed regions using positive resists, and the unexposed regions using negative resists. Thus by carefully controlling

the exposure time and temperature, it is possible to ensure that the resist is fully removed from the desired regions, while leaving sufficient resist across the rest of the chip. When using the bilayer resist, the developer preferentially removes the lower of the two layers of resist. This happens since the lower layer, due to its molecular weight, has a larger solubility than the top layer. For the first lithography step, the chip is developed in a 3 to 1 mixture of MIBK (methyl isobutyl ketone) to IPA (isopropyl alcohol). The development procedure is to immerse the chip in the development mixture for 60 seconds, at room temperature. In most other development procedures, the sample is immersed in developer within a sonic bath, for less time, while sonicating (subjecting the sample to very loud ultrasound). Unfortunately this is not an option when making graphene devices, since graphene has very weak adhesion to the SiO_2 substrate, and any sonication is sufficient to cause the graphene to lift-off from the substrate, ruining the device. After development, we are left with a mask in the desired pattern, leaving some areas of the chip completely exposed, and others remaining protected by a thin layer of the PMMA.

3.2.5 Metal evaporation

Once we have the chip correctly masked, the next step is to use a metal evaporator to evaporate a thin layer of metal on to the chip. The basic principle of such a machine is that a source material, typically a metal, is evaporated in a vacuum such that the evaporated atoms travel ballistically, i.e. without any scattering events, to the target chip held some distance away. The distance between the source and sample is typically ≥ 50 cm, and hence a very good vacuum is required to allow for the vast majority of atoms to be able to travel this distance without scattering. To achieve this, the vacuum has to be of the order of $\leq$ a few 10^{-4} Pa. The reason for placing the source some

distance away from the sample is to ensure that evaporated atoms arriving at different points on the sample arrive nearly parallel to each other. If the atoms do not arrive parallel to each other, the result can be a shadowing effect of the evaporated metal deposited on the substrate, reducing the evaporated metal's fidelity to the mask, and potentially making the lift-off step (Sec. 3.2.6) far harder. The energy required to evaporate the source material in our evaporator comes from Joule heating. The most common alternate method is to use a high-voltage electron beam to heat the source. There are several slightly different methods of evaporating the source material using Joule heating. The most common method used for this thesis was to place a small quantity of the desired evaporation material in a "boat". This boat is made from a material with a very high melting point, most commonly molybdenum (2890 K [21]), tantalum (3269 K [21]) or tungsten (3680 K [21]). Unfortunately, despite having the highest melting point, tungsten can not be used for all materials since it readily alloys with some materials at high temperatures [22]. The "boat" can simply be thought of as a thin strip of metal with a small cavity pressed out at its centre. Into this cavity the target evaporation material is placed, and the boat is placed between two electrical contacts inside the evaporator such that a very large current can be passed through it. As the boat heats up, the source material melts into a pool contained by the cavity, and evaporates from here, travelling ballistically to the sample. The amount of the source material being deposited on the chip is measured by a crystal adjacent to the chip which correlates between the deviation of the resonant frequency of the crystal and the thickness of metal deposited on its surface.

It is preferable in the first lithographic stage to use a fairly thick layer of gold. This is desirable both for the bondpads and the alignment marks: for the bondpads, in order to have a low resistivity, and to make bonding easier (Sec. 3.2.9); and for the alignment marks, to have high visibility under an optical microscope. Unfortunately, gold has very

poor adhesion to SiO_2 [23], and so it is necessary first to evaporate a thin adhesion layer. In this case, 15 nm of chrome is used as the adhesion layer, followed by 250 nm of gold. The thickness of the gold is always a compromise between the ease of liftoff (Sec. 3.2.6), which favours thin gold layers, and ease of bonding (Sec. 3.2.9) / minimizing resistance to the sample, which favours thick gold layers. After evaporation, the sample is allowed to cool in order to prevent unwanted oxidation when air is readmitted; once cool, the vacuum is vented and the sample removed.

3.2.6 Lift-off

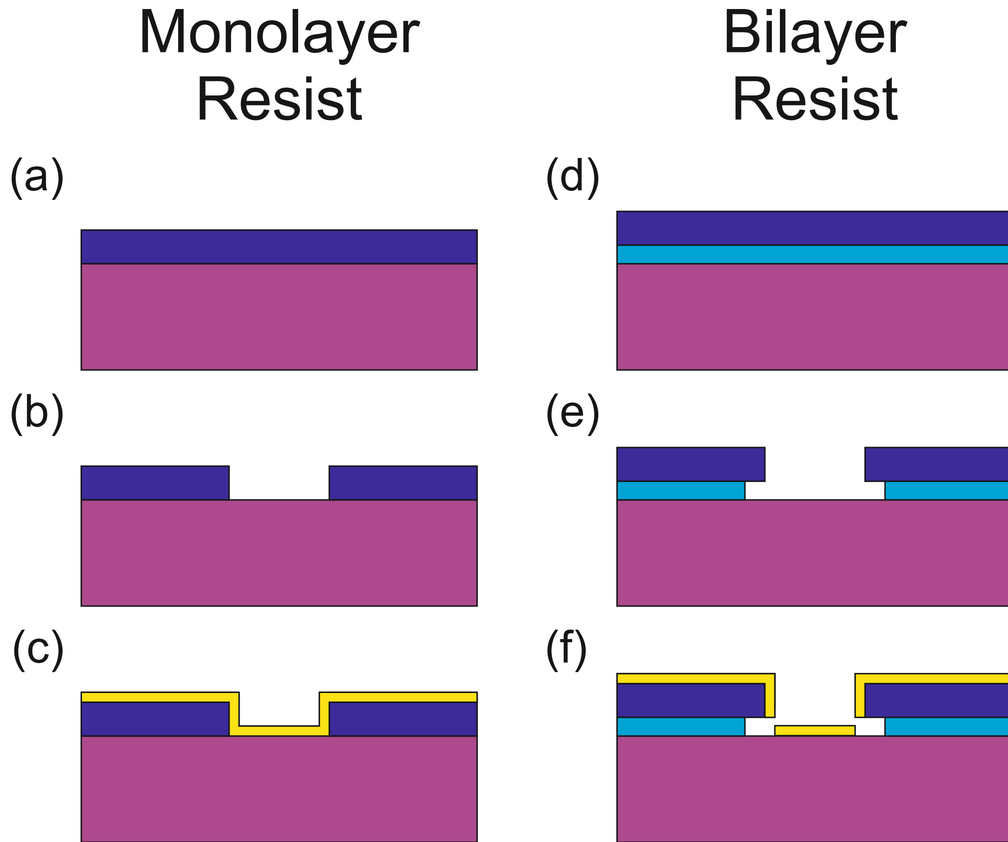

Figure 3.5: Diagram showing the advantage of using bilayer resists. (a) to (c) show the monolayer resist condition, where the lowest layer, shown in purple, is the substrate, the next layer up, in dark blue, is the resist, and in (c) the thin yellow layer is the evaporated metal. (a) shows the chip, after spin-coating and baking. (b) shows the chip after exposure and development. (c) shows the chip after metal evaporation. Even using an evaporated metal layer much thinner than the resist, (c) shows there is a risk that the metal on top of the resist, and that directly on top of the substrate will connect, which greatly interferes with lift-off. (d) to (f) show the bilayer resist condition, where the lowest layer, shown in purple, is the substrate, the next layer up, in light blue, is the first layer of resist, the second layer of resist is shown in dark blue, and in (f) the thin yellow layer is the evaporated metal. (d) shows the chip, after spin-coating and baking. (e) shows the chip after exposure and development. (f) shows the chip after metal evaporation. Note that in the bilayer resist condition, the metal on top of the resist, and that directly on top of the substrate, are not connected, which greatly improves the chances of successful lift-off.

The final step in the first lithography stage is the procedure known as lift-off. Following the evaporation, there is a thin metal film across the entire surface of the chip. However, the thickness of the resist and evaporated metal was carefully chosen such that metal evaporated directly onto the chip, was not usually connected to the metal evaporated on top of the remaining resist. To ensure that the metal is not connected between the two levels a bilayer resist was used as described in (Sec. 3.2.3). As shown in Fig. 3.5 (a) to (c), in the absence of a bilayer resist there is a risk of metalization around the cliff between the high and low regions of the chip, even when the thickness of the metal film is far thinner than that of the resist. The bilayer as shown in Fig. 3.5 (d) to (f) solves the problem by ensuring that even if there is metalization along the edge of the resist it avoids a connection being formed between the metal on the resist and the metal on the chip.

The lift-off procedure used for the first lithographic stage is to soak the sample in NMP (1-methyl-2-pyrrolidone) for 30 minutes at 100 °C. After the 30 minutes a pipette is taken, and the solution is rapidly sucked in and out of the pipette to agitate the solution and cause the undesired metal, which was previously resting on the resist, to be removed.

3.2.7 Flake discovery and positioning

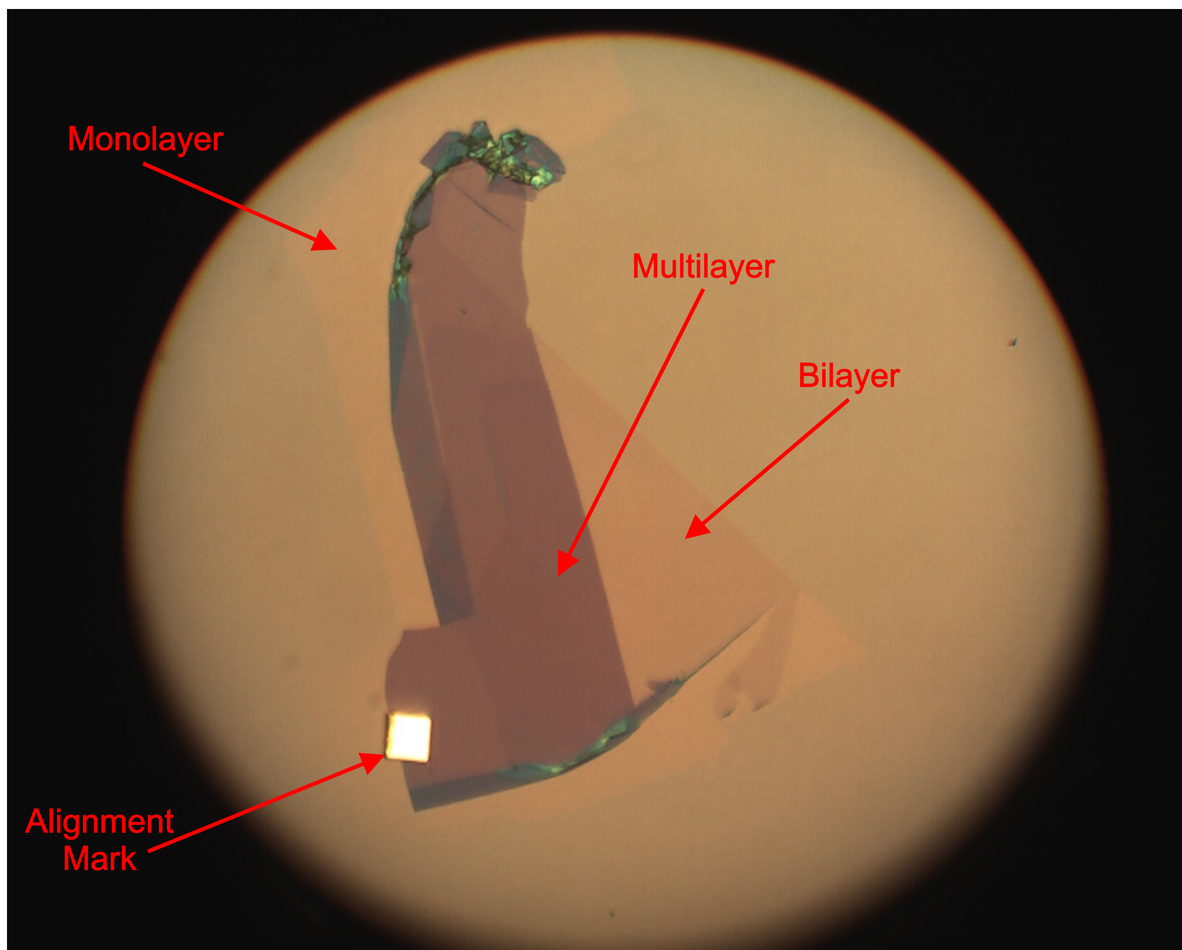

Figure 3.6: An example of one of the flakes found in the course of this investigation. Visible on the figure is one of our alignment marks shown next to graphene layers of varying thicknesses. Monolayer, bilayer, and multilayer regions are labelled with the monolayer region just visible, appearing as a very slight colour and opacity change from that of the substrate.

Given that the chip now has alignment marks, it is possible to identify accurately the position of any flakes on the chip. The chip is placed under a microscope equipped with a camera. The surface of the chip is systematically scanned, the best monolayer flakes identified, and positions noted. The thickness can easily be determined by observing the

opacity and wavelength shift with thickness (Fig. 3.6), using the technique described by Blake *et al.* [6]. This thickness determination can be confirmed from Raman spectroscopy [24], or from the presence of the “half-integer” anomalous quantum Hall effect (Sec. 2.3). Photographs are taken of the target flakes at varying levels of magnification which allow positioning relative to the original AutoCAD design as described in the next section.

3.2.8 Subsequent lithographic stages

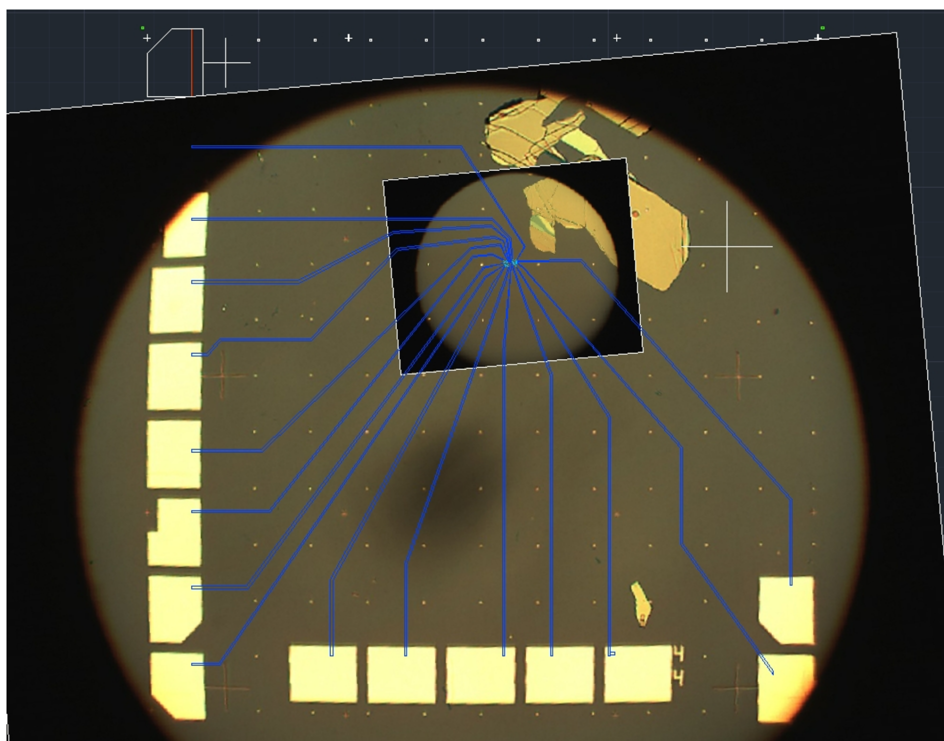

Figure 3.7: AutoCAD file for the second lithographic stage (tracks from the bondpads to near the graphene flake). Photographs from after the first lithographic stage are carefully superimposed on the original AutoCAD file. Using these photographs, tracks are defined relative to the discovered position of the flake. Such tracks are superimposed in blue on the figure.

Subsequent lithographic stages are reasonably similar to this first stage, with a few key differences. In the second lithographic stage, conducting tracks are written from the bondpads to close to, but not touching, the graphene flake. As shown in Fig. 3.7 a new AutoCAD file has to be designed to account for the previously unknown position of the flake or flakes. Exactly the same resist, development, and evaporation stages are used for this lithographic stage. The main difference in procedure between the first and second lithographic stage is during the exposure step, since the exposure pattern now needs to be aligned to the previously lithographed one. This is done using three of the alignment mark crosses in an "L" shape, which allows us accurately to define the position, scale, and orientation of the sample relative to the previous exposure. Any of these three can change slightly from exposure to exposure, since the position of the chip inside the e-beam chip holder will always be slightly different every time the chip is removed and replaced, as required for the processing steps.

The third lithographic stage is to mesa-etch our graphene flake into a Hall bar shape. For this stage we use a negative resist since we wish to mask a Hall bar shape on top of the graphene, and leave the entire rest of the chip exposed. To conduct this procedure using a positive resist would take on the order of a day of writing time using our e-beam system. The negative resist used is ma-N 1407. Before spinning the ma-N onto the chip a primer, HMDS (hexamethyldisilazane), is spin coated onto the chip for 45 seconds at 4000 RPM. The purpose of this is to promote adhesion between the ma-N and SiO_2 which could otherwise be weak. The ma-N is spin coated onto the chip at 5000 RPM for 60 seconds. The chip is then baked at 100 °C for 60 seconds. Since this lithographic step is used to mesa-etch the graphene and not to evaporate metal onto the chip there is no need to use a bilayer process. We then need to produce yet another AutoCAD file, this time simply with the shape of the Hall bar, and correctly align it to do the exposure. For this resist a different developer is needed, known as ma-D 533/S. As before, the sample

is immersed in the developer at room temperature, this time for 25 seconds. In order to shape the graphene the chip is placed in the plasma etcher in an oxygen plasma for 60 seconds. Using oxygen plasma quickly removes unwanted graphene, since it can readily convert carbon to carbon monoxide or carbon dioxide, while leaving the graphene under the ma-N polymer protected, and not attacking the metallic tracks or bondpads.

The fourth and final lithographic stage is to produce the final tracks to the device. The reason for splitting up the production of the tracks into two lithographic stages is that using an adhesive metal layer (the chrome in the first stage (Sec. 3.2.5)) between the gold and graphene can dramatically effect the contact resistance [25]. In preliminary work we discovered our contact resistance was greatly decreased by using only gold for the final contacting to the graphene device. Gold-only tracks, however, stick very poorly and so cannot be used over distances greater than around 10 μm. Otherwise this final step is exactly the same as the first two, merely omitting the chrome deposition stage.

3.2.9 Ball bonding

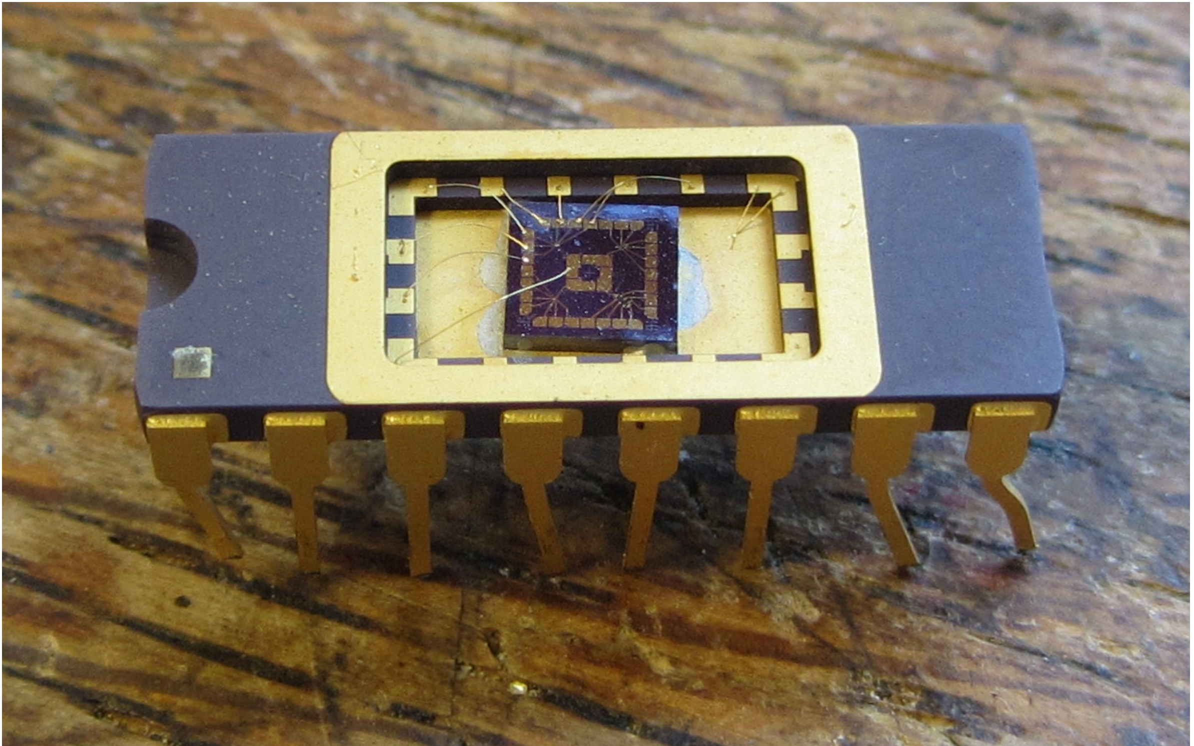

Figure 3.8: Photograph showing a fully fabricated chip inside a chip carrier. The chip carrier is a leaded ceramic chip carrier with gold contacts. The chip carrier is a standard dual in-line package (DIP), around 2cm in length. Ball bonded 25 μm gold bonds can be seen running from the chip carrier's bondpads to our chip's bondpads.

In order to measure the device it is necessary to connect the chip to the measurement apparatus. The first step is to "glue" down the chip to a ceramic chip carrier as shown in Fig. 3.8. We use ceramic chip carriers to minimize the distortion of the magnetic field from the chip carrier when both are placed inside a magnet. The chip is glued down to the carrier using silver DAG, which ensures an electrical connection to the silicon bulk of the chip, allowing backgating of the device. Gold wire interconnections are formed between the gold bondpads on the chip and carrier using a ball bonder.

A ball bonder can loosely be thought of as similar in operation to a sewing machine.

The chip carrier is securely clamped to a heater stage. Above this, 25 μm gold thread is passed through a disposable hollow needle-like device called a capillary, with the thread formed into a ball just beyond the capillary. The heater stage is normally mechanically connected to a mouse, very similar to that used with a computer, which allows the user accurately to position the bondpads under the capillary to form the bonds. Above the stage there is usually also a microscope to assist in this process. The heater stage heats the chip carrier, and hence bondpads, to 120 °C. When the user triggers the first bond, the capillary lowers until it is in contact with the bondpad. Once it is in contact, it triggers an ultrasonic pulse, and this, combined with the heated bondpads, is sufficient to melt the gold thread into the bondpad. The user then repositions the capillary to the desired site for the second bond. Again, after the bonding process is triggered, an ultrasonic pulse is provided by the capillary to melt the gold into the bondpad. However, in addition, this time the capillary pushes down in a manner which cuts the gold thread away from the capillary, leaving a bond between the two bonding locations. Finally a spark under the capillary is triggered, melting the tip of the gold thread to form a new ball, and this leaving it ready for the next bond.

A further consideration when using the ball bonder is its potential to punch a hole through the oxide layer of the substrate, rendering backgating impossible. To avoid damage to the oxide layer extreme care must be taken to minimize the heating, ultrasonic power, and applied force while still being able to bond successfully. Problems with the optimization of this stage where in large part responsible for the relatively minimal use of backgating in this thesis.

3.3 Measurement apparatus

Figure 3.9: Photograph of the 21T superconducting Oxford Instruments Magnet, the primary piece of equipment used in this investigation.

This section contains a brief overview of the primary measurement equipment used for the work presented in this thesis. Shown in Fig. 3.9 is our primary measurement apparatus, a 21T Oxford Instruments superconducting magnet. This system has two layers of cryogenics, an outer liquid nitrogen jacket, and an inner liquid helium 4 space.

The magnet is immersed in helium 4, and the temperature of the sample space can be controlled from 1.4K up to ∼310K by controlling the flow of helium into the sample space, and the current of a heater inside the sample space. It is possible to reduce the sample space temperature to below the boiling point of helium by using evaporative cooling. The evaporative cooling comes from pumping on the sample space with a vacuum pump. The chip carrier is attached to a long thin insert. This magnet is a top-loading design, and hence the insert is lowered into the magnet from the room above. The insert is adjusted such that when it comes to rest in the magnet, the sample is held in the exact magnetic field centre to ensure magnetic field uniformity across the chip.

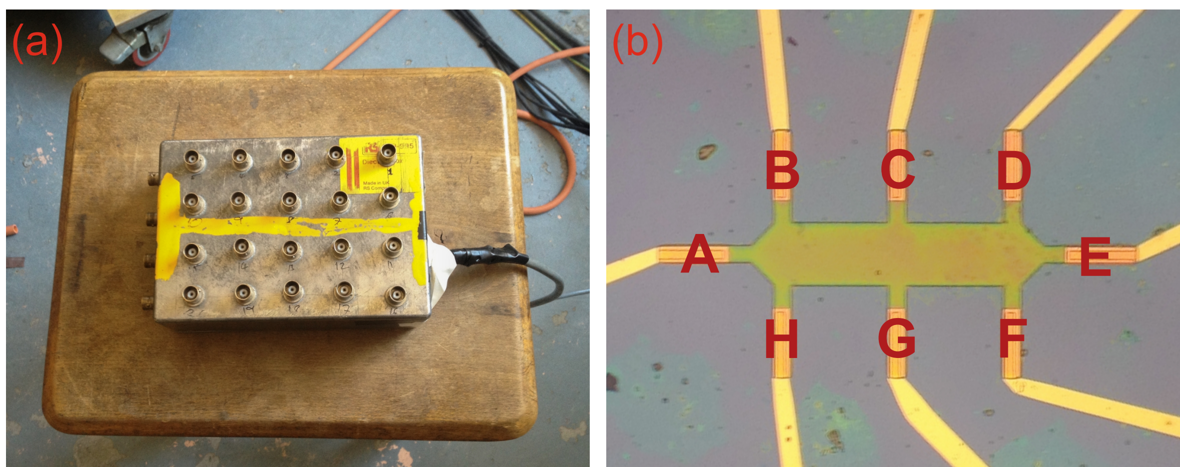

Figure 3.10: (a) the BNC box used in this research which connects the insert to the measurement DMMs. (b) shows an example of one of our finished Hall bars with contacts labelled A through H.

Through the insert, wires are run from the chip to a socket on top of the insert, just outside the magnet. To this socket we connect a BNC (Bayonet Neill-Concelman) box, Fig. 3.10 (a). This box allows us to connect between the measurement digital multimeters (DMMs) and the chip carrier, and hence ultimately to our device. Fig. 3.10 (b) shows the layout of one of our typical eight-legged Hall bars. In a typical DC (direct current) measurement set up, current would be passed between A and E, with

the Hall voltage recorded with a DMM between B and H, and another DMM recording the longitudinal voltage drop between B and D. Depending on the exact experiment, the current was either provided by a battery-powered constant power source or a source measurement unit (SMU). Use of the battery powered source is ideal since it avoids any mains interference, and hence was used whenever we required a constant current. However, for more complicated current sweeps with constantly varying current, we had to use the SMU.

Our Hall bar as shown in Fig. 3.10 (a) is initially orientated inside the magnet such that the magnetic field comes straight out of the page towards us, i.e. perpendicular to A-E (current) and B-H (Hall voltage). Our insert is equipped with a rotation mechanism which allows us to change this orientation during measurement. Magnetic field sweeps are controlled by a LabVIEW program, which both controls the magnet and records the DMMs automatically.

Bibliography

[1] W. Choi, I. Lahiri, R. Seelaboyina, and Y. S. Kang, Crit. Rev. Solid State **35**, 52 (2010).

[2] K. S. Novoselov, A. K. Geim, S. V. Morozov, D. Jiang, Y. Zhang, S. V. Dubonos, I. V. Grigorieva, and A. A. Firsov, Science **306**, 666 (2004).

[3] N. D. Mermin, Phys. Rev. **176**, 250 (1968).

[4] L. D. Landau and E. M. Lifshitz, *Statistical Physics: Theory of the Condensed State*, 3rd ed. (Pergamon Press, 1980).

[5] J. C. Meyer, A. K. Geim, M. I. Katsnelson, K. S. Novoselov, T. J. Booth, and S. Roth, Nature **446**, 60 (2007).

[6] P. Blake, E. W. Hill, A. H. Castro Neto, K. S. Novoselov, D. Jiang, R. Yang, T. J. Booth, and A. K. Geim, Appl. Phys. Lett. **91**, 063124 (2007).

[7] K. Bolotin, K. Sikes, Z. Jiang, M. Klima, G. Fudenberg, J. Hone, P. Kim, and H. Stormer, Solid State Commun. **146**, 351 (2008).

[8] E. Pallecchi, M. Ridene, D. Kazazis, C. Mathieu, F. Schopfer, W. Poirier, D. Mailly, and A. Ouerghi, Appl. Phys. Lett. **100**, 253109 (2012).

[9] K. V. Emtsev, A. Bostwick, K. Horn, J. Jobst, G. L. Kellogg, L. Ley, J. L. McChesney, T. Ohta, S. A. Reshanov, J. Röhrl, E. Rotenberg, A. K. Schmid, D. Waldmann, H. B. Weber, and T. Seyller, Nat. Mater. **8**, 203 (2009).

[10] J. Hass, R. Feng, T. Li, X. Li, Z. Zong, W. A. de Heer, P. N. First, E. H. Conrad, C. a. Jeffrey, and C. Berger, Appl. Phys. Lett. **89**, 143106 (2006).

[11] J. Borysiuk, J. Sołtys, and J. Piechota, J. Appl. Phys. **109**, 093523 (2011).

[12] C. Berger, Z. Song, X. Li, X. Wu, N. Brown, C. Naud, D. Mayou, T. Li, J. Hass, A. N. Marchenkov, E. H. Conrad, P. N. First, and W. A. de Heer, Science **312**, 1191 (2006).

[13] W. Gannett, W. Regan, K. Watanabe, T. Taniguchi, M. F. Crommie, and A. Zettl, Appl. Phys. Lett. **98**, 242105 (2011).

[14] S. J. Chae, F. Güneş, K. K. Kim, E. S. Kim, G. H. Han, S. M. Kim, H.-J. Shin, S.-M. Yoon, J.-Y. Choi, M. H. Park, C. W. Yang, D. Pribat, and Y. H. Lee, Adv. Mater. **21**, 2328 (2009).

[15] C. Mattevi, H. Kim, and M. Chhowalla, J. Mater. Chem. **21**, 3324 (2011).

[16] X. Li, W. Cai, J. An, S. Kim, J. Nah, D. Yang, R. Piner, A. Velamakanni, I. Jung, E. Tutuc, S. K. Banerjee, L. Colombo, and R. S. Ruoff, Science **324**, 1312 (2009).

[17] S. Bae, H. Kim, Y. Lee, X. Xu, J.-S. Park, Y. Zheng, J. Balakrishnan, T. Lei, H. R. Kim, Y. I. Song, Y.-J. Kim, K. S. Kim, B. Ozyilmaz, J.-H. Ahn, B. H. Hong, and S. Iijima, Nat. Nanotech. **5**, 574 (2010).

[18] P. Rai-Choudhury, *Handbook of Microlithography, Micromachining, and Microfabrication. Volume 1: Microlithography*, 1st ed. (Society of Photo-Optical Instrumentation Engineers, 1997).

[19] P. Otellini (Intel Roadmap 2012, 2012).

[20] J. J. Licari, *Coating Material for Electronic Applications: Polymers, Processing, Reliability, Testing*, 1st ed. (William Andrew, 2003).

[21] W. Haynes, *CRC Handbook of Chemistry and Physics*, 92nd ed. (CRC Press, 2011).

[22] E. Lassner and S. W. D., *Tungsten: Properties, Chemistry, Technology of the Element, Alloys, and Chemical Compounds*, 1st ed. (Springer, 1999).

[23] M. A. George, Q. C. Bao, I. W. Sorensen, W. S. Glausinger, and T. T., J. Vac. Sci. Technol. A **8**, 1491 (1990).

[24] A. C. Ferrari, J. C. Meyer, V. Scardaci, C. Casiraghi, M. Lazzeri, F. Mauri, S. Piscanec, D. Jiang, K. S. Novoselov, S. Roth, and a. K. Geim, Phys. Rev. Lett. **97**, 187401 (2006).

[25] J. a. Robinson, M. LaBella, M. Zhu, M. Hollander, R. Kasarda, Z. Hughes, K. Trumbull, R. Cavalero, and D. Snyder, Appl. Phys. Lett. **98**, 053103 (2011).

Chapter 4

Energy Relaxation for Hot Dirac Fermions in Graphene and Breakdown of the Quantum Hall Effect

---

In this chapter, energy loss rates for hot-carriers in graphene are experimentally investigated by observing the amplitude of Shubnikov-de Haas oscillations as a function of electric field. The carrier energy loss in graphene is shown to follow the predictions of deformation-potential coupling going as $\sim T^4$ at carrier temperatures up to $\sim$100K, and that deformation-potential theory, when modified with a limiting phonon relaxation time, is valid up to several hundred kelvin. Additionally we investigate the breakdown of the quantum Hall effect and show that energy loss rates in graphene are around 10 times larger than GaAs at low temperatures. This leads to significantly higher breakdown currents per micrometer, and we report a measured breakdown current of $8\mu A/\mu m$.

4.1 Introduction

Graphene has been hailed in the few years since its discovery as the ideal material for a range of applications from gas sensors to touch screens. This is in large part due to its unusual properties, many of which are ultimately derived from its unique linear electronic dispersion relation. One of the most exciting potential uses for graphene is as a successor to silicon for microchip manufacture. Indeed the semiconductor industry roadmap [1] lists graphene as a leading candidate to replace silicon in nano-electronics. For such a use it has many favourable properties which include: ultra-high room temperature mobility [2] of $>$10,000 cm^2/(Vs), its ability to integrate to nearly any substrate [3], the stability of its carbon-carbon bond, its single atom thickness which should allow for greater gate length scalability according to scaling theory [4], and the fact that it is amenable to conventional planar processing techniques.

As the size of electronics goes down the power density increases and as a result heat management is now a primary constraint in operating performance. It is therefore of great practical as well as theoretical interest to understand how energy is lost from the carriers in graphene to its lattice. There have been a number of theoretical calculations of the energy loss rate per carrier [5, 6], but to date there have only been limited experimental results reported. In this chapter, measurements of the energy loss per carrier in the regime of total energy loss $\sim$1 - 500Wcm^{-2} are reported, which are comparable to those found in modern central processor units.

The large value of the cyclotron energy $\hbar\omega_c$ for graphene also means that the beginnings of quantum Hall behaviour can be observed at room temperature [2] leading to suggestions that it would be a good material for quantum Hall resistance standards applications. Results to date on exfoliated graphene have not reported particularly high breakdown currents [7], whereas by contrast reports on epitaxial graphene [8, 9] suggest

breakdown currents may be much higher than those for GaAs [10]. We demonstrate here that high breakdown currents can be observed for exfoliated graphene and relate these to the energy loss rates.

Our measurements of carrier heat loss have been taken in an intermediate temperature regime using magneto-transport measurements with carrier temperatures from 1.5K to around 120K. Most previous experimental work on energy loss rates in graphene has been done using optical excitation at much higher energies [11, 12] with non-equilibrium carrier distributions and carrier temperatures in excess of 5000K. In this regime the carrier lifetime has saturated, whereas we are able to show the energy loss rate has a significant dependence on temperature. Previous electrical studies have also concentrated on much higher temperature regimes, up to 1050K [13].

One reason for the considerable advantages of graphene over other materials is that polar-optical phonon scattering and piezo-electric acoustic phonon scattering are negligible up to room temperature and beyond due to the high optic phonon energy and non-ionic bonding. At room temperature, deformation-potential induced electron-acoustic phonon coupling is the only significant intrinsic scattering mechanism, in contrast to most other semiconductors, where electron-optical phonon coupling is dominant. In all but the cleanest suspended samples, however, scattering from substrate phonons and charged impurity scattering will tend to dominate [14], with the high mobilities observed at room temperature [2] being observable only in ultra-clean samples, and ultra-high mobilities in suspended samples [15]. This might lead one to expect that electron energy loss rates in graphene would be rather small, however we demonstrate here that this is not the case, in agreement with theoretical predictions from Kubakaddi [5]. One consequence of this is that graphene has considerable potential for quantum Hall resistance standards capable of operating at high current densities.

4.2 Methodology

4.2.1 Sample preparation

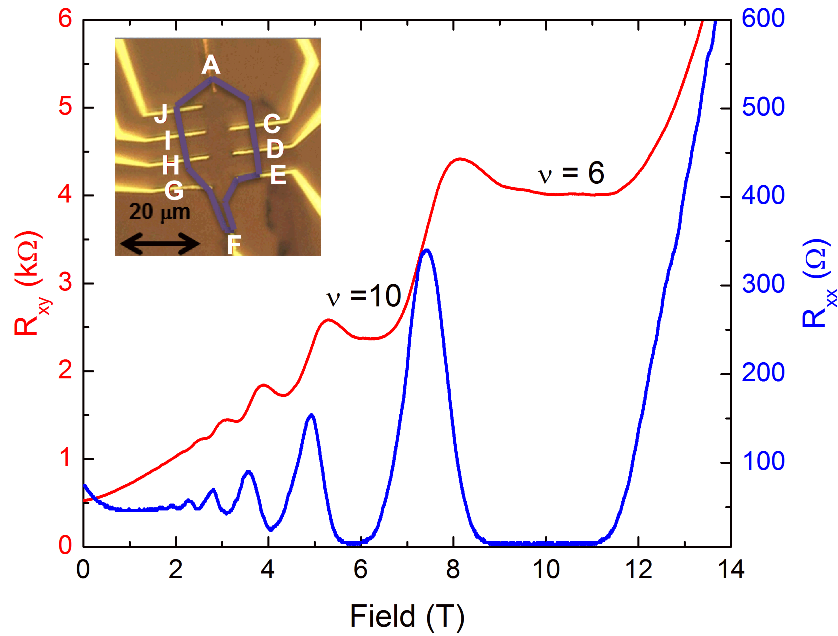

Figure 4.1: Example R_{xx} & R_{xy} quantum Hall effect traces from our device. The insert to the figure shows the layout of our device, and the outline of the monolayer graphene sheet is highlighted, clearly showing all gold contacts reaching inside the flake in an internal contacting geometry. The traces in this figure were taken in a non-standard transverse geometry with the current running from D to H. The clear, adjacent $\nu = 6$, 10 plateaux demonstrate our sample to be monolayer graphene.

The graphene was produced by the now standard micro-mechanical exfoliation technique [16, 17] onto a silicon wafer with a 300nm SiO_2 layer. The wafer was then diced into chips. Bond-pads and alignment marks were written using e-beam lithography and metal evaporation with a 20nm adhesion layer of chrome and 200nm of gold. The positions of monolayer flakes were identified using the alignment marks, and hence the final fingers

to the flake were written in a similar manner. Crucially, however, the final fingers were made by deposition of gold only, without a chrome adhesion layer, as preliminary work showed that this gold-only contacting dramatically reduced the contact resistances to our devices. Our ungated Hall bar devices were deliberately not mesa-etched giving a non-standard internal contacting geometry. This was done in order to reduce the role of defects from edge states, by physically separating the currents from flowing near the edge of the device, and by minimizing the role of defect states and doping introduced by the mesa-etching process [18]. The device used in our experiments was connected in a standard Hall bar arrangement (inset to Fig. 4.1).

4.2.2 Measurement and data processing

Electrical measurements were carried out using a helium cooled 21 Tesla Oxford Instruments magnet. We used a Keithley SMU to supply current to the Hall bar. All electrical measurements were made using Keithley 2000 DMMs. The samples were immersed directly in liquid helium at 1.5K throughout. The area in which current flows is assumed to be internal to the area defined by the gold contacts, which have a much lower resistance than the graphene. When the applied current was passed along the length of the device we took the relevant area to be the whole of the device inside the contacts. Most of our data was, however, collected in an alternative geometry, with the current passed across the width of the device. In this case simple Laplace equation modelling [19], taking the current contacts as point contacts inside a uniformly conducting system, showed that the area of current flow is approximately circular with a diameter equal to the distance between the two current contacts.

4.3 Results

4.3.1 Energy loss rate

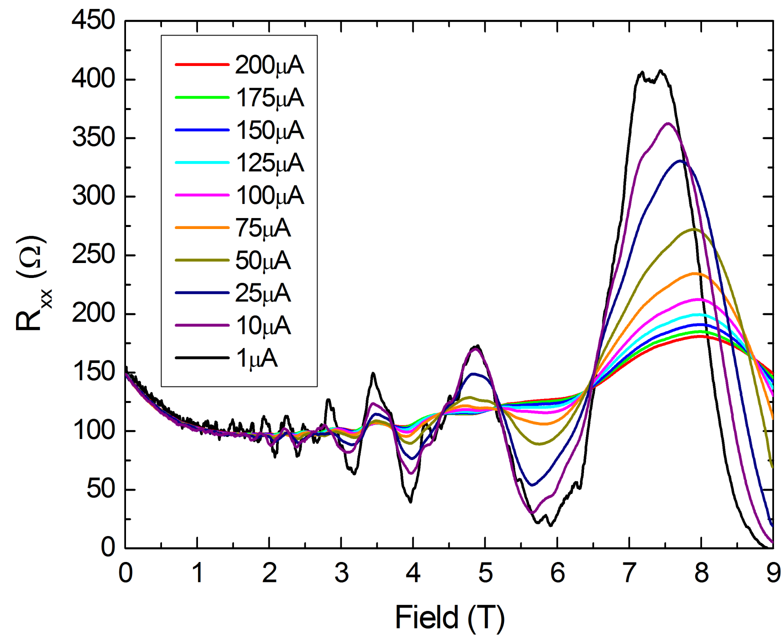

Figure 4.2: R_{xx} measurements taken for a range of currents from 1μA to 200μA. Damping of the Shubnikov-de Haas oscillations are clearly observed. This data was again taken in a non-standard geometry this time with the current across the width of the sample between C & I

We investigated carrier energy loss to the lattice by measuring the Shubnikov-de Haas oscillations and analysing the damping of these oscillations to determine the carrier temperature, as has been reported previously in a number of different materials [10, 20–22]. This is based on the assumption that there is a very rapid thermalisation of the carriers which takes place on a time scale of tens of femtoseconds, leaving a Bolzmann distribution of hot-carriers which then lose energy to the lattice much more slowly.

Experiments in graphene and related materials strongly support this assumption of very rapid carrier thermalisation [11, 12, 23].

At low DC and AC currents we observe typical well-resolved quantum Hall behaviour, Fig. 4.1, with $\nu = 6$ & $\nu = 10$ plateaux well defined in R_{xy}, with the associated R_{xx} at zero resistance to within our measurement accuracy. The plateaux numbers observed follow the 2 + 4n pattern which confirms that our sample is monolayer graphene [24]. A series of measurements at constant DC currents ranging from 1μA to 200μA are shown in Fig. 4.2. As the current increases, the amplitude of the oscillations decreases, due to the increased carrier temperature from current heating. Using the theory of Ando [25] we calculate the carrier temperatures (T_e) from

$$\frac{\Delta\rho}{\rho} = f(\omega_c\tau)\frac{\chi}{\sinh\chi}e^{-\frac{\pi}{\omega_c\tau_q}}, \tag{4.1}$$

where

$$\chi = \frac{2\pi^2 k_B T_e}{\hbar\omega_c}, \tag{4.2}$$

and $\hbar\omega_c$ is calculated from the Landau level separations from

$$E_N = \mathrm{sgn(N)} \times c^* \sqrt{2e\hbar B|N|}, \tag{4.3}$$

where $|N|$ is the Landau quantum index and B is the magnetic field. The Dirac velocity, c^* [2, 26], is taken to be 1.1 x 10^6 ms^{-1}. We estimate that our calculated values for T_e have an associated random error of around 3-5%, with the error increasing at larger currents due to the smaller measured amplitudes.

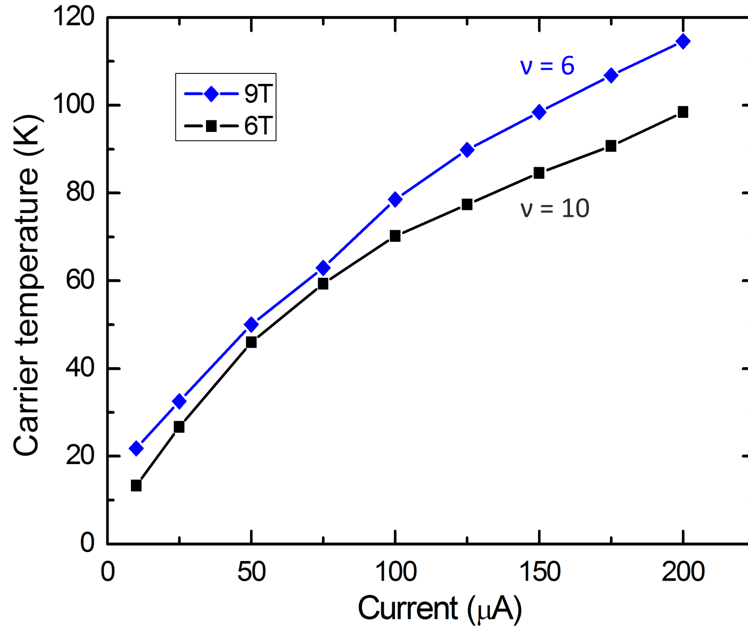

Figure 4.3: Measured carrier temperature as a function of input current for ν = 6, 10. Note the temperature attained is far in excess of that of the lattice, which was held at 1.5K throughout, and hence the device is operating in a hot-carrier regime.

Fig. 4.3 shows a plot of T_e as a function of current for the two plateaux. All measurements give electron temperatures in the range 20 - 120 K, demonstrating that we are operating in the non-equilibrium hot-carrier regime.

From this data we calculate the energy loss per carrier, taking into account that for short channel devices, the dominant power input is at the current injecting contacts [27] where the voltage drop corresponds to the quantum Hall resistance, R_K, using

$$E_{loss} = I^2 \frac{R_K}{\nu} / N_e A \tag{4.4}$$

where we have used the measured charge carrier density of $\mathrm{N}_e = 1.39 \cdot 10^{12}\mathrm{cm}^{-2}$ and device area as $\mathrm{A} = 5.9 \cdot 10^{-11}\mathrm{m}^2$.

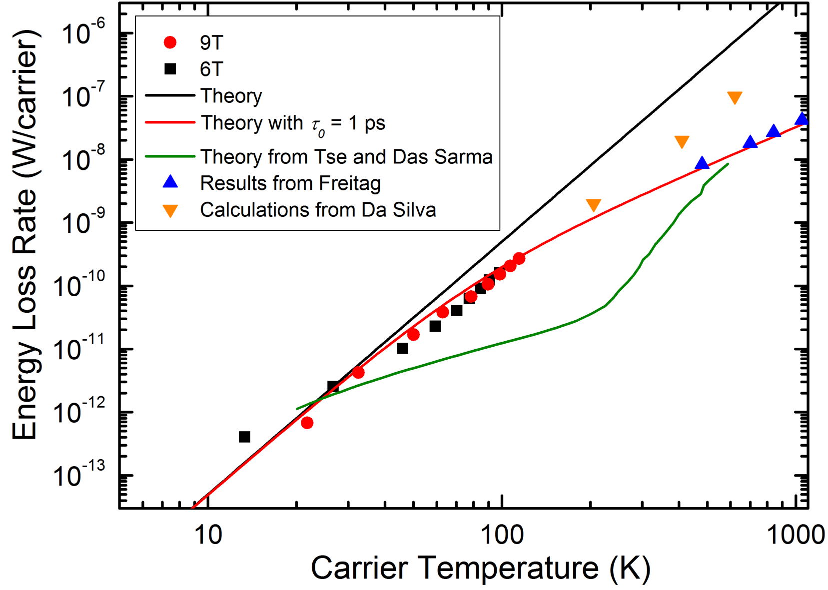

Figure 4.4: Carrier energy loss rate as a function of carrier temperature. Data from two plateaux are shown for 9T and 6T corresponding to $\nu = 6, 10$ respectively. Superimposed in black is the unmodified theoretical prediction from Kubakaddi [5]. The red theory line is the prediction from Kubakaddi modified with the addition of a constant phonon relaxation time of 1ps. The green theory line is a prediction from Tse and Das Sarma [6].Finally some high lattice temperature data from Freitag [13], and calculations including silicon dioxide substrate phonons from Da Silva [28] are included.

Combining this with the carrier temperature data gives the energy loss rate per carrier as a function of carrier temperature (Fig. 4.4). As found in other systems at low temperatures [10, 20–22, 29, 30] this shows an approximate power law dependence $\sim T^3 - T^4$. Theoretical predictions for energy loss rates are shown from the work of Kubakaddi [5] for acoustic phonons, extrapolated from low temperature values as

$$P = \alpha(T_e^4 - T_L^4), \tag{4.5}$$

where α is weakly carrier density dependent. Also shown are the theoretical predictions from Tse and Das Sarma [6]. These suggest a significantly lower contribution from

acoustic phonons, with high temperature energy loss, above ∼250K, being dominated by optical phonons. We find the Tse and Das Sarma prediction fits our data poorly as it significantly underestimates the energy loss rate for the majority of our measured range. Additionally the predicted power dependence of the range dominated by acoustic phonons is $\sim T^2$ which is lower than typically seen in other systems [10, 20–22, 29, 30]. It is clear that the Kubakaddi acoustic phonon prediction [5], based on a deformation-potential of 19 eV, fits very well at lower temperatures but the extrapolation increasingly overstates the measured values at higher carrier temperatures. Kubakaddi suggests that the theory requires extension [5] to provide accurate predictions in this range. The electron energy loss time (τ_e) can be deduced from P using

$$\tau_e = \frac{\pi^2 k_B^2 (T_e^2 - T_L^2)}{3 E_F P}, \tag{4.6}$$

where T_L is the lattice temperature. This gives

$$\tau_e = \frac{\pi^2 k_B^2}{3 E_F \alpha T_e^2}, \tag{4.7}$$

when high $T_e \gg T_L$. At high temperatures τ_e is expected to saturate due to hot phonon and higher order effects. This has been measured optically for high energies both for doped and undoped samples [11, 12, 23, 31]. For doped samples comparable to that studied here the relaxation time has been measured to be in the range 0.4 - 1.5ps. Adding τ_0 as a limiting factor we expect

$$\tau_e = \frac{\pi^2 k_B^2}{3 E_F \alpha T_e^2} + \tau_0. \tag{4.8}$$

In our modelling we have selected a value of 1ps for the phonon relaxation time,

which is in the middle of the measured range of values for doped graphene. We use this expression to re-calculate P from Eq. (4.6), giving

$$P = \frac{\pi^2 k_B^2 \alpha T_e^4}{\pi^2 k_B^2 + 3E_F \alpha T_e^2 \tau_0}. \tag{4.9}$$

This expression gives good agreement with experiment for the whole temperature range, as shown in red on Fig. 4.4. On the figure we also include measurements from Freitag [13] of lattice temperature, a lower bound on the carrier temperature, at very high electron energy loss rates [13] and calculations for electron temperatures including the silicon dioxide substrate phonons [28]. These suggest that the deformation-potential scattering is still making a substantial contribution to energy loss rates up to temperatures of many hundreds of kelvin and that Eq. (4.9) provides a good empirical description of the total energy loss rate.

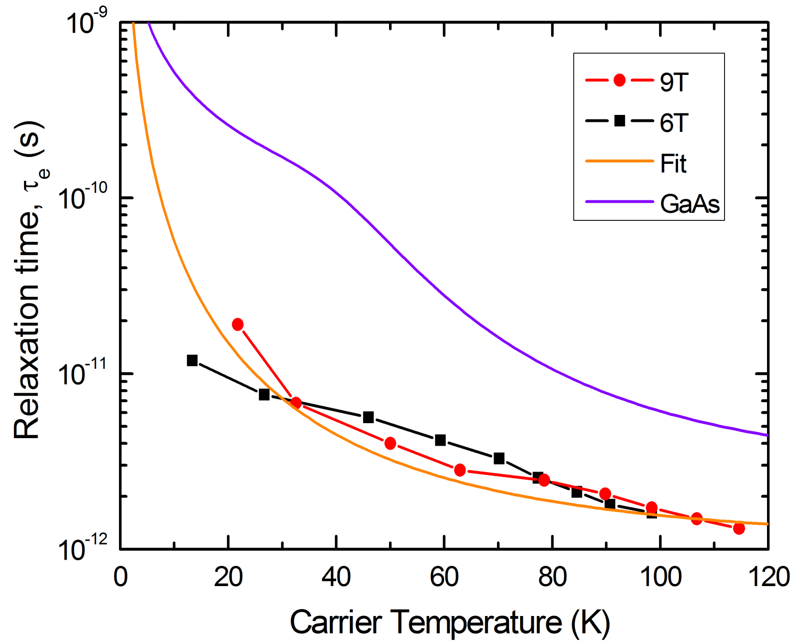

Figure 4.5: Relaxation time versus carrier temperature. A good fit is observed to the theoretical prediction, especially in the range of 30K-80K, which covers the regime of quantum Hall breakdown. A trace for GaAs [32] is shown by way of comparison. The GaAs has a relaxation time an order of magnitude slower than that of graphene across the entire temperature range.

The electron temperature dependence of τ_e is shown in Fig. 4.5, as deduced from experiment and Eq. (4.6), together with corresponding data for GaAs [32]. This shows the initially rather surprising result that τ_e is typically an order of magnitude less than GaAs over the whole temperature range studied, resulting in a much higher energy loss rate in graphene. This is despite the fact that optic phonon emission is making a strong contribution to the GaAs energy loss rate above $\sim$50K.

4.3.2 Quantum Hall effect breakdown

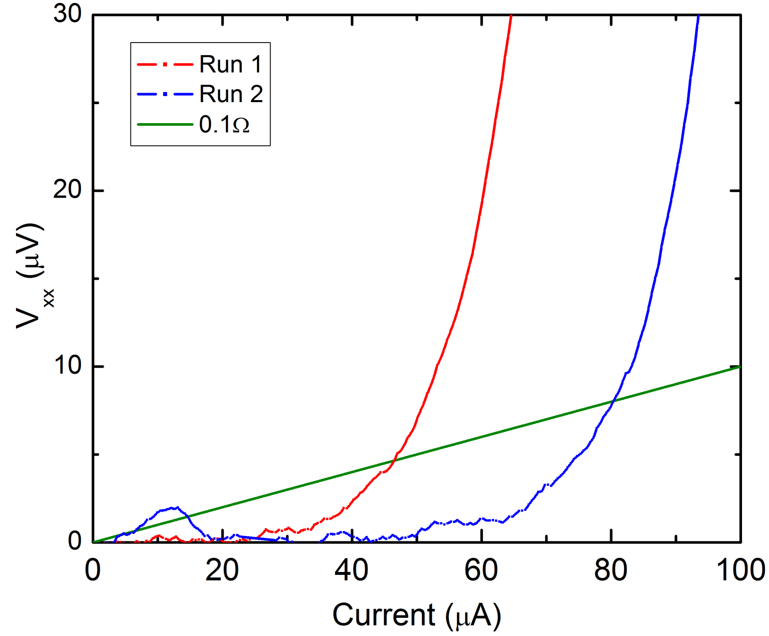

Figure 4.6: High current breakdown of $\nu = 6$ quantum Hall state in graphene. Defined as $R_{xx} < 0.1\Omega$ (green line), the breakdown current is 80μA at 9.5 Tesla for contacts 10μm apart. Two successive runs are shown demonstrating the effect of current annealing on the breakdown behaviour. This data was taken in the same configuration as the Shubnikov-de Haas data, with the current running from C to I.

To explore the potential of this system further as a resistance standard, we also examined the breakdown of the quantum Hall effect (QHE) at high currents. Fig. 4.6 shows typical curves for two measurements of V_{xx} at the resistivity minimum for $\nu = 6$. The appearance of a finite resistivity is used to predict the quantization accuracy, which is usually related to the Hall resistivity by $\Delta\rho_{xy} = -S\rho_{xx}$ where S is a constant related to the width of the probe arms over the width of the Hall bar, usually in the region 0.1 to 1 [33–35]. The breakdown shows fairly typical behaviour, with a relatively 'soft' increase in resistance.

The sample exhibits the previously reported current annealing behaviour [7, 36] where the critical current increases as a result of passing a high current through the sample, probably due to the removal of physisorbed molecules which act as scattering centres. Using a fairly stringent definition [37] for the onset of breakdown at $R_{xx} = 0.1\Omega$ gives breakdown currents of $\sim 80\mu$A, flowing between contacts C & I of the insert to Fig. 4.1 corresponding to a peak current density of $\sim 10\mu$A/μm. This compares with previously reported [7, 8] values of around 2-3$\mu A/\mu m$ at the considerably lower lattice temperature of 0.35K for exfoliated graphene, and more recently values of around 10μA/μm have been reported [9] in polymer gated epitaxial graphene.

We attribute this improvement over previous samples to two factors. Firstly, our improved contacting procedures, using gold without any adhesion layer for the region where the tracks contact the graphene. This gave an estimated contact resistance of 150-300$\Omega\mu$m from a comparison of two and four terminal measurements of the quantum Hall resistance on a similar sample using an identical contacting procedure. This compares very favourably to Ti/Au, Cr/Au, Ni/Au which have typical contact resistances of $10^3 - 10^5\Omega\mu$m, and even compares favourably to Ti/Pd/Au which has a contact resistance of around 750$\Omega\mu$m [38–42]. Additionally we attribute the improvement to our use of an internal contacting geometry which minimizes scattering from defect edge states. These breakdown current values demonstrate that there is almost an order of magnitude increase over the largest values reported [10, 43] for GaAs devices which are typically in the range 1-2$\mu A/\mu m$ for bulk materials, though higher breakdown current densities may be achievable in narrow channel devices [44].

The observation of enhanced breakdown currents in graphene is due to the combination of two favourable factors: the increased cyclotron energy combined with the larger energy loss rates measured above. This can be seen from the model most commonly

used to predict the breakdown of QHE, which is the bootstrap-type electron heating model of Komiyama and Kawaguchi [45], which is based on the runaway heating which occurs when the QHE begins to break down. Modifying this theory for the two-fold valley degeneracy of graphene, the breakdown field E_y is predicted to be

$$E_y = \sqrt{\frac{4B\hbar\omega_c}{\eta e \tau_e}}, \tag{4.10}$$

where $\eta = 4$ for graphene, to account for the two-fold spin and two-fold valley degeneracy.

At 10 Tesla:	GaAs (ν=2)	Graphene (ν=6)	Graphene (ν=2)
$\hbar\omega_c$ (meV)	17	51.6	126
τ_e (ps)	100	3	4
$I_b = \nu\ \sigma_0\ E_b$ (μA / μm)	4.7	93	43
T (K)	4	12	30

Table 4.1: Data calculated for the cyclotron energy, carrier relaxation time, breakdown current per micrometer and thermal breakdown temperature, with carrier densities set for each plateau such that the labelled plateaux all occurred at 10 Tesla.

The breakdown currents found above correspond to a carrier temperature of 50-70K where it was found that τ_e ~3ps. This value is ~30 times shorter than for GaAs which suggests that breakdown currents will be much higher in graphene as a result of this. In fact Eq. (4.10) suggests that this factor will be more important than the increased value of $\hbar\omega_c$ for graphene. Using Eq. (4.10) we compare the predictions for graphene ($\nu = 2,6$) with GaAs ($\nu = 2$), the current gold-standard for resistance metrology measurements, shown in Table 4.1. The carrier densities are adjusted to correspond to each plateau occurring at 10T. The bootstrap heating model predicts that graphene should be 10 - 20 times better than GaAs, although the predicted values are significantly higher than those observed to date for both materials. In the experiments above breakdown

current densities approximately 5 - 10 times larger than those observed in good GaAs Hall bars were obtained, suggesting that further optimisation might be able to increase the breakdown currents in graphene still further. It is also worth noting that for this device we did not attempt an extensive optimization of the annealing procedure, and in previous work [8] significant improvements in breakdown currents were observed when decreasing temperature from 1.5K to 0.35K. The theory has thus allowed us to conclude that the majority of the improvement to the breakdown current in graphene is in fact due to its high energy loss rate associated with the small value of τ_e.

A further advantage of graphene for metrology is that it could be used to allow such measurements to be carried out at much higher temperatures due to the higher cyclotron energies. In order to achieve the accuracy that standards require [8], currently about 1 part in 10^{10}, which corresponds to

$$\rho_{xx} \ll 10^{-10}\rho_{xy}, \tag{4.11}$$

where for high mobility samples

$$\rho_{xx} \approx \frac{1}{\nu\sigma_0}\exp(-\frac{\hbar\omega_c}{2k_BT}), \tag{4.12}$$

due to thermal excitations across the Landau gap. To get the required 1 part in 10^{10} accuracy, we need

$$k_BT < \hbar\omega_c/50. \tag{4.13}$$

Using this criterion we calculate the temperature at which thermal breakdown of

the QHE will occur. This is shown in Table 4.1. As can be seen thermal breakdown of the QHE should occur at much higher temperatures in graphene than in GaAs and, crucially, it should be possible to achieve standards level quantization at temperatures up to 10K, in contrast to the 0.3K typically used in GaAs standards measurements.

4.4 Conclusions

We have shown experimentally that electron energy loss in graphene follows the predictions of deformation-potential coupling going as $\sim T^4$ at carrier temperatures up to $\sim$100K. We have shown that this is in good agreement with deformation-potential theory [5] when modified with a limiting relaxation time. From this we conclude that the energy relaxation time in graphene is over an order of magnitude shorter than that in GaAs.

As a result of the much shorter relaxation time in particular, we expect that QHE breakdown currents should be much higher in graphene when compared to GaAs. We have observed this using exfoliated graphene and the prediction suggests that future improvements to sample preparation could allow for yet higher breakdown currents. High breakdown currents have been observed at Helium 4 temperatures and estimates suggest that high breakdown currents should be observable at even higher temperatures which would allow for easier fabrication of cryogen-free metrology kits.

Bibliography

[1] ITRS (International Technology Roadmap for Semiconductors, 2009).

[2] K. S. Novoselov, Z. Jiang, Y. Zhang, S. V. Morozov, H. L. Stormer, U. Zeitler, J. C. Maan, G. S. Boebinger, P. Kim, and A. K. Geim, Science **315**, 1379 (2007).

[3] T. Palacios, Nat. Nanotech. **6**, 464 (2011).

[4] F. Schwierz, Nat. Nanotech. **5**, 487 (2010).

[5] S. S. Kubakaddi, Phys. Rev. B **79**, 075417 (2009).

[6] W.-K. Tse and S. Das Sarma, Phys. Rev. B **79**, 235406 (2009).

[7] A. J. M. Giesbers, G. Rietveld, E. Houtzager, U. Zeitler, R. Yang, K. S. Novoselov, A. K. Geim, and J. C. Maan, Appl. Phys. Lett. **93**, 222109 (2008).

[8] A. Tzalenchuk, S. Lara-Avila, A. Kalaboukhov, S. Paolillo, M. Syväjärvi, R. Yakimova, O. Kazakova, T. J. B. M. Janssen, V. Fal'ko, and S. Kubatkin, Nat. Nanotech. **5**, 186 (2010).

[9] T. J. B. M. Janssen, A. Tzalenchuk, R. Yakimova, S. Kubatkin, S. Lara-Avila, S. Kopylov, and V. I. Fal'ko, Phys. Rev. B **83**, 233402 (2011).

[10] Y. Ma, R. Fletcher, E. Zaremba, M. D'Iorio, C. T. Foxon, and J. J. Harris, Phys. Rev. B **43**, 9033 (1991).

[11] D. Sun, Z. Wu, C. Divin, X. Li, C. Berger, W. de Heer, P. First, and T. Norris, Phys. Rev. Lett. **101**, 157402 (2008).

[12] J. M. Dawlaty, S. Shivaraman, M. Chandrashekhar, F. Rana, and M. G. Spencer, Appl. Phys. Lett. **92**, 042116 (2008).

[13] M. Freitag, M. Steiner, Y. Martin, V. Perebeinos, Z. Chen, J. C. Tsang, and P. Avouris, Nano Lett. **9**, 1883 (2009).

[14] J.-H. Chen, C. Jang, S. Xiao, M. Ishigami, and M. S. Fuhrer, Nat. Nanotech. **3**, 206 (2008).

[15] K. Bolotin, K. Sikes, Z. Jiang, M. Klima, G. Fudenberg, J. Hone, P. Kim, and H. Stormer, Solid State Commun. **146**, 351 (2008).

[16] K. S. Novoselov, A. K. Geim, S. V. Morozov, D. Jiang, Y. Zhang, S. V. Dubonos, I. V. Grigorieva, and A. A. Firsov, Science **306**, 666 (2004).

[17] P. Blake, E. W. Hill, A. H. Castro Neto, K. S. Novoselov, D. Jiang, R. Yang, T. J. Booth, and A. K. Geim, Appl. Phys. Lett. **91**, 063124 (2007).

[18] L. Liu, S. Ryu, M. R. Tomasik, E. Stolyarova, N. Jung, M. S. Hybertsen, M. L. Steigerwald, L. E. Brus, and G. W. Flynn, Nano Lett. **8**, 1965 (2008).

[19] W. J. Duffin, *Electricity and Magnetism*, 4th ed. (McGraw Hill Publishing Co., 1990).

[20] D. R. Leadley, R. J. Nicholas, J. J. Harris, and C. T. Foxon, Semicond. Sci. Technol. **4**, 879 (1989).

[21] G. Stöger, G. Brunthaler, G. Bauer, K. Ismail, B. S. Meyerson, J. Lutz, and F. Kuchar, Phys. Rev. B **49**, 10417 (1994).

[22] R. Leturcq, D. L'Hôte, R. Tourbot, V. Senz, U. Gennser, T. Ihn, K. Ensslin, G. Dehlinger, and D. Grützmacher, Europhys. Lett. **61**, 499 (2003).

[23] M. Breusing, C. Ropers, and T. Elsaesser, Phys. Rev. Lett. **102**, 086809 (2009).

[24] V. Gusynin and S. Sharapov, Phys. Rev. Lett. **95**, 146801 (2005).

[25] T. Ando, J. Phys. Soc. Japan **37**, 1233 (1974).

[26] R. Deacon, K.-C. Chuang, R. J. Nicholas, K. S. Novoselov, and A. K. Geim, Phys. Rev. B **76**, 081406 (2007).

[27] U. Klass, W. Dietsche, K. von Klitzing, and K. Ploog, Z. Phys. B **82**, 351 (1991).

[28] A. M. DaSilva, K. Zou, J. K. Jain, and J. Zhu, Phys. Rev. Lett. **104**, 236601 (2010).

[29] R. Fletcher, V. Pudalov, Y. Feng, M. Tsaousidou, and P. Butcher, Phys. Rev. B **56**, 12422 (1997).

[30] E. Chow, H. Wei, S. Girvin, and M. Shayegan, Phys. Rev. Lett. **77**, 1143 (1996).

[31] P. George, J. Strait, J. Dawlaty, S. Shivaraman, M. Chandrashekhar, F. Rana, and M. G. Spencer, Nano Lett. **8**, 4248 (2008).

[32] K. Leo, W. W. Ruhle, and K. Ploog, Phys. Rev. B **38**, 1947 (1988).

[33] F. Delahaye and B. Jeckelmann, Metrologia **40**, 217 (2003).

[34] M. Furlan, Phys. Rev. B **57**, 14818 (1998).

[35] B. Jeckelmann and B. Jeanneret, Online **64**, 1603 (2001).

[36] K. I. Bolotin, K. J. Sikes, J. Hone, H. L. Stormer, and P. Kim, Phys. Rev. Lett. **101**, 096802 (2008).

[37] G. Nachtwei, Physica E **4**, 79 (1999).

[38] B.-C. Huang, M. Zhang, Y. Wang, and J. Woo, Appl. Phys. Lett. **99**, 032107 (2011).

[39] P. Blake, R. Yang, S. Morozov, F. Schedin, L. Ponomarenko, A. Zhukov, R. Nair, I. Grigorieva, K. Novoselov, and A. Geim, Solid State Commun. **149**, 1068 (2009).

[40] S. Russo, M. Craciun, M. Yamamoto, A. Morpurgo, and S. Tarucha, Physica E **42**, 677 (2010).

[41] K. Nagashio, T. Nishimura, K. Kita, and A. Toriumi, Appl. Phys. Lett. **97**, 143514 (2010).

[42] K. Nagashio, T. Nishimura, K. Kita, and A. Toriumi, Jpn. J. Appl. Phys. **49**, 051304 (2010).

[43] S. Kawaji, K. Hirakawa, M. Nagata, T. Okamoto, T. Fukase, and T. Gotoh, J. Phys. Soc. Japan **63**, 2303 (1994).

[44] L. Eaves and F. Sheard, Semicond. Sci. Technol. **1**, 346 (1986).

[45] S. Komiyama and Y. Kawaguchi, Phys. Rev. B **61**, 2014 (2000).

Chapter 5

Energy Loss Rates of Hot Dirac Fermions in Epitaxial, Exfoliated and CVD Graphene

---

Energy loss rates for hot-carriers in graphene have been measured using graphene produced by epitaxial growth on SiC, exfoliation and chemical vapour deposition (CVD). It is shown that the energy loss rates measured with high-field damped Shubnikov-de Haas oscillations correlate well with the temperature dependence of the weak localization peak close to zero field, with the high-field measurements understating the energy loss rates by ∼40% compared to the low-field results. The energy loss rates for all graphene samples follow a universal scaling of T_e^4 at low temperatures and depend weakly on carrier density $\propto n^{-\frac{1}{2}}$, with some evidence for enhancement of the energy loss rate due to disorder in CVD samples. Further, the Fermi velocity of CVD graphene is measured as 1.08 x 10^6 m s^{-1}, though it is noted that the Fermi velocity is expected to have a dependence on the chemical potential at high energies [1].

5.1 Introduction

Despite its remarkable properties, a key problem in the commercialization of graphene has been that the fabrication method used for its discovery, micromechanical exfoliation [2], is not amenable to large-scale commercial production. There are, however, other production methods which can easily be scaled up, such as epitaxial growth on SiC, or chemical vapour deposition (CVD) on thin metal films [3]. While both these techniques are well established, the majority of graphene research is still carried out on exfoliated graphene. The principal reasons for this are the comparative ease of graphene fabrication using this method, and that to date it still produces the highest quality samples [4]. There is therefore a great need for comparisons to be made between graphene produced by the 'research' method, and those produced in a more commercially amenable manner.

Carrier energy loss rates are a particularly important parameter as they influence thermal dissipation and heat management in modern electronics as well as low-temperature applications such as quantum resistance metrology [5] and hot-electron bolometers [6]. Energy loss rates have previously been measured in exfoliated graphene [7, 8], with conflicting results. There has also been theoretical disagreement as to how Dirac fermions in graphene lose energy to the lattice and how this varies with temperature and carrier density [9, 10]. Here we compare the carrier energy loss rates in graphene produced by three different fabrication methods: exfoliation, CVD and epitaxial growth on SiC, for carrier densities ranging from 1 x $10^{11}\,\mathrm{cm}^{-2}$ to 1.6 x $10^{13}\,\mathrm{cm}^{-2}$ using two independent methods (weak localization (WL) and Shubnikov-de Haas (SdH) oscillations) and demonstrate that a single consistent picture exists.

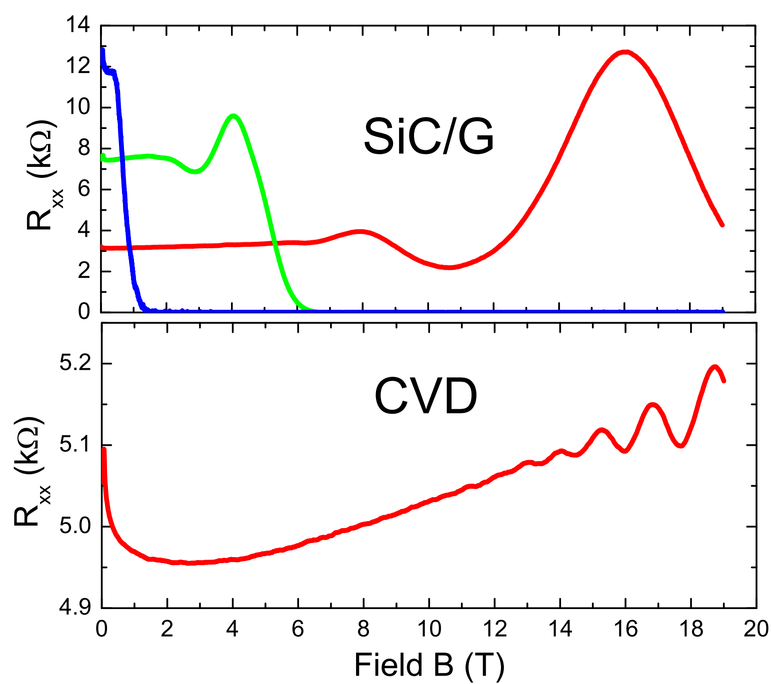

Figure 5.1: Example R_{xx} for the SiC/G and CVD samples. SiC/G, graphene grown epitaxially on SiC, before (Red, n = 1.63 x 10^{12} cm^{-2}, 160 μm x 35 μm), after (Green, n = 4.72 x 10^{11} cm^{-2}), and after further photochemical gating (Blue, n = 1 x 10^{11} cm^{-2}). CVD, graphene grown by CVD onto thin film metal, (n = 1.62 x 10^{13} cm^{-2}, 120 μm x 32 μm).

5.2 Methodology

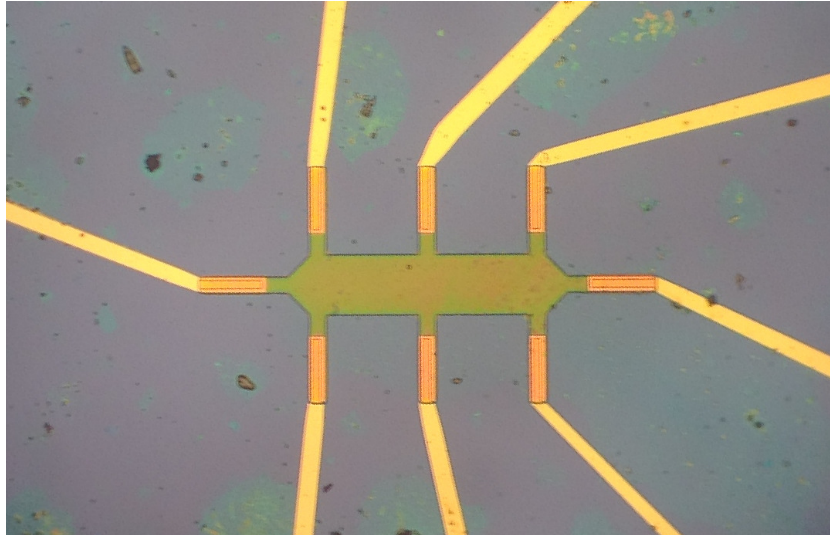

Figure 5.2: A microscope image of a 16 μm wide CVD graphene Hall bar patterned by electron beam lithography. A thin layer of ma-N 1407 photoresist remains on top of the patterned graphene device rendering it clearly perceptible. Gold contacts are visible leading to the device.

The CVD graphene was grown on thin-film copper, subsequently transferred to Si/SiO_2 [11]. The graphene wafers were lithographed by e-beam into Hall bars using gold-only final contacting as described in Chapter 4 (see also [7]). The SiC/Graphene (SiC/G) was epitaxially grown on the Si-terminated face of SiC [12]. Hall bar devices were produced using e-beam lithography and oxygen plasma etching with large area titanium-gold contacting. Photochemical gating is used to control the carrier density in the epitaxial samples due to the impossibility of conventional backgating through the insulating SiC substrate [13]. The polymer gating consisted of a dual polymer layer of PMMA and ZEP520A. The latter acts as a strong acceptor after exposure to deep UV, which acts to photochemically gate the device. All electrical measurements were carried out using DC constant-current sources and multimeters. The CVD graphene was grown by C. T. Lin

& L. J. Li of Academia Sinica. The SiC/G was grown and fabricated by R. Yakimova of Linköping University, S. Lara-Avila of Chalmers University, and T. J. B. M. Janssen, S. Kubatkin & A. Tzalenchuk of NPL.

5.3 Results

5.3.1 Shubnikov-de Haas

The conventional method of measuring energy loss rates is from the temperature dependent damping of SdH oscillations of the heated carriers. This method can be used for high density samples with a sufficient mobility to display sinusoidal oscillations. The damping is caused by thermal broadening of the carrier distribution heated by an applied electric field. The carriers are unable to lose energy at a sufficient rate to reach thermal equilibrium with the lattice and thus heat up [14]. Using theory from Ando [15] we calculate the carrier temperature (T_e) from the damped amplitude, using

$$\frac{\Delta\rho}{\rho} = f(\omega_c\tau)\frac{\chi}{\sinh\chi}e^{-\frac{\pi}{\omega_c\tau_q}}, \tag{5.1}$$

where τ_q is the quantum lifetime and

$$\chi = \frac{2\pi^2 k_B T_e}{\hbar\omega_c}, \tag{5.2}$$

and $\hbar\omega_c$ is calculated from the separation of the N and N+1 Landau levels from

$$E_N = \mathrm{sgn(N)} \times v_F\sqrt{2e\hbar B|N|}, \tag{5.3}$$

where B is the magnetic field and v_F is the Fermi velocity.

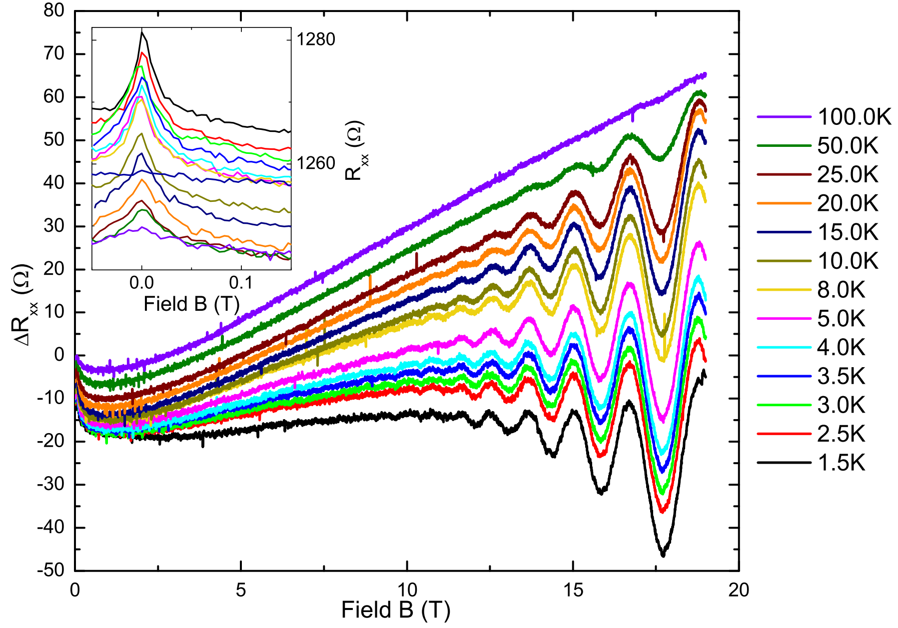

Figure 5.3: R_{xx} for CVD graphene with n = 1.43 x 10^{13} cm^{-2}. All traces taken at 500 nA with the sample space temperature varied from 1.5 K to 100 K. Traces are shifted such that the WL peak is at 0 Ω. The inset shows the WL peak around B = 0 T.

This method for determining the carrier temperature from the Shubnikov-de Haas oscillations has previously been applied to several different materials, including GaAs [14, 16], SiGe [17], as well as in exfoliated graphene [7]. In all these materials, however, the carrier density has been less than 2 x 10^{12} cm^{-2}. For our CVD samples, however, we were dealing with samples with carrier densities nearly an order of magnitude higher. To validate the method at these high carrier densities, the effect of raising the lattice temperature on damping was tested directly. Traces were taken at low current for a variety of lattice temperatures (Fig. 5.3). A low current was used to avoid additional carrier heating above the lattice temperature.

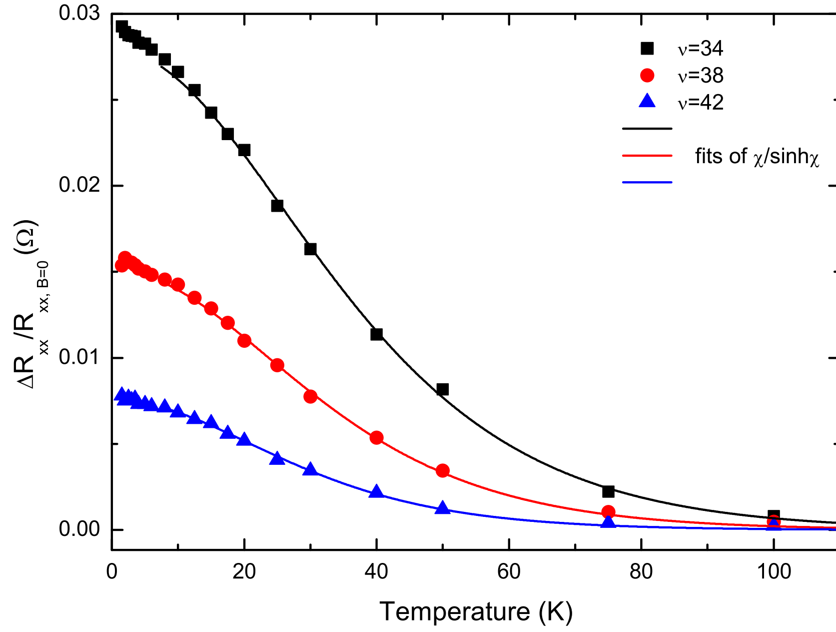

Figure 5.4: Temperature dependence of the normalized amplitude of Shubnikov-de Haas oscillations from a CVD sample with n = 1.62 x $10^{13}\,\mathrm{cm}^{-2}$, at the three smallest measured filling factors. Fits of $\frac{\chi}{\sinh\chi}$ are shown from which the Fermi velocity is derived.

Fig. 5.4 shows the amplitudes of the SdH oscillations for the three smallest filling factors as a function of temperature. The validity of Eq. (5.1) for the CVD samples is demonstrated by fitting the data points with the temperature dependent factor $\frac{\chi}{\sinh\chi}$ from Eqs. (5.1) & (5.2) using

$$\frac{\Delta R_{xx}}{R_{xx,B=0}} = A\frac{(T/b)}{\sinh(T/b)}. \tag{5.4}$$

From the figure, the data are shown to be well fitted by this equation, and from fitting parameter b, the Fermi velocity v_F can be calculated using

$$\omega_c = \sqrt{\frac{2eB}{\hbar}}(\sqrt{N+1} - \sqrt{N})v_F. \tag{5.5}$$

Filling factor ν	Field B(T)	Landau level N	Velocity v_F (ms^{-1})
34	17.69	8	1.06 x 10^6
38	15.83	9	1.09 x 10^6
42	14.33	10	1.10 x 10^6
		Average v_F =	1.08 x 10^6

Table 5.1: Values of v_F calculated from the fitting of the temperature dependence of the SdH amplitudes. Data taken in CVD graphene with a carrier density of 1.43 x $10^{13}\,cm^{-2}$.

The measured values of v_F are shown in Table 5.1. We find a value of v_F = 1.084 x $10^6\,ms^{-1}$ for the CVD graphene sample which had a carrier density of 1.43 x $10^{13}\,cm^{-2}$. This value of v_F is in good agreement with the values found at lower carrier densities for graphene produced by exfoliation [18], or epitaxially on SiC [19] of 1.1 x $10^6\,ms^{-1}$. This implies that the Fermi velocity remains approximately constant to energies of at least E_F = 478 meV, though it is noted that the Fermi velocity is expected to have a dependence on the chemical potential at high energies [1].

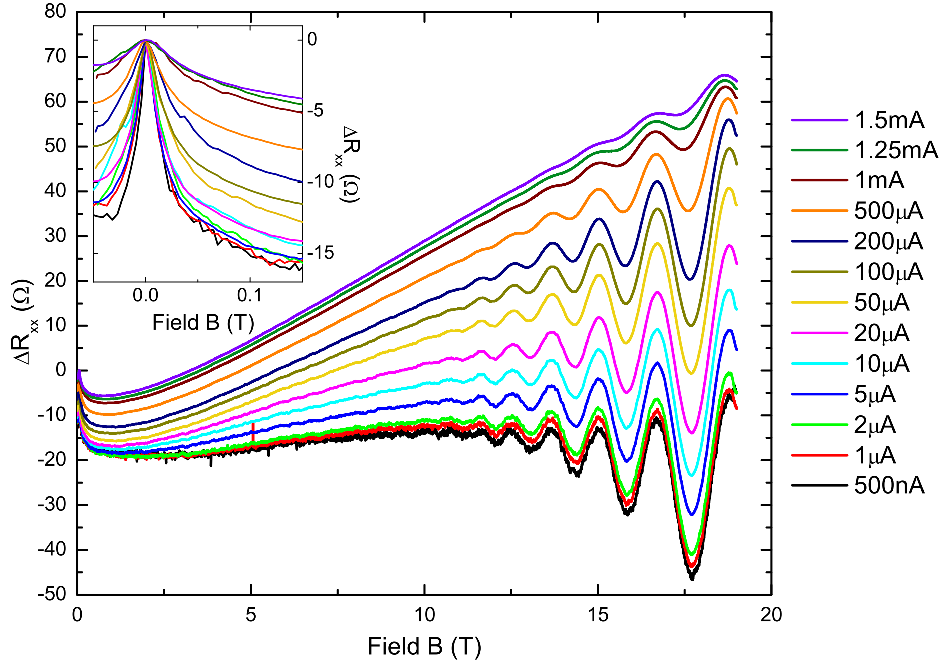

Figure 5.5: R_{xx} for CVD graphene with n = 1.43 x $10^{13}\,cm^{-2}$. All traces taken at 1.5K with the current varied from 500nA up to 1.5mA. Traces are shifted such that the WL peak is at 0Ω. The inset shows the WL peak around B = 0T.

Having established the validity of the SdH method at these carrier densities, the energy loss rates were determined as a function of carrier temperature by measuring the amplitudes of the SdH oscillations as a function of current (Fig. 5.5). Comparing the amplitudes to the undamped value, taken at low current, and using Eq. (5.1), the carrier temperature for each trace is determined. The associated energy loss rate per carrier is calculated using

$$E_{loss} = \frac{I^2 R_{xx}}{nA}, \tag{5.6}$$

where R_{xx} is the sample resistance, n is the carrier density, and A is the device area.

5.3.2 Weak-localization

For some samples, however, the SdH method for extracting energy loss rates could not be applied, most notably for the lower carrier density SiC/G devices, where the carrier densities are too low to support a series of sinusoidal SdH oscillations (Fig. 5.1). SiC/G samples do, however, have prominent WL peaks.

The magnitude of the WL peak is known to be strongly damped by increasing temperature [20, 21]. Energy loss rates have previously been measured as a function of carrier temperature from WL peaks for several other materials [22–25]. In GaAs [23] good agreement was found between the values for electron temperature deduced from the WL peak and SdH oscillations at low fields (∼0.5T) up to ∼4K. Similarly excellent agreement was found for the two methods in SiGe [22] but could only be studied for electron temperatures up to 1.1K. In our work the WL peak persists up to temperatures of almost 100K allowing a much more extensive range of parameters to be studied. Previous work in graphene [26], however, was not able to determine energy loss rates

from the damping of the WL peak.

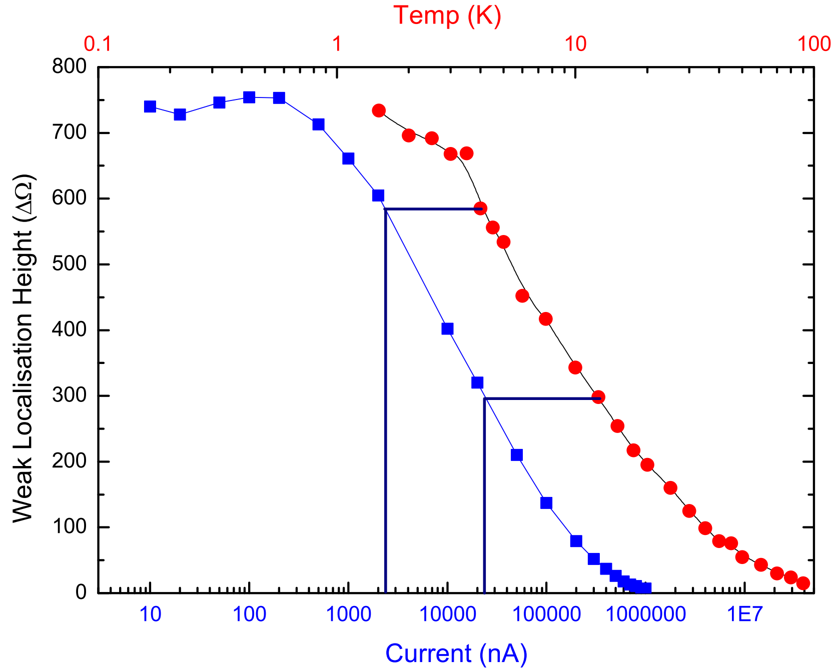

Figure 5.6: An example set of data displaying the matching of the height of the WL peak as a function of current (squares) and temperature (circles), from a SiC sample with n = 4.13 x 10^{11} cm^{-2}.

We determine the energy loss rates by comparison of the current and temperature dependence of the WL peak. The magnitudes of the peaks are measured by taking the difference of R_{xx} between 0T and a fixed small field, sufficient to entirely suppress the WL behaviour. A best-fit interpolated curve is plotted of the temperature dependent amplitude measured at low current which allows us to assign a carrier temperature to each current by finding points of equivalently damped amplitude (Fig. 5.6).

It is worth emphasizing that for the above analysis to be correct, the effects of raising both the carrier and lattice temperature (T_L) need to be equivalent. The magnitude of the WL peak depends primarily on the inelastic scattering time τ_φ, and so for this equivalence to be the case τ_φ must only depend on the carrier temperature, and be

independent of the lattice temperature. This has been verified by Ki *et al.* [27] by measuring the effect on τ_φ of changes to the carrier density at temperatures up to 20K. The inelastic scattering, τ_φ, in graphene was shown to depend on Coulomb interactions and Nyquist scattering, both of which vary with carrier temperature only. This can be qualitatively seen by the similar functional dependence upon current and temperature, shown in Fig. 5.6.

5.3.3 Comparison of the energy loss rate techniques

Sample Type	Carrier Density (cm^{-2})	SdH α ($W\,K^{-4}$/ carrier)	WL α ($W\,K^{-4}$/ carrier)	αSdH / αWL
CVD	$1.62 \cdot 10^{13}$	$2.4 \cdot 10^{-18}$	$3.8 \cdot 10^{-18}$	0.63
CVD	$1.43 \cdot 10^{13}$	$2.0 \cdot 10^{-18}$	$3.0 \cdot 10^{-18}$	0.67
CVD	$8.16 \cdot 10^{12}$	$2.2 \cdot 10^{-18}$	$3.7 \cdot 10^{-18}$	0.59
Epitaxial	$1.63 \cdot 10^{12}$	$2.1 \cdot 10^{-18}$	$3.7 \cdot 10^{-18}$	0.57
			Average =	0.62

Table 5.2: The α values $P = \alpha(T_e^4 - T_L^4)$ for CVD and SiC/G samples measured by the SdH and WL methods.

The energy loss rates as measured by both techniques up to 90 K are shown in Fig. 5.7 for CVD and epitaxial graphene. Only the SdH method could be used on the exfoliated graphene, which does not exhibit large WL peaks [28]. There is a systematic difference between the two methods with the SdH techique giving energy loss rates ∼40% lower (Table 5.2). This is in contrast to GaAs [23] and SiGe [22] where good agreement between the two methods was found when SdH oscillations below 1 T were analysed. We attribute this to a magnetic-field suppression of the energy loss rate, as the WL method measures the energy loss rate near 0 T, whereas the relatively low mobilities in most graphene samples require the SdH method to make measurements at much higher fields, typically 10 T to 18 T in our samples, where the Landau quantization energy is 30 to 50 meV and significant changes in the current distribution also occur. Taken together,

these methods allow the measurement of the energy loss rates per carrier as a function of carrier temperature for any graphene sample, and permit a robust comparison to be made between such samples.

5.3.4 Measured energy loss rates

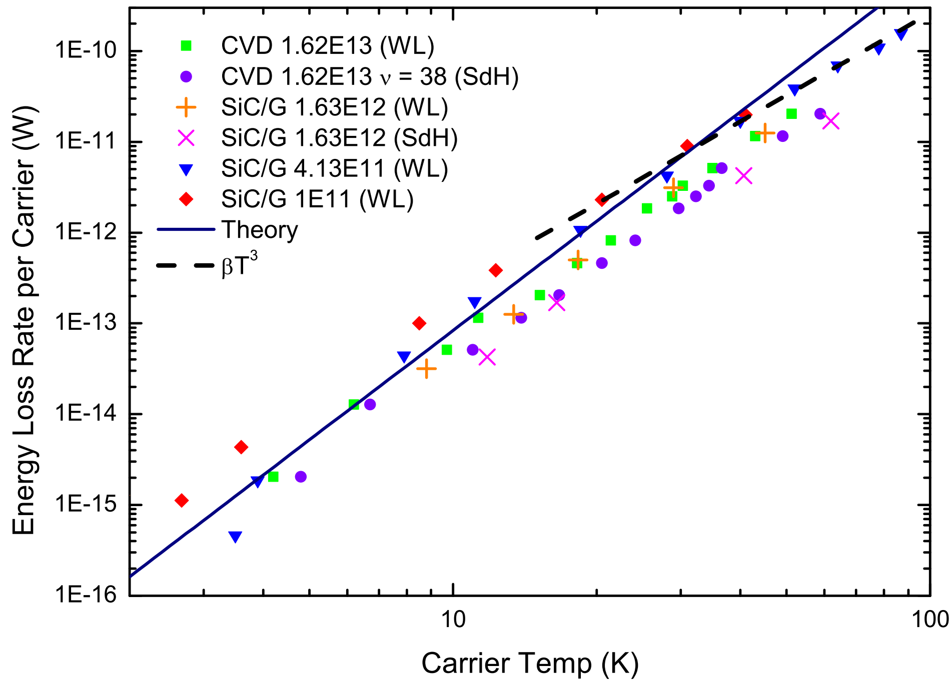

Figure 5.7: Carrier energy loss rate as a function of electron temperature for a representative variety of samples and from the two techniques used. The data follow a similar trend for all samples, with the energy loss rate scaling by approximately T^4. An extrapolated T^4 dependence from low temperature calculations [9] is shown for a carrier density of 4.13 x 10^{11} cm^{-2} and a T^3 dependence is also shown.

Fig. 5.7 demonstrates that there are no significant differences in the systematic behaviour between samples derived from the different production methods. We find that samples produced by all the measured production methods are well fitted to a low temperature, limiting behaviour of $P = \alpha(T_e^4 - T_L^4)$, where α is a scaling constant that is only

weakly carrier density dependent. This can be approximated to the form $P = \alpha(T_e^4)$ when $T_L \ll T_e$. Theoretical predictions of the energy loss rate at low temperatures from Kubakaddi [9] are shown for a carrier density of n = 4.13 x 10^{11} cm^{-2}. These are dominated by deformation potential coupling and are shown to be an excellent fit with a deformation potential of 19 eV. This (T_e^4) power law behaviour is typical for low temperatures below the Bloch-Grüneisen temperature (T_{BG}) as observed for the resistivity in graphene [29]. This is in contrast to some previous theoretical [10] and experimental [8] work which suggested other powers of T.

The value of T_{BG} ($=\hbar v_F k_F / k_B$) for the samples studied is in the range 10-125K (1-160 x 10^{11} cm^{-2}), but, as found previously in GaAs [14], the data show no evidence of approaching a high temperature limit of linear T dependence, even at temperatures significantly above T_{BG}. At the highest temperatures there is, however, some decrease in the energy loss rate, closer to a power law in the region of T^3 or lower, as shown in Chapter 4 (see also [7]) at high T_e.

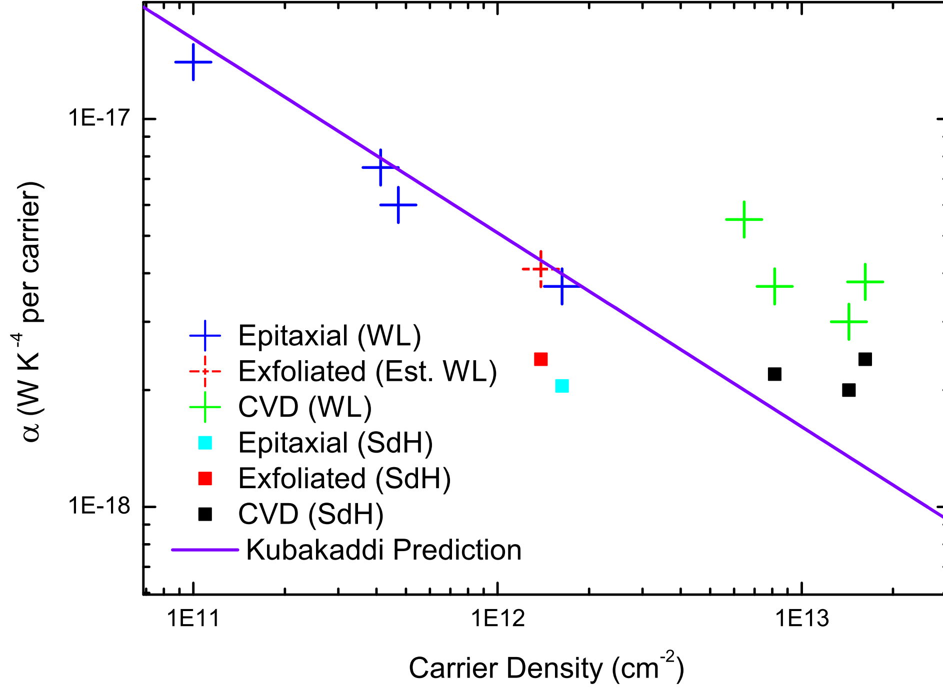

Figure 5.8: The α values as a function of carrier density for the CVD, exfoliated, and epitaxial graphene data deduced from WL, and SdH methods. The point labelled in the key as exfoliated (Est. WL) is estimated from previous SdH results for an exfoliated sample by adjusting the value upwards by 60% to take account of the the measured systematic difference between the two methods (Table 5.2). The solid line on the graph is the theoretical prediction from Kubakaddi [9] using a deformation-potential coupling constant of 19 eV.

Fig. 5.8 shows the fitted α coefficient for data below 30K, plotted against carrier density, for all the measured samples, and, where possible, for multiple measurement techniques. The theoretical predictions [9] of the absolute values are in excellent agreement with experiment for the epitaxial and exfoliated samples and show an $\alpha \propto n^{-\frac{1}{2}}$ dependence on carrier density as predicted. However for CVD samples the energy loss rates appear to be a factor of 2 - 3 larger. Recent theoretical work from Song *et al.* [30] has proposed enhanced energy loss processes in graphene which they term “super-collisions”. These are caused by disorder-assisted, and two-phonon, scattering and are particularly important for higher energy carriers which play a disproportionately large role in the energy loss processes. Our CVD samples contain significant amounts of dis-

order and hence the "supercollision" process could potentially account for the increased energy loss rates of the CVD samples relative to the theoretical predictions [9]. Song *et al.* predict that around T_{BG} this should give a dependence $\propto T^3$, while fitting the higher temperature data for the CVD samples in Fig. 5.7 gives P $\propto T^{3.5}$, suggesting that this process is beginning to contribute to the energy loss rate.

5.4 Conclusions

We have performed an extensive comparison of the transport properties of graphene produced by the three most common production methods. The energy loss rates per carrier as a function of carrier temperature follow a low temperature limiting T^4 dependence in all cases, with a multiplicative factor that varies weakly with carrier density in good agreement with theory [9] based on deformation potential scattering. The close agreement between epitaxial graphene grown on SiC and exfoliated flakes deposited on SiO_2 suggest that the substrate plays very little role in determining the energy loss rates. An enhanced energy loss rate is observed in CVD samples which may be attributable to "supercollisions" [30] enhanced by the presence of increased disorder which may be beneficial for electronic applications of graphene. We have also established that energy loss rates can be measured over a wide temperature range using the WL correspondence method, and correlate well with the conventional SdH method, but that the values deduced at high fields (10-18 T) are suppressed by $\sim$40% relative to the low field values. Finally, we have also measured the Fermi velocity in CVD graphene, at a Fermi energy of 478 meV, to be 1.08 x 10^6 ms^{-1}. This value is in agreement with previous measurements for graphene with a Fermi energy significantly closer to the Dirac point.

Bibliography

[1] D. a. Siegel, C.-H. Park, C. Hwang, J. Deslippe, A. V. Fedorov, S. G. Louie, and A. Lanzara, “bibfield journal “bibinfo journal Proc. Natl. Acad. Sci. USA“ “textbf “bibinfo volume 108,“ “bibinfo pages 11365 (“bibinfo year 2011).

[2] K. S. Novoselov, A. K. Geim, S. V. Morozov, D. Jiang, Y. Zhang, S. V. Dubonos, I. V. Grigorieva, and A. A. Firsov, Science **306**, 666 (2004).

[3] R. Van Noorden, Nature **483**, S32 (2012).

[4] K. Bolotin, K. Sikes, Z. Jiang, M. Klima, G. Fudenberg, J. Hone, P. Kim, and H. Stormer, Solid State Commun. **146**, 351 (2008).

[5] A. Tzalenchuk, S. Lara-Avila, A. Kalaboukhov, S. Paolillo, M. Syväjärvi, R. Yakimova, O. Kazakova, T. J. B. M. Janssen, V. Fal’ko, and S. Kubatkin, Nat. Nanotech. **5**, 186 (2010).

[6] J. Yan, M.-H. Kim, J. A. Elle, A. B. Sushkov, G. S. Jenkins, H. M. Milchberg, M. S. Fuhrer, and H. D. Drew, Nat. Nanotechnol. **7**, 472 (2012).

[7] A. M. R. Baker, J. A. Alexander-Webber, T. Altebaeumer, and R. J. Nicholas, Phys. Rev. B **85**, 115403 (2012).

[8] Z. Tan, C. Tan, L. Ma, G. T. Liu, L. Lu, and C. L. Yang, Phys. Rev. B **84**, 115429 (2011).

[9] S. S. Kubakaddi, Phys. Rev. B **79**, 075417 (2009).

[10] W.-K. Tse and S. Das Sarma, Phys. Rev. B **79**, 235406 (2009).

[11] S. Chen, Q. Wu, C. Mishra, J. Kang, H. Zhang, K. Cho, W. Cai, A. A. Balandin, and R. S. Ruoff, Nat. Mater. **11**, 203 (2012).

[12] T. J. B. M. Janssen, A. Tzalenchuk, R. Yakimova, S. Kubatkin, S. Lara-Avila, S. Kopylov, and V. I. Fal’ko, Phys. Rev. B **83**, 233402 (2011).

[13] S. Lara-Avila, K. Moth-Poulsen, R. Yakimova, T. Bjornholm, V. Fal'ko, A. Tzalenchuk, and S. Kubatkin, Adv. Mater. **23**, 878 (2011).

[14] D. R. Leadley, R. J. Nicholas, J. J. Harris, and C. T. Foxon, Semicond. Sci. Technol. **4**, 879 (1989).

[15] T. Ando, J. Phys. Soc. Japan **37**, 1233 (1974).

[16] G. Stöger, G. Brunthaler, G. Bauer, K. Ismail, B. S. Meyerson, J. Lutz, and F. Kuchar, Phys. Rev. B **49**, 10417 (1994).

[17] Y. Ma, R. Fletcher, E. Zaremba, M. D'Iorio, C. T. Foxon, and J. J. Harris, Phys. Rev. B **43**, 9033 (1991).

[18] R. Deacon, K.-C. Chuang, R. J. Nicholas, K. S. Novoselov, and A. K. Geim, Phys. Rev. B **76**, 081406 (2007).

[19] D. L. Miller, K. D. Kubista, G. M. Rutter, M. Ruan, W. A. de Heer, P. N. First, and J. A. Stroscio, Science **324**, 924 (2009).

[20] H. Cao, Q. Yu, L. A. Jauregui, J. Tian, W. Wu, Z. Liu, R. Jalilian, D. K. Benjamin, Z. Jiang, J. Bao, S. S. Pei, and Y. P. Chen, Appl. Phys. Lett. **96**, 122106 (2010).

[21] S. Lara-Avila, A. Tzalenchuk, S. Kubatkin, R. Yakimova, T. J. B. M. Janssen, K. Cedergren, T. Bergsten, and V. Fal'ko, Phys. Rev. Lett. **107**, 166602 (2011).

[22] R. Leturcq, D. L'Hôte, R. Tourbot, V. Senz, U. Gennser, T. Ihn, K. Ensslin, G. Dehlinger, and D. Grützmacher, Europhys. Lett. **61**, 499 (2003).

[23] R. Fletcher, J. J. Harris, C. T. Foxon, and R. Stoner, Phys. Rev. B **45**, 6659 (1992).

[24] M. Gershenson, Y. Khavin, D. Reuter, P. Schafmeister, and A. Wieck, Phys. Rev. Lett. **85**, 1718 (2000).

[25] G. Stöger, G. Brunthaler, G. Bauer, K. Ismail, B. S. Meyerson, J. Lutz, and F. Kuchar, Semicond. Sci. Technol. **9**, 765 (1994).

[26] S. Lee, N. Wijesinghe, C. Diaz-Pinto, and H. Peng, Phys. Rev. B **82**, 045411 (2010).

[27] D. K. Ki, D. Jeong, J. H. Choi, H. J. Lee, and K. S. Park, Phys. Rev. B **78**, 125409 (2008).

[28] S. V. Morozov, K. S. Novoselov, M. I. Katsnelson, F. Schedin, L. A. Ponomarenko, D. Jiang, and A. K. Geim, Phys. Rev. Lett. **97**, 016801 (2006).

[29] D. Efetov and P. Kim, Phys. Rev. Lett. **105**, 256805 (2010).

[30] J. C. W. Song, M. Y. Reizer, and L. S. Levitov, ArXiv [**cond-mat.mes-hall**], arXiv:1111.4678v2 (2012).

Chapter 6

Weak Localization Scattering Lengths in Epitaxial, and CVD Graphene

---

Fits to weak localization are performed for devices with carrier densities ranging from 1 x $10^{11}\,\mathrm{cm}^{-2}$ to 1.43 x $10^{13}\,\mathrm{cm}^{-2}$. Weak localization on devices produced by epitaxial growth onto SiC and CVD growth on thin metal film are analysed and shown to be well fitted by theory. We demonstrate that the previously reported saturation of measured L_φ in the literature is caused by hot-electron effects, and to avoid such effects currents as low as 0.01 nA are required in small devices. Finally we analyse trends in L_φ (dephasing length), L_i (elastic intervalley scattering length), and L_* (total scattering length) with carrier density. We find no significant trend for L_φ, a decreasing trend with carrier density for L_i just beyond a large standard error, and a $n^{-\frac{1}{4}}$ trend for L_* with a small standard error.

6.1 Introduction

Since its discovery eight years ago, graphene has proved of great interest both for its huge range of potential applications, from enhancing the strength of composite materials [1], to high-speed analogue electronics [2]; and for its impressive range of physical properties, including an anomalous integer quantum Hall effect [3], quantized opacity [4], and its two-dimensionality [3]. Amongst other properties it shows a greatly enhanced weak (anti)localization effect [3], which is the principal topic of this chapter.

The nature of weak (anti)localization in graphene has attracted a significant amount of controversy [5]. It was originally predicted that the effect would be entirely of the weak antilocalization type due to the existence of a Berry phase in graphene. Early results, however, failed to show such behaviour [5]. Subsequently, it was realized that this could be resolved by the addition of further scattering terms which break chirality, particularly elastic intervalley scattering [6].

The purpose of this chapter is the fitting of scattering lengths using the theory of McCann *et al.* [6] for a wide range of different graphene samples. The fittings are used to demonstrate the validity of this method for devices with carrier densities ranging from 1 x $10^{11}\,\mathrm{cm}^{-2}$ to 1.43 x $10^{13}\,\mathrm{cm}^{-2}$. Devices are analysed from graphene produced by epitaxial growth on SiC [7], and chemical vapour deposition (CVD) onto thin metal films [8]. The results are compared with those obtained from the literature [9–12] and together are used to measure trends in the scattering lengths with carrier density.

We also demonstrate that the saturation of the dephasing length with decreasing temperature [10, 11, 13] reported in some cases is an experimental artefact caused by hot-electron effects in graphene. Hot-electron effects are explored in greater detail in Chapters 4 & 5 (see also [14, 15]). The currents required to avoid this effect are calculated

and are demonstrated to be as low as 0.01 nA for small devices.

6.2 Methodology and Theoretical Background

A more detailed discussion of the theoretical background to weak (anti)localization can be found in section 2.2.

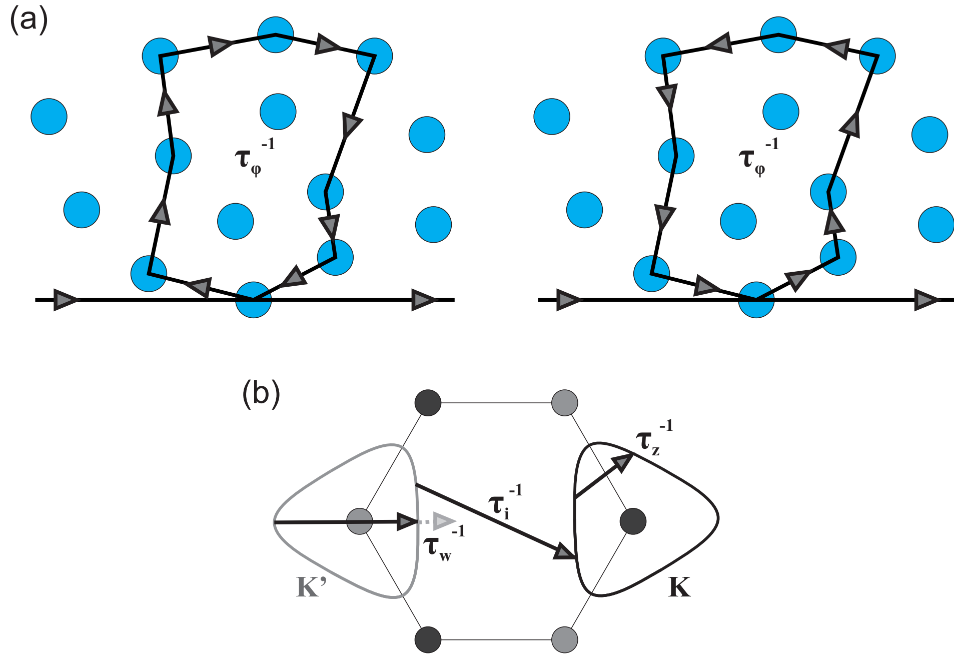

Figure 6.1: Illustration of the scattering processes which contribute to weak (anti)localization. (a) Two example scattering paths, identical except for the direction of travel around the loop. The dephasing rate, τ_φ^{-1}, controls the maximum size of such loops due to the need for phase coherence to produce an interference effect. (b) The two rounded triangles centred on the two inequivalent Dirac points, K, K' are shown for a small Fermi energy such that trigonal warping is clearly apparent. Three scattering terms, and how they contribute, are superimposed on this Fermi surface: τ_i^{-1}, the elastic intervalley scattering rate, τ_w^{-1}, the elastic intravalley trigonal warping scattering term and τ_z^{-1} the elastic intravalley chirality breaking scattering term.

Hall bar devices were produced using graphene derived from the epitaxial and CVD

fabrication methods. The devices were produced using e-beam lithography and oxygen plasma etching. The epitaxial graphene was grown on the Si-terminated face of SiC [7], with contacts made using large area titanium-gold contacting. Photochemical gating was used to control the carrier density on the epitaxial devices due to the impossibility of conventional backgating through SiC [16]. CVD graphene was grown on thin-film copper, subsequently transferred to Si/SiO_2, and contacts were made using chrome-gold tracks/bondpads followed by gold-only final contacting, as described in Chapter 4 (see also [14]). Various sizes of large-area Hall bar were produced; dimensions were typically 64 x 16 μm^2 for the CVD devices, and 160 x 35 μm^2 for the epitaxial devices.

Weak (anti)localization is a quantum interference effect which occurs at low temperatures in disordered systems where electrons can remain coherent over sufficiently long distances [17]. Fig. 6.1 shows four scattering terms which contribute to this process. Fig. 6.1 (a) shows τ_φ, the dephasing rate due to inelastic scattering [6]. Fig. 6.1 (b) shows the three other main scattering terms [18]: τ_i, the elastic intervalley scattering rate which comes from atomically sharp scatterers and scattering from the edges of the device, τ_w, the elastic intravalley trigonal warping scattering term, and finally τ_z, the elastic intravalley chirality breaking scattering term which comes from dislocations or other topological defects. There is a further tau, τ_* which was originally defined [6] as $\tau_*^{-1} \equiv \tau_w^{-1} + \tau_z^{-1} + \tau_i^{-1}$. This definition is used in this thesis; however, it is worth pointing out that in the literature an alternate definition is often used, where $\tau_*^{-1} = \tau_w^{-1} + \tau_z^{-1}$. Care must therefore be taken when dealing with τ_*^{-1} to account for these different definitions.

Fig. 6.1 (a) displays two self-intersecting scattering paths. These two paths are identical except for the direction of travel around the loop. Interference between such loops is the origin of the weak (anti)localization effect. If these paths constructively

interfere, such loops are more common than would be expected classically, resulting in an increase in resistance known as weak localization. The converse, the destructive interference case, is called weak antilocalization. Due to the need to maintain phase coherence for an interference effect to occur, τ_φ acts to control the maximum size of such loops, and hence the magnitude of the weak (anti)localization effect.

Whether we are operating in a weak localization regime, or a weak antilocalization regime, depends on the phase the carriers pick up while traversing such a path. Because of the existence of a Berry phase in monolayer graphene [3], the two trajectories are expected to gain a phase difference of π, leading to destructive interference, and hence weak antilocalization [19]. However, in the presence of significant elastic intervalley scattering (τ_i), weak localization can be restored. The reason for this is that chirality is reversed between the two valleys [20]; hence trajectories involving intervalley scattering allow for zero phase difference between two self-intersecting paths which leads to constructive interference and hence weak localization.

The weak (anti)localization effect can be destroyed by increasing either the magnetic field or temperature to a sufficient value. Increased magnetic fields add a random relative phase to the carriers as they traverse curved paths, causing the interference effect to be averaged away [17]. Increased temperature has the effect of decreasing τ_φ, which reduces the magnitude of both types of localization effect, Eq. (6.2).

This chapter makes use of the main result from McCann *et al.* [6] to produce fits of the resistivity as a function of magnetic field, B, to the measured weak (anti)localization,

$$\Delta\rho(B) = -\frac{e^2\rho^2}{\pi h}\left(F\left(\frac{\tau_B^{-1}}{\tau_\varphi^{-1}}\right) - F\left(\frac{\tau_B^{-1}}{\tau_\varphi^{-1} + 2\tau_i^{-1}}\right) - 2F\left(\frac{\tau_B^{-1}}{\tau_\varphi^{-1} + \tau_*^{-1}}\right)\right), \qquad (6.1)$$

where $F(z) = \ln z + \psi\left(\frac{1}{2} + \frac{1}{z}\right)$, ψ is the digamma function, $\tau_B^{-1} = \frac{4eDB}{\hbar}$, and D, the diffusion coefficient $= \frac{1}{2}v_F^2\tau_{tr}$, where τ_{tr} is the transport time. At small magnetic fields, where $z \ll 1$, we can approximate $F(z) \approx \frac{z^2}{24}$. Using this we can simplify Eq. (6.1) for small fields as,

$$\Delta\rho(B) = -\frac{e^2\rho^2}{24\pi h}\left(\frac{4eDB\tau_\varphi}{\hbar}\right)^2\left(1 - \frac{1}{\left(1+2\frac{\tau_\varphi}{\tau_i}\right)^2} - \frac{2}{\left(1+\frac{\tau_\varphi}{\tau_*}\right)^2}\right). \tag{6.2}$$

From this equation it is clear how variations in τ_φ control the magnitude of the weak (anti)localization. It is also clear how significant intervalley scattering, τ_i, is required to produce a positive resistivity correction, i.e. weak localization. In practice, significant intervalley scattering is found in most samples, and therefore, weak localization is far more commonly found than weak antilocalization [21].

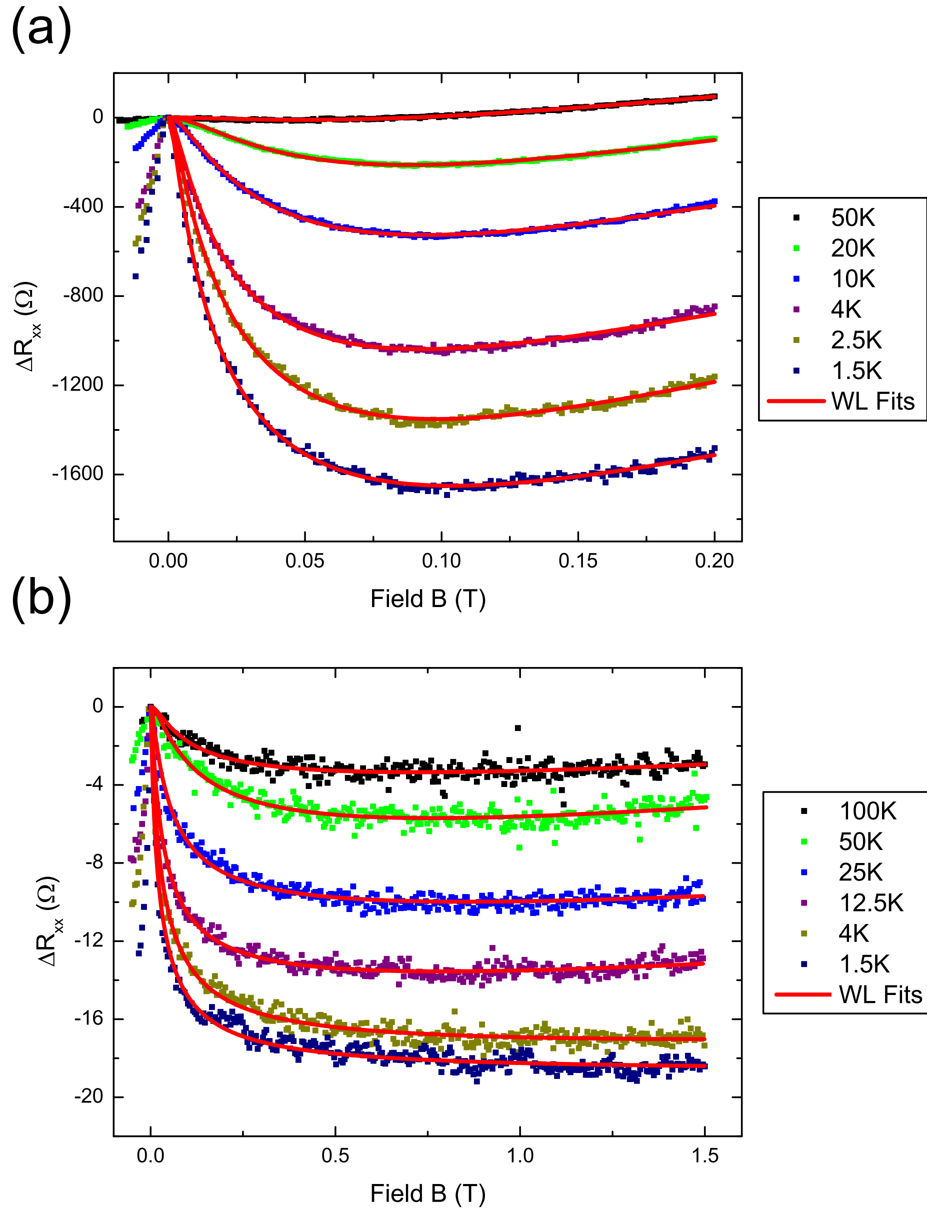

Figure 6.2: Plots showing weak localization fits using the theory of McCann *et al.* [6] from the two extremes of carrier density for the measured samples. The two plots highlight the dramatically different range in field and resistance that weak localization can occur over. (a) Epitaxially grown on SiC [7], $n = 1$ x $10^{11}\,\mathrm{cm}^{-2}$, exhibiting a low-temperature weak localization magnitude of $1.6\,\mathrm{k}\Omega$, and a minimum in R_{xx} at 0.1 T. (b) Grown by CVD onto copper [8], $n = 1.43$ x $10^{13}\,\mathrm{cm}^{-2}$, exhibiting a low-temperature weak localization magnitude of $18\,\Omega$, and a minimum in R_{xx} in excess of 1.5 T for low-temperatures.

Fig. 6.2 shows data from the extremes of carrier density of the measured samples. The samples are found to be very well fitted by the McCann theory [6], despite the two samples having very different magnitudes, shape, and spread over field. These fits are significantly better than many in the literature. To attain the best possible fits, several factors need to be taken into account. First, it is necessary to take good quality data, which requires sufficiently slow magnetic field sweeps such that many data points are recorded and that the effect of any lags in the system or measurement equipment are minimized. A second factor is that it is ideal if the field sweeps can be arranged such that the system sweeps through zero-field, so that the whole of the weak (anti)localization peak is well imaged. This is particularly important for the weak (anti)localization effect since there is a very sharp drop-off in the effect with magnetic field. For the fitting procedure itself, extreme care must be taken to avoid landing in local minima of the parameter space, especially when τ_* and/or τ_i are very short. One final factor which is covered in the maximum currents section (Sec. 6.3.2) is the importance of using sufficiently small currents, especially for studies which use low temperatures.

6.3 Results

6.3.1 Scattering lengths

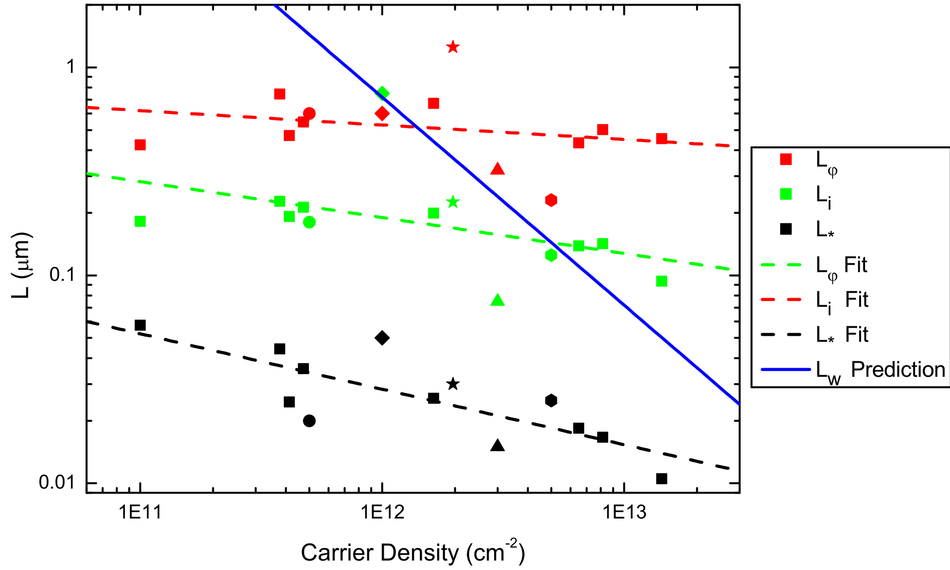

Figure 6.3: Scattering lengths as a function of carrier density. Squares denote our own data, which was all collected at 1.5 K. Circles denote data from Lara-Avila *et al.* [9]. Diamonds denote data from Tikhoneko *et al.* [10]. Stars denote data from Ki *et al.* [11]. Hexagons denote data from Jauregui *et al.* [12]. All data collected from the literature as close to 1.5 K as possible. L_w Prediction is the prediction from McCann *et al.* [6]

Fig. 6.3 shows the extracted scattering lengths, from our data and from the literature [9–12]. Scattering times were extracted using Eq. (6.1) and converted to scattering lengths using, $L_{\varphi,i,*} = \sqrt{\tau_{\varphi,i,*}D}$. Care was taken to extract all values for as close as possible to the same temperature, in this case 1.5 K. This is done since L_φ in particular is known to vary strongly with temperature [9–12]. Fits to the data are made using a simple power law, Bn^A, the results of which are shown in Table 6.1.

To within the standard error we find no variation with carrier density for the phase coherence length (L_φ). Previous work has typically found similar values for L_φ of around

Scattering Length	Exponent (A)	Exponent Standard Error	Multiplicative Constant (B)
L_φ	-0.069	± 0.082	$3.59{\cdot}10^{-6}$ m
L_i	-0.173	± 0.101	$2.25{\cdot}10^{-5}$ m
L_*	-0.267	± 0.064	$4.47{\cdot}10^{-5}$ m

Table 6.1: Multiplicative constant and exponents of the fits to the data in Fig. 6.3 of the form Bn^A, where n is the carrier density in carriers per cm^2.

0.6 μm [9–12]. In Ki *et al.* [11], there has been some previous work carried out on the carrier density dependence by using a single sample with a backgate. In their work they found a superlinear increase of L_φ with carrier density. These devices, however, were very small at 6 x 1 μm^2 and were probably effected by boundary scattering. More indirectly, temperature studies have also been carried out on L_φ, the modelling of which could in principle be used to predict a carrier density dependence. In Ki *et al.* [11], the scattering length's behaviour is modelled using two electron-electron interaction terms, a direct Coulomb term and a Nyquist scattering term. These terms do have a carrier density dependence, however, the fitting parameters were found to vary with carrier density. Lara-Avila *et al.* [9] use an alternative model and find their data to be well modelled by the addition of a electron spin-flip scattering term. This term is due to spin-flip scattering from the localized magnetic moment of spin-carrying defects. Unfortunately, since this term is highly dependent on the sample quality and the nature of any impurities, this suggests that the spin-flip effect could substantially mask any underlying trend in the phase coherence length with carrier density.

For the elastic intervalley scattering term, L_i, we find a weak trend with carrier density with a negative exponent of -0.173. Previous temperature [9, 11] and backgate studies [11] found no strong variation of L_i with either temperature or carrier density. Given that L_i is due to atomically sharp scatterers and device-edge scattering, it would be expected to be highly dependent on the device characteristics. However, the level

of atomically sharp scatterers might be expected to increase with the ungated carrier density of samples. In particular, for the data presented here, the highest ungated carrier densities are found for CVD graphene devices which are associated with high levels of polycrystallinity. This implies a large number of atomically sharp scatterers, and hence could account for the measured carrier density dependence.

The strongest trend, with an exponent of -0.267, and smallest standard error ($\pm$0.064) is found for L_*, the sum of all the sublattice-symmetry-breaking perturbations. For all samples in Fig. 6.3, $L_i \gg L_*$ and hence L_* will be predominantly made up from L_w, the elastic intravalley trigonal warping scattering term, and L_z, which allows for other chirality breaking elastic intravalley processes. We would expect the trigonal warping term to increase with carrier density, since the degree of trigonal warping is dependent on the Fermi energy. The L_z term is expected to be relatively independent of carrier density due to its origin from topological defects [18]. McCann *et al.* [6] produce the following prediction of how L_w is expected to vary with carrier density,

$$L_w^{-2} = \frac{\tau_w^{-1}}{D} = \frac{\tau_{tr}}{D}\left(\frac{\mu E_F^2}{\hbar v_F^2}\right)^2 \propto n^2. \tag{6.3}$$

where μ, the structure constant $= \frac{\gamma_0 a^2}{8\hbar^2}$, E_F is the Fermi energy, and v_F is the Fermi velocity. This equation predicts that L_w should be proportional to $\frac{1}{n}$, and is shown on Fig. 6.3 as a solid blue line. For the region studied we find a much slower variation with n of approx $n^{\frac{1}{4}}$. This suggests we do not measure in the region where the trigonal warping scattering term, L_w, is the dominant component of L_*, and that L_w should become the dominant component above around 8.2 x $10^{13}\,\mathrm{cm}^{-2}$.

6.3.2 Maximum currents

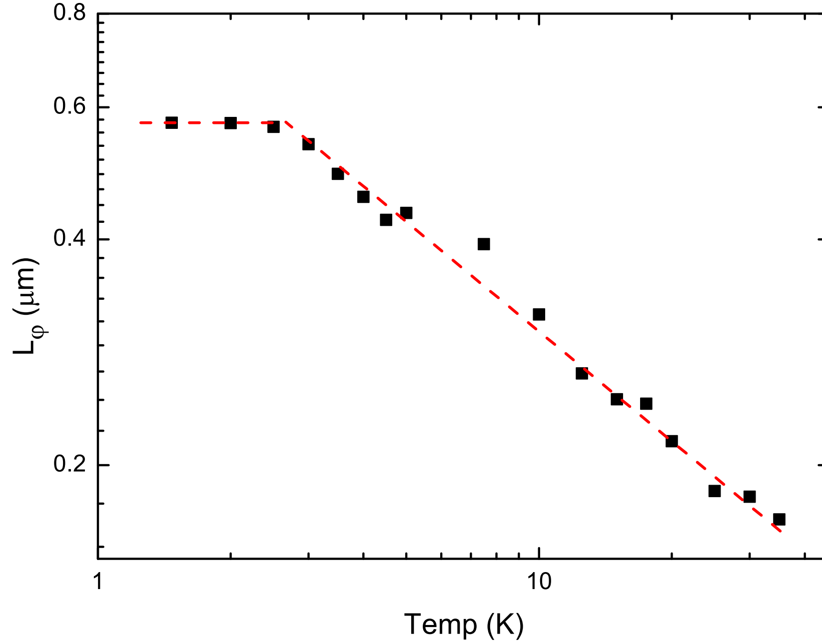

Figure 6.4: L_φ data for for an epitaxial sample with a carrier density of 4.72 x 10^{11} cm^{-2}, a size of 160 x 35 μm^2, and a sample resistance at zero field of 8.2 kΩ. All data was measured with a current of 500 nA. Despite the comparatively large size of the sample and fairly low current used, the effect of "hot-carriers" is clearly visible preventing the temperature of the carriers from being reduced below 2 K.

In this section the importance of using sufficiently low currents is demonstrated, together with how the use of too large currents may explain the observations of a "saturation" in L_φ sometimes found in the literature. Because of the very large optical phonon energies in graphene [22], the dominant cooling mechanism for carriers in graphene at low temperatures comes from acoustic phonons, Chapter 4 (see also [14]). The acoustic phonon cooling in graphene is a fairly weak mechanism which allows carriers to attain temperatures far in excess of that of the lattice, Chapters 4 & 5 (see also [14, 15]), and at low temperatures in the Bloch-Grüneisen limit this process is strongly temperature dependent. This "hot-carrier" effect can be described using the theory of Kubakaddi

[23]. Using this theory, we can calculate the effective minimum carrier temperature, $T_{e,min}$, that can be obtained for a given device for each current. Kubakaddi presents the relation for the energy loss rate per carrier,

$$F(T) = \alpha(T_e^4 - T_l^4), \tag{6.4}$$

where T_e is the carrier temperature, and T_L is the lattice temperature. For a given current and sample resistance R_{xx}, this can be equated to the power input per carrier from the current as

$$\alpha(T_e^4 - T_l^4) = \frac{I^2 R_{xx}}{nA}, \tag{6.5}$$

where n is the carrier density, and A is the sample area. The coefficient α is calculated using the relation

$$\alpha = \frac{D^2 E_F k_B^4 3! \zeta(4)}{n\pi^2 \rho \hbar^5 v_s^3 v_f^3}, \tag{6.6}$$

where ζ is the Riemann zeta function, ρ is the sample density, and v_s is the sound velocity. This can be rearranged to give the effective minimum carrier temperature,

$$T_{e,min} = \sqrt[4]{\frac{I^2 R_{xx}}{\alpha n A} + T_L^4}, \tag{6.7}$$

Using the numerical values suggested by Kubakaddi [23] we calculate $\alpha = 5.36 \text{ x } 10^{-18}$ W K^{-4} / $\sqrt{n}$, where n is in / 10^{12} cm^{-2}.

Fig. 6.4 shows data from one of our epitaxial samples which exhibits a saturation in

the measured value of L_φ with decreasing temperature. The sample has a carrier density of $4.72 \times 10^{11}\,\mathrm{cm}^{-2}$, a size of $160 \times 35\,\mu\mathrm{m}^2$ and a sample resistance of $8.2\,\mathrm{k}\Omega$. All the data for the graph was collected with a current of 500 nA. Using Eq. (6.7) we calculate $T_{e,min}$ for the sample as 1.97 K. This value corresponds well to the temperature of the measured onset of the saturation regime presented in the figure.

When previously encountered, this saturation in measured L_φ has been attributed variously to magnetic impurities [11], electron-hole puddles reducing the effective conducting area [11], and limits imposed directly from the sample size [10]. We believe the above hot-carrier explanation is sufficient to give a full account for the behaviour in these previous studies. Giving further weight to the validity of the hot-carrier explanation, Lara-Avila *et al.* [9] measured significant changes in L_φ below 100 mK, by using a large area device and a current of 50 pA for which Eq. (6.7) predicts $T_e \sim 20\,\mathrm{mK}$.

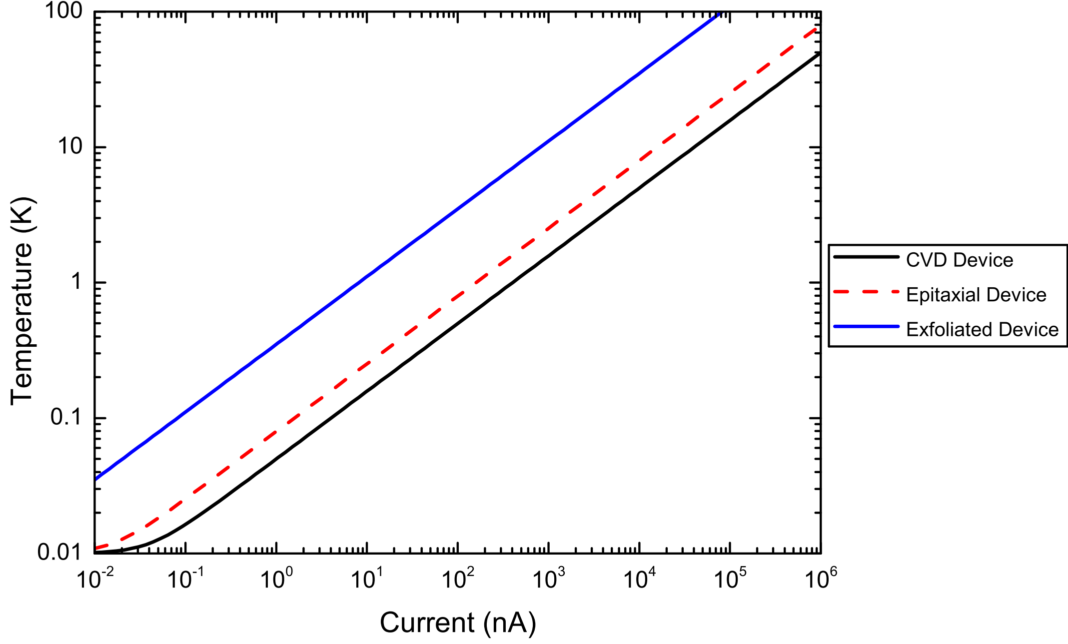

Figure 6.5: The figure presents the minimum carrier temperatures obtainable for a given current, for three different experimental setups, calculated for a lattice temperature, T_L of 10 mK. The epitaxial device is the device showed in Fig. 6.4 (n = 4.72 x 10^{11} cm^{-2}, A = 160 x 35 μm^2, R_{xx} = 8.2 kΩ). The CVD device is the device in Fig. 6.2 (b) (n = 1.43 x 10^{13} cm^{-2}, A = 64 x 16 μm^2, R_{xx} = 1.3 kΩ). The final exfoliated device is for a typical small device similar to devices commonly used in the literature (n = 1 x 10^{12} cm^{-2}, A = 5 x 1 μm^2, R_{xx} = 4 kΩ).

By way of illustration we calculate the currents required to achieve a given carrier temperature for three different examples of typical samples used here and in the literature which we present in Fig. 6.5. The epitaxial device in the figure is the one from Fig. 6.4, the CVD device is the one from Fig. 6.2 (b), and the third, exfoliated graphene device is a typical device similar to many of those used in the literature of dimensions 5 x 1 μm^2. It is striking, and worth emphasizing, that for this device to attain a carrier temperature of 100 mK, it requires maximum currents of < 0.1 nA.

6.4 Conclusions

In this chapter we demonstrate that the theory of McCann *et al.* [6] can be applied to produce high quality fits to weak-localization for devices with carrier densities from 1 x $10^{11}\,\mathrm{cm}^{-2}$ to 1.43 x $10^{13}\,\mathrm{cm}^{-2}$ using graphene produced by both the epitaxial and CVD methods. We have shown that the previously measured saturation in L_φ is due to hot-electron effects from using too large currents and that currents may need to be as low as 0.01 nA to measure at dilution fridge temperatures in small devices. Further, we have investigated trends in carrier density for L_φ, L_i, and L_*. We find no evidence of a trend for L_φ. We do find evidence for a weak decreasing trend with carrier density for L_i, though we acknowledge this could be due to a coincidental increase in disorder with carrier density. Finally, we find strong evidence of a decreasing trend in L_* with carrier density of approximately $n^{-\frac{1}{4}}$.

Bibliography

[1] S. Stankovich, D. a. Dikin, G. H. B. Dommett, K. M. Kohlhaas, E. J. Zimney, E. a. Stach, R. D. Piner, S. T. Nguyen, and R. S. Ruoff, Nature **442**, 282 (2006).

[2] K. Bourzac, Nature **483**, S34 (2012).

[3] K. S. Novoselov, A. K. Geim, S. V. Morozov, D. Jiang, M. I. Katsnelson, I. V. Grigorieva, S. V. Dubonos, and A. A. Firsov, Nature **438**, 197 (2005).

[4] R. R. Nair, P. Blake, A. N. Grigorenko, K. S. Novoselov, T. J. Booth, T. Stauber, N. M. R. Peres, and A. K. Geim, Science **320**, 1308 (2008).

[5] A. K. Geim and K. S. Novoselov, Nat. Mater. **6**, 183 (2007).

[6] E. McCann, K. Kechedzhi, V. I. Fal'ko, H. Suzuura, T. Ando, and B. L. Altshuler, Phys. Rev. Lett. **97**, 146805 (2006).

[7] T. J. B. M. Janssen, A. Tzalenchuk, R. Yakimova, S. Kubatkin, S. Lara-Avila, S. Kopylov, and V. I. Fal'ko, Phys. Rev. B **83**, 233402 (2011).

[8] S. Chen, Q. Wu, C. Mishra, J. Kang, H. Zhang, K. Cho, W. Cai, A. A. Balandin, and R. S. Ruoff, Nat. Mater. **11**, 203 (2012).

[9] S. Lara-Avila, A. Tzalenchuk, S. Kubatkin, R. Yakimova, T. J. B. M. Janssen, K. Cedergren, T. Bergsten, and V. Fal'ko, Phys. Rev. Lett. **107**, 166602 (2011).

[10] F. V. Tikhonenko, D. W. Horsell, R. V. Gorbachev, and a. K. Savchenko, Phys. Rev. Lett. **100**, 056802 (2008).

[11] D. K. Ki, D. Jeong, J. H. Choi, H. J. Lee, and K. S. Park, Phys. Rev. B **78**, 125409 (2008).

[12] L. A. Jauregui, H. Cao, W. Wu, Q. Yu, and Y. P. Chen, Solid State Commun. **151**, 1100 (2011).

[13] X. Wu, X. Li, Z. Song, C. Berger, and W. A. de Heer, Phys. Rev. Lett. **98**, 136801 (2007).

[14] A. M. R. Baker, J. A. Alexander-Webber, T. Altebaeumer, and R. J. Nicholas, Phys. Rev. B **85**, 115403 (2012).

[15] A. M. R. Baker, J. A. Alexander-Webber, T. Altebaeumer, S. D. McMullan, T. J. B. M. Janssen, A. Tzalenchuk, S. Lara-Avila, S. Kubatkin, R. Yakimova, C.-T. Lin, L.-J. Li, and R. J. Nicholas, Submitted to Phys. Rev. Lett. (2012).

[16] S. Lara-Avila, K. Moth-Poulsen, R. Yakimova, T. Bjornholm, V. Fal'ko, A. Tzalenchuk, and S. Kubatkin, Adv. Mater. **23**, 878 (2011).

[17] A. H. Castro Neto, F. Guinea, N. M. R. Peres, K. S. Novoselov, and A. K. Geim, Rev. Mod. Phys. **81**, 109 (2009).

[18] F. Tikhonenko, D. Horsell, B. Wilkinson, R. Gorbachev, and A. Savchenko, Physica E **40**, 1364 (2008).

[19] D. W. Horsell, F. V. Tikhonenko, R. V. Gorbachev, and A. K. Savchenko, Phil. Trans. R. Soc. A **366**, 245 (2008).

[20] V. I. Fal'ko, K. Kechedzhi, E. McCann, B. Altshuler, H. Suzuura, and T. Ando, Solid State Commun. **143**, 33 (2007).

[21] F. V. Tikhonenko, A. A. Kozikov, A. K. Savchenko, and R. V. Gorbachev, Phys. Rev. Lett. **103**, 226801 (2009).

[22] J. Yan, Y. Zhang, P. Kim, and A. Pinczuk, Phys. Rev. Lett. **98**, 166802 (2007).

[23] S. S. Kubakaddi, Phys. Rev. B **79**, 075417 (2009).

Chapter 7

Concluding Remarks

7.1 Key Results

This thesis has focused upon magnetotransport measurements made on graphene Hall bar devices derived from the three most common graphene fabrication techniques: epitaxial growth on silicon carbide, exfoliation and chemical vapour deposition.

Energy loss rates on exfoliated graphene were investigated, and it was shown that the carrier energy loss rates follow a T^4 dependence. This dependence was well described by predictions of acoustic phonon deformation-potential coupling up to $\sim$100 K and with the addition of a limiting phonon relaxation time, remained consistent up to several hundred kelvin. Further, the energy loss rates in graphene were shown to be ten times larger than those in GaAs, which means that significantly greater breakdown current densities are attainable. This would allow for metrology measurements to be carried out at temperatures as high as 10 K. Breakdown current densities reported here are the highest reported values for exfoliated graphene.

Comparisons of the carrier energy loss rates were made between epitaxial, exfoliated, and CVD graphene. Two methods for measuring the energy loss rate were compared: the conventional Shubnikov-de Haas method, and an unconventional method based on the temperature dependence of the weak localization peak. The two methods were found to correlate well, with the high-field Shubnikov-de Haas measurements underestimating the energy loss rates by $\sim$40% compared to the low-field weak localization measurements. All samples were found to be well-modelled by a T^4 dependence. Further, the data were found to be well fitted by an absolute prediction of the carrier dependence of the energy loss rate of form $n^{-\frac{1}{2}}$. There is also some evidence for an enhancement of the energy loss rate in the CVD samples from "supercollisions". Finally, the Fermi velocity was measured in CVD graphene to be 1.08 x 10^6 ms^{-1}.

Weak localization was studied in epitaxial and CVD graphene. From the decomposition of the weak localization peak, scattering lengths were extracted. The saturation in the dephasing length with decreased temperature reported in the literature was investigated, and demonstrated to be an experimental artefact. Trends in the scattering lengths were also investigated: no trend in the dephasing length with carrier density was found, although, a weak decreasing trend in the elastic intervalley scattering length was observed, along with a strong decreasing trend in the total scattering length. Further, the total scattering length was demonstrated to not be primarily dominated by trigonal warping scattering for the measured carrier densities.

7.2 Future Work and Outlook

This thesis presents several opportunities for further work. The additional work, which would be of most value in building upon the findings presented in this thesis, would

be backgate studies of graphene Hall bars from multiple fabrication techniques. This would allow for adjustment of the carrier density on each individual sample, which would greatly help in disaggregating trends in carrier density from sample-specific effects. Further, the polymer gated SiC/G samples exhibited significant promise, and would highly benefit from further low-field carrier density dynamics studies, as well as from work currently in progress on the high-field breakdown in such devices.

Beyond the Oxford physics group, there is an enormous amount of activity (running into the tens of thousands of papers per year) in and around the field of graphene. The funding outlook, both in the UK and around the world, appears exceedingly rosy. A few selected examples are: a £50 million fund announced in October last year for work in the UK on commercializing graphene; a $200 million public-private partnership announced by the South Korean government in May this year to aid in commercialization; and, perhaps most excitingly of all, the European Future and Emerging Technologies fund which, if graphene is one of the technologies selected, would be worth up to €1 billion over the next ten years.

From the applications side, the first applications of graphene should be appearing imminently, and if the public's expectations can be correctly managed, we should see plenty more from this “wonder material” over the next few years.

Appendix A

Abbreviations

AC	Alternating Current
BNC	Bayonet Neill-Concelman
CNT	Carbon Nanotubes
CVD	Chemical Vapour Deposition
DC	Direct Current
DIP	Dual In-Line Package
DMM	Digital Multimeter
E-Beam	Electron Beam (Lithography)
HMDS	Hexamethyldisilazane
HOPG	Highly Oriented Pyrolytic Graphite
IPA	Isopropyl Alcohol
LL	Landau Level
MBE	Molecular Beam Epitaxy
MIBK	Methyl Isobutyl Ketone
NMP	1-Methyl-2-Pyrrolidone

PMMA	Polymethyl Methacrylate
QHE	Quantum Hall Effect
RPM	Revolutions per Minute
SiC/G	Graphene on Silicon Carbide
SdH	Shubnikov-de Haas
SEM	Scanning Electron Microscope
SMU	Source Measurement Unit
WAL	Weak Antilocalization
WL	Weak Localization